UNIVERSITY
OF TRENTO - Italy
DEPARTMENT OF INDUSTRIAL ENGINEERING

XXX cycle

Doctoral School in Materials, Mechatronics and Systems Engineering

Enhancing the Photo-electrode Features to Improve the Solar Conversion Efficiency in the Dye-Sensitized Solar Cell

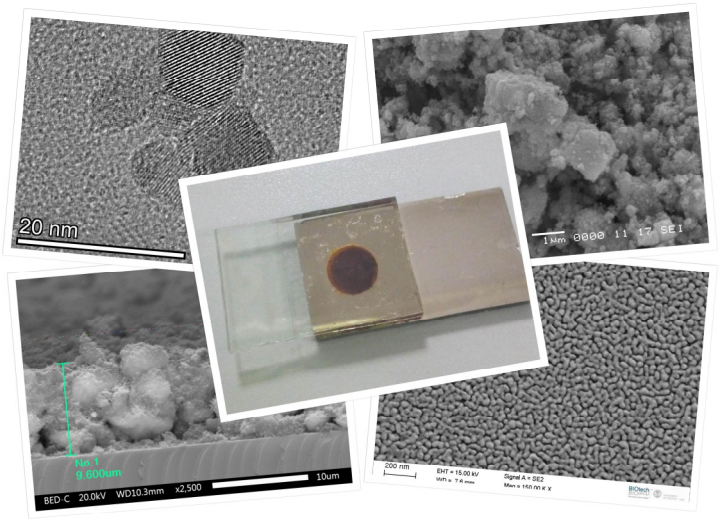

Mohammad Hossein Nateq
October 2019

ENHANCING THE PHOTO-ELECTRODE FEATURES TO IMPROVE THE SOLAR CONVERSION EFFICIENCY IN THE DYE-SENSITIZED SOLAR CELL

Mohammad Hossein Nateq

mohammadhosein.nateq@unitn.it

Approved by:

Prof. Riccardo Ceccato, Advisor
Department of Industrial Engineering
University of Trento, Italy

Ph.D. Commission:

Prof. Sandra Dirè
Department of Industrial Engineering
University of Trento, Italy,

Prof. Giuseppe Marci'
Department of Engineering
University of Palermo, Italy,

Prof. Enrico Bernardo
Department of Industrial Engineering
University of Padova, Italy.

University of Trento

Department of Industrial Engineering

October 2019

Doctoral Thesis
Enhancing the Photo-electrode Features to Improve the Solar Conversion Efficiency in the Dye-Sensitized Solar cell
Mohammad Hossein Nateq, 2019
Published in Trento (Italy) – by University of Trento
ISBN:

In the name of God

To my beloved parents,

Mehdi & Behjat,

and the immortal memory of my grandparents,

Mahmood & Ozra.

Abstract

Mesoporous semiconductors such as TiO_2 nanoparticles, as well as transparent conducting oxides (TCOs) such as indium tin oxide films are typically employed for setting up the photo-electrode module in variety of photoelectrochemical cells including Dye-Sensitized Solar Cells (DSSCs). In order to exhibit a high performance efficiency, the photo-electrodes in such applications are required to be able to harvest the light and transport the generated electrons effectively. Accordingly mesoporous layers with high values of surface area and well-established pore structure along with highly transparent and conductive TCOs are deposited on suitable substrates through the physical or chemical vapor deposition methods. The processing facilities and materials required to fabricate such high-quality devices with high values of efficiency are complicated and expensive, whereas devices of lower quality do not fulfill the demands. This issue is of particular importance regarding the energy production and developing the solar cell technologies, as it is considered by the concept of “cost per watt”. Thus, a great deal of effort is being carried out globally to enhance the efficiency of affordably-produced solar cells such as low-cost DSSCs. Utilizing the wet chemical techniques such as sol-gel method which provide a considerably more affordable route to synthesize nanoparticles and

deposit thin films without the need of applying high temperature or vacuum condition is a widely-used approach to decrease the processing expenses. However, to achieve an acceptable cost-per-watt ratio requires enhancing the obtained efficiency value as well, and therefore, modifying the processing procedures to improve the required features of the products are highly encouraged.

This thesis focuses on two individual activities: synthesis of TiO_2 nanoparticles, and also thin film deposition of a promising TCO called aluminum-doped zinc oxide (AZO); both obtained through the sol-gel route that is modified to contribute to nanostructures with suitable features for application in photoelectrochemical devices such as DSSC. In the first part, mesoporous anatase nanoparticles were synthesized through the surfactant-mediated sol–gel route. Through changing the refluxing time and water-to-surfactant molar ratio, as-prepared nanocrystals of high density and large and narrowly-distributed pore sizes were obtained, displaying surface area values up to 240 $m^2 \cdot g^{-1}$, much higher than the reported values for commercial TiO_2-based catalysts. In the second part, sol–gel dip–coating of ZnO thin films doped with 2 at.% of aluminium ions was carried out. By altering the hydrolysis reaction and changing the thermal treatment procedure, thin films of highly c-axis preferred orientation were obtained with optical transmittance of around 80% and resistivity values down to 6 – 15 $m\Omega \cdot cm$, corresponding to sheet resistance of around R_{sh} ~ 500 Ω/sq. The obtained conductivity

values, even though one order magnitude lower than those reported for the AZO thin film prepared via expensive techniques, are in the suitable range to improve the cost per watt ratio in applications such as inkjet printing of low-cost printed electronics and more affordable DSSC devices.

Table of Contents

Chapter 1
Introduction.....1

1.1. Motivation and Aim.....1
1.2. Outline 2

Chapter 2
Theoretical Background.....3

2.1. Principles and Working Mechanism of DSSC 3
2.1.1. Components and Features 4
2.1.2. Charge Transport and Recombination.....6
2.1.3. Efficiency Improvement 8
2.1.3.1. Improving the Cell Potential.....9
2.1.3.2. Improving the Cell Photocurrent.....9
2.1.3.3. Improving the Cell Fill Factor.....11
2.2. Sol-gel Synthesis of Nanoparticles and Thin Films 11
2.3. Characterization Techniques.....13
2.3.1. X-Ray Diffraction.....13
2.3.2. Nitrogen Physisorption Porosimetry 13
2.3.3. UV-Vis-NIR Spectroscopy 14
2.3.4. I-V Measurement **.....14**
2.4. References 16

Chapter 3
Practical Procedure to Set Up and Enhace the DSSC 19

3.1. Introduction.....19
3.2. Reference Samples Preparation and Characterization.....19
3.3. Enhanced Samples by Modification of TiO_2 Paste.....23
3.3.1. Experimental Procedure. 23
3.3.2. Results and Discussion. 24
3.4. References 27

Chapter 4
Synthesis of TiO_2 Nanocrystalline Particles.....28

4.1. Introduction.....28
4.2. Materials and Method.....32
4.2.1. Synthesis Procedure 32
4.2.2. Characterization.....32
4.3. Results 34
4.4. Discussion 40
4.4.1. As-Prepared Samples 40
4.4.2. Treated Samples 42
4.5. Conclusions 43
4.6. References 44

Chapter 5
Preparation and Characterization of Transparent Conducting Films 47

5.1. Introduction.....47
5.2. Materials and Methods 49
5.2.1. Sol Preparation 49
5.2.2. Gel and Powder Processing 50
5.2.3. Substrates Preparation 50

5.2.4. Film Deposition and Annealing 51
5.2.5. Characterization.....51
5.3. Results 52
5.4. Discussion.....61
5.4.1. Evolution of the Sol.....61
5.4.2. Thermal Evolution of Gels 65
5.4.3. Structural Analysis of Films 66
5.4.4. Electrical Behavior of Films 68
5.4.5. Optical Behavior of Films 71
5.4.5.1. Absorption Behaviour 71
5.4.5.2. Dispersion Behaviour 74
5.5. Conclusions 77
5.6. References 79

Chapter 6
Conclusions and Future Perspectives 87

Scientific Production.....91
Participation to Congresses, Schools and Workshops.....92
Acknowledgements 93

Chapter 1

Introduction

1.1 Motivation and Aim

The increasing global demand for energy along with the severe consequences caused by the overconsumption of fossil fuels has triggered a worldwide movement toward exploiting the renewable sources of energy. Solar energy has the potential to fulfill a significant part of the clean energy demand of the world; however, to ensure maintaining a sustainable balance between environmental protection and economic growth, the price of the generated power must be logically comparable to that generated from fossil fuels in terms of cost per watt. Thus, in order to increase the contribution of solar energy in our daily energy consumption, the technologies such as solar cells and Li ion batteries that can convert and store the solar irradiation are needed to be developed focusing on two factors; reduction in the processing cost and increasing the performance efficiency.

Dye-Sensitized Solar Cell (DSSC) is a promising technology utilizing low-cost materials and well-established processing procedures with facile manufacturing steps; and by the virtue of specific features such as light weight, low thickness and the possibility to have flexible form, it could play a significant role in supplying energy for portable electronic devices. However, it suffers from low efficiency values, particularly if high quality components and instruments are not available. Accordingly, numerous studies in this field have focused on improving the performance efficiency of the DSSCs in which, the more expensive components such as synthesized dyes and transparent conductive glasses are replaced by more affordable alternatives; and at the same time, also the processing steps through low-temperature approaches such as sol-gel method and chemical bath deposition are utilized instead of sophisticated and elaborative ones that require vacuum-based facilities.

This thesis aims to improve the performance of laboratory-grade DSSCs through enhancing the quality of its photo-electrode components, namely the

mesoporous semiconductor layer and the transparent conducting film, by modifying the sol-gel methods used to synthesize them. However, the conducted experiments and the obtained results are not limited to DSSC and can be employed for a wide range of applications including electrochemical and photoelectrochemical devices and optoelectronic tools such as Li ion batteries, water splitting and sensors. Therefore, we hope that this effort could add a small drop to the ocean of researchers' attempts towards a better future.

1.2 Outline

This thesis is outlined in six chapters. In the Chapter 2, the theoretical background of the work regarding the basic knowledge on DSSCs, sol-gel processing of nanomaterials and the main characterization techniques used in the following chapters are provided. The Chapter 3 is devoted to describe the preliminary experiments conducted to understand and clarify the general functioning principles of DSSCs through preparing a reference device and some modified samples. Then in the following two chapters, a more profoundly approach is pursued to improving the morphological and structural features of mesoporous TiO_2 nanoparticles used as the DSSC semiconductor component (Chapter 4); as well as enhancing the optoelectrical characteristics of aluminum-doped zinc oxide thin films used as the transparent conducting film of DSSC (Chapter 5). Finally, in Chapter 6 the conclusions of the work in addition to some perspectives for future activities are presented.

Chapter 2

Theoretical Background

2.1 Principles and Working Mechanism of DSSC

The basic principle of all solar cells is absorption of light and transforming photon energy into electrical energy through the charge separation mechanism. In conventional p-n junction-based solar cells, both tasks are carried out by an inorganic semiconductor; either in the form of a thick layer of single or polycrystalline silicon referred as the first generation of solar cells, or the thin films of amorphous silicon (aSi), cadmium telluride (CdTe) and copper indium gallium selenide (CIGS) which comprise the second generation of solar cells.

The working mechanism of DSSC as a third generation of solar cells is quite different since the light absorption and charge separation occur separately in different device components [1]. The light-harvesting part is a photosensitive dye molecule that is anchored to the surface of a wide band-gap semiconductor and surrounded by a redox electrolyte as the hole-transporting component. Upon the illumination, incident photons with appropriate energy level stimulate the dye molecules, whereby electrons from the highest occupied molecular orbital (HOMO) are excited to the lowest unoccupied molecular orbital (LUMO), forming the electron/hole pairs. Afterwards, the charge separation occurs at different interfaces of the dye molecule; the exited electrons are injected into the conduction band of the semiconductor component and then transported throughout its microstructure to the transparent conducting film of the photo-electrode, while the resulted holes are recovered by the oxidizing species of the hole-transporting electrolyte. Finally the cycle completes through the reduction of oxidizing species by a catalyst layer on the counter-electrode. This explanation clarifies the general concept of DSSC as a "photoelectrochemical" device, a photon-driven electrochemical cell. Figure 2.1 shows the schematic illustration of the photoelectrochemical process in the DSSC.

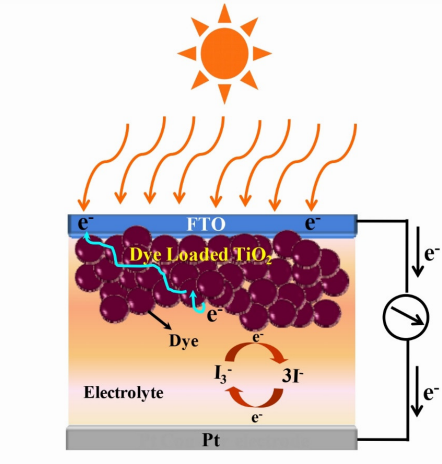

Figure 2.1. *The schematic illustration of the photoelectrochemical process in a DSSC.*

2.1.1 Components and Features

According to Figure 2.1, a DSSC device can be considered as made of five main components:

1 - A wide band gap semiconductor layer that is deposited on the photo-electrode to act as a support for the dye molecules and also to transport the excited electrons. As a requirement, a large surface area is essential to ensure a great amount of dye loading. Besides, a fast charge transport rate is necessary to ensure acceptable electron collection efficiency. These two features are the determining characteristics for an ideal semiconductor layer of DSSC [2]. Considering other parameters including chemical neutrality and low production cost, the choice for this component is limited to nanostructures of TiO_2, ZnO and SnO_2; among which TiO_2-based DSSCs show higher efficiency values [3]. Moreover, anatase polymorphs of TiO_2 is preferred because the electron transport rate in rutile, due to its higher packing density, is slower than in anatase and its smaller surface area per unit volume results in less dye loading capacity [4].

2 - A photosensitive dye that is chemically adsorbed on the semiconductor layer and generates the charge under illumination is the key component of a DSSC. For an efficient performance, the dye must have high molar extinction coefficients in the visible and near-infrared region in order to be sensitized by the widest part of the

sunlight spectra. Moreover, an appropriate LUMO and HOMO energy couples is essential to ensure effective charge injection into the semiconductor and dye regeneration by the electrolyte; this means the presence of a more negative LUMO than the conduction band of the semiconductor and a more positive HOMO than the redox potential of the electrolyte.
Among natural and synthetic dyes, ruthenium polypyridyl dyes such as N719® and N3® molecules have been the most commonly used dyes in TiO_2-based DSSCs since the combination of their broad light absorption range and suitable energy levels matched with TiO_2 have always resulted to score the highest efficiency of 12.3% [5]. However, using metal-free organic sensitizers are under extensive investigation despite the lower obtained efficiency since they are available more affordably [6].
It is worth mentioning that in addition to photosensitive dyes, there are two different classes of sensitizers to couple with semiconductor and hole-transporter components, quantum-dots and organometallic halide perovskites that form additional categories along with DSSCs, namely quantum-dot solar cells and perovskite solar cells. However, similar principles govern their functioning mechanism.

3 - A redox electrolyte for transferring electrons from the counter-electrode to the dye to regenerate the excited molecules. In other words, the electrolyte acts as a charge transport medium to transfer positive charges toward the counter-electrode. A high electrical conductivity for fast electron transfer and also suitable redox potential regarding the LUMO energy level of the dye are the main important features of an optimal electrolyte. Moreover the capability of establishing a maximum surface coverage over the dye molecules is essential which explains how better infiltration of liquid electrolytes inside the semiconductor layer results in highest efficiency values for DSSCs [7]. Among the different types of redox couples, the most commonly used ones are $I^{3-}/3I^{-}$ [8] and Co^{2+}/ Co^{3+} [5] due to their good conductivities and suitable redox potential regarding ruthenium dyes, together with a rapid dye regeneration rate [9]. Durability limitations and problems regarding the solar cell sealing to prevent the evaporation of liquid electrolytes have encouraged using solid-state electrolytes such as organic compounds of OMeTAD and Spiro-OMeTAD [10]. However, they offer much lower conversion efficiency values because of the difficulties in the infiltration of a solid phase into semiconductor layer and a subsequently poor surface contact with the sensitizer component.

4 - A catalyst layer that is deposited on the counter-electrode to catalyze the reduction of the oxidizing species of the electrolyte and therefore, it provides the required electron for the electrolyte for the following regeneration of dye molecules. High conductivity and suitable electrocatalytic energy level regarding the electrolyte redox potential is necessary to accelerate the reduction reaction. Noble metals such

as Pt, Au and Ag along with carbon-based structures such as porous carbon, carbon nanotubes and graphene are used as catalyst layers in DSSCs [[11],[12]]; however, deposition of Pt through thermal decomposition of hexachloroplatinic salt in isopropanol [13], or sputtering [14] provides higher values of efficiency compared with other compounds.

5 - A transparent conducting film (TCF) as a thin layer covering the photo-electrode surface beneath the semiconductor layer. Since the photo-electrode is simultaneously responsible for providing the illumination path for the dye molecules and collecting the generated charge from the semiconductor layer, having a high electrical conductivity with high optical transparency is an essential requirement that cannot be fulfilled with common photo-electrodes made of glass or transparent polymers. Among the limited number of materials possessing such a property, the most widely utilized are thin films of certain wide band-gap n-type semiconducting oxides like In_2O_3, SnO_2 and ZnO, known as transparent conducting oxides (TCOs), degenerately doped with traces of impurities. They offer high transmission in the visible and even near infrared wavelength range and also are of high enough conductivity to collect electrons efficiently. Commercially, indium-doped tin oxide (ITO) is probably the most common TCO used in LCD televisions, plasma displays and touch screen electronics; but the high cost of indium contributes to the high price of these types of electronics [15]. In DSSCs, the normally used TCO is fluorine-doped tin oxide (FTO), which is able to undergo the annealing temperature necessary for DSSC processing and can withstand the acidic conditions in case of using acetic acid for TiO_2 paste processing. However, FTO is not the most affordable type of TCO and ZnO-based TCOs, especially aluminum-doped zinc oxide (AZO), offer nearly identical features with lower cost with the expense of some disadvantages such as instability in acidic conditions.

2.1.2 Charge Transport and Recombination

The performance and efficiency of DSSCs are governed by the energy-level arrangements between the all components, as well as the kinetics of the charge separation and transfer processes. Figure 2.2(a) shows the diagram for the energy levels with respect to a normal hydrogen electrode (NHE) for a DSSC comprising TiO_2 as the semiconductor, N719 as the sensitizer dye molecule, the liquid electrolyte of $I^{3-}/3I^-$, catalytic layer of platinum and FTO as the TCF. In Figure 2.2(b) a schematic representation of the processes contributing to conversion of the photons energy to electrical current are labelled as 1 to 6 along with an approximation for the kinetics of each process.

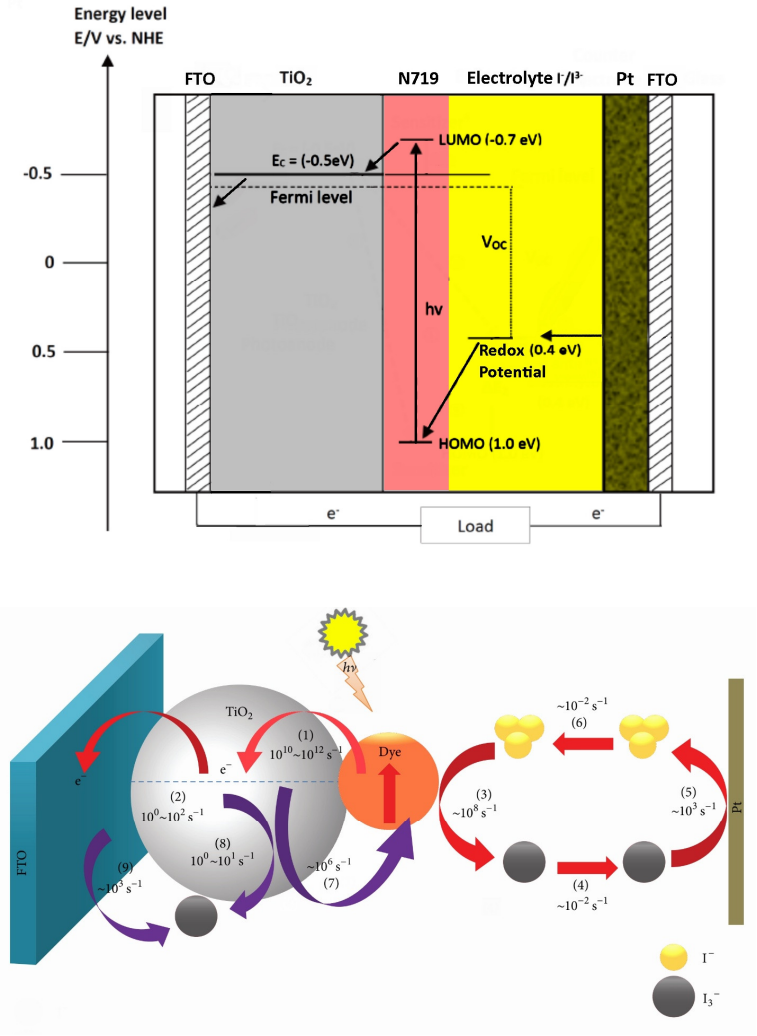

Figure 2.2. *(a) The energy level diagram with respect to a normal hydrogen electrode (NHE) for conventional a DSSC. (b) The schematic illustration of the charge transport (labelled 1 to 6) and recombination processes (labelled 7 to 9) [16].*

According to the previous explanations and referring to the labels in Figure 2.2(b), upon the illumination and photoexcitation of the dye, the following processes occur in DSSC:

1. Electron injection to the conduction band of TiO_2.

2. Electron transport to the FTO film throughout the TiO_2 structure.

3. Regeneration of the oxidized dye by I^- species of electrolyte and formation of I_3^-
4. Diffusion of I_3^- to the counter-electrode.

5. Reduction of I_3^- by the platinum layer and formation I^-, according to:
$I_3^- + 2e^- \rightarrow 3I^-$

6. Diffusion of I^- to the repeat regeneration of the oxidized dye molecule.

However, there are also some undesired reactions in the reverse direction called charge recombination processes, labelled as 7 to 9 in Figure 2.2(b):

7. Regeneration of the oxidized dye by the electrons in TiO_2 conduction band.

8. Reduction of I_3^- by the electrons in TiO_2 conduction band.

9. Reduction of I_3^- by the electrons collected by the FTO film.

For the efficient functioning of the DSSC, the rate of charge transport at all interfaces must be faster than the charge recombination. For the DSSCs using TiO_2 nanocrystalline semiconductor sensitized by Ru-based dyes and $I_3^-/3I^-$ electrolyte, the charge injection to TiO_2 conduction band (reaction 1) is extremely fast, in the range of femtoseconds, while the excited-state decay of the dye is slower for several orders of magnitude and occurs over microseconds. Thus the charge loss due to excited-state decay of the dye is not probable. Afterwards, however, the slow charge transport throughout the TiO_2 layer (reaction 2) and slow reduction of I_3^- species by platinum (reaction 5) provide the recombination opportunity through the reactions 7 and 8 at TiO_2/N719 and TiO_2/I_3^- interfaces respectively [17]. Moreover, in case of direct contact between the electrolyte and FTO film, a considerable charge recombination is resulted because the reduction of I_3^- occurs much faster at FTO/I_3^- interface (reaction 9) compared with Pt/I_3^- (reaction 5).

2.1.3 Efficiency Improvement

Despite the numerous investigations dedicated to improve the efficiency of DSSC, the highest obtained value of 12.3% is still behind the previous solar cell generations and is even less than theoretically attainable values [18]., As it is explained in the Section 2.3.4 for I – V measurements, the conversion efficiency of any solar cell

including DSSC could be simply defined the ratio of the maximum obtained power P_{max} to the input power $P_{in.}$, which gives rise to the Equation 2-2 .Accordingly, the only way to improve the efficiency value is to increase the parameters of I_{SC}, V_{OC}, and the FF. Below we discuss about the possibility, perspectives and limitations regarding each parameter.

2.1.3.1 Improving the Cell Potential

The open-circuit voltage V_{OC} is the maximum electrical potential of the circuit when the resistivity is infinite. In DSSC, as observed in the energy level diagram in Figure 2.2(a), V_{OC} can be considered of as the largest difference in potential that can develop between the external contacts at the cathode and anode of the cell, which is roughly the difference between the Nernstian potential of the electrolyte, known as redox potential and the Fermi level of the semiconductor [19] according to the equation below:

$$V_{OC} = \frac{E_{CB}}{q} + \frac{kT}{q} \cdot \ln\left(\frac{n}{N_{CB}}\right) - \frac{E_{redox}}{q} \qquad (2-1)$$

in which, n is the number of electrons in the TiO_2 conduction band and E_{CB} and N_{CB} are TiO_2 conduction band energy level and its effective density of states.

Thus, it is possible to estimate the V_{OC} of the DSSC if the semiconductor material and the electrolyte type are determined. For instance, in a conventional DSSC with TiO_2 semiconductor and iodine-based electrolyte, the highest possible value for V_{OC} is around 600 – 700 mV [20]. Since the Fermi levels of the conventionally-used semiconductors in DSSC devices are close the one of TiO_2, the most efficient way to improve V_{OC} is choosing another type of electrolyte with more positive redox potential [21]. However, this work is dedicated to DSSCs assembled with the iodine-based electrolyte and using another type of electrolyte is out of the scope.

2.1.3.2 Improving the Cell Photocurrent

The short-circuit current I_{SC} is the maximum generated current when the resistivity of the circuit is almost zero. Generally, in order to eliminate the effect of the cell area, the short-circuit current density J_{SC} is reported instead of I_{SC} as $J_{SC} = I_{SC}$/Cell Area.

This parameter largely depends on the amount of the charge that DSSC injects to the circuit and is directly related to the generated charge and the lost charge due to the interfacial recombination.

The most straightforward way to improve the amount of Jsc is to absorb the energy of photons regarding a larger part of the sunlight spectra. The optical gap of the Ru-based dyes is around 1.8 eV, allowing it to absorb the energy of almost all of the photons in the visible range [22]. Increasing the photocurrent density requires decreasing the optical gap to extend the dye's absorption into the near-infrared region with higher extinction coefficients and a more panchromatic absorption.

However, since this work is dedicated to DSSCs sensitized with N719 as a Ru-based dye, using another type of dye is out of the scope.

Apart from using more efficient dyes, it is possible to increase the amount of generated charge through employing higher volumes of a specific dye per unit of area. This strategy directly associates with the semiconductor features as the dye-loading component in DSSC.

In the primary investigations on photoelectrochemical cells, the semiconductor component was a flat film of single or polycrystalline TiO_2 that could bring just very low values of conversion efficiency [23]. A tremendous change happened when Grätzel et al. used a mesoporous semiconductor layer formed by sintering 20 nm-sized TiO_2 particles instead of a planar semiconductor, whereby the overall conversion efficiency increased by an order of magnitude [24]. Combining a large internal surface area with the improved porosity features are considered to be responsible for the successful approach. Since photons are only absorbed at the TiO_2 surface, the semiconductor should exhibit an extremely large surface area to increase the available area for dye loading. Upon excitation and electron injection, a rapid reduction of oxidized dye by the surrounding electrolyte is necessary; otherwise, the regeneration of the oxidized dye by the electrons in TiO_2 conduction band is inevitable. Here, the pores in TiO_2 microstructure play an important role by providing enough space to allow infiltration of the electrolyte.

However, the porous network of TiO_2 has to offer also intact percolation paths for rapid transportation of charges. The electron transport performance is determined by the kinetic competition between the electron diffusion rate and electron lifetime. The diffusion rate is dependent on diffusion coefficient D_n. The diffusion coefficient itself is a function of electron mobility μ and the density of sub bandgap trap states [[25],[26]. The fundamental disadvantage of the nanoparticle-based semiconductor design is the considerably small diffusion coefficient, D_n, resulting in poor charge transport [27]. While the single-crystal of anatase shows electron mobility of around $\mu \approx 10\ cm^2.V^{-1}.s^{-1}$ [28], generally a several orders of magnitude reduction of value is observed in nanoparticle to around $\mu \approx 10^{-1} - 10^{-5}\ cm^2.V^{-1}.s^{-1}$ [29],[30]. To enhance charge-carrier transport, 1D structures such as TiO_2 nanorods or nanotubes have been extensively studied to replace electrode architectures in DSSCs. These structures show greatly enhanced charge carrier transport as they offer 1D and therefore almost direct percolation path in contrast with randomly-oriented ones in nanoparticle-based structures. However, they suffer from reduced surface area per unit volume due to the lack of nanoporosity associated with the surface roughness of nanometer-sized crystals [20]. Thus, despite many promising studies in increasing charge-transport properties, maximum efficiency still belongs to the devices with nanoparticle-based semiconductor and therefore, combining their high values of surface area with improved charge-carrier transport is considered to be the main solution to increase the DSSC efficiency.

Accordingly, another approach is overcoming the electronic disorder in the nanocrystalline structure of TiO_2 that does not necessarily correlate with the particles mesoscale arrangement and mainly originates from the polycrystalline nature of the semiconductor layer. In comparison with a single-crystal where only lattice defects limit the mean free path of propagating electrons [31], in polycrystalline structures, charge traps located at the grain-boundaries also reduce the electron mobility and thus, the diffusion coefficient. These charge traps comprise a tail of sub-bandgap states below the conduction band [32],[33]. It is widely accepted that the electron transport in such microstructures is accompanied by repetitive cycles of trapping and detrapping, whereby the generated electrons mostly populate localized states below the conduction band instead of diffusing towards the TCO [34]. Regarding the grain-boundaries role in suppressing the electron mobility, the higher values of crystallite size of the mesoporous TiO_2 are shown to have a profound effect on improving the charge transport properties through influencing on the charge transport lifetime [35],[36],[37]. The importance of this finding lies in the fact that for transport-limited recombinations, any other improvement in charge diffusion would result in a corresponding increase in recombination [38]. Therefore, the ideal semiconductor layer is of large crystallite size and high volume of pores with a considerable surface area value. This concept is followed by trying to synthesize TiO_2 nanoparticles with enhanced crystallinity and improved surface area through surfactant-assisted sol-gel route, as discussed in Chapter 3.

2.1.3.3 Improving the Cell Fill Factor

This parameter is defined by the ratio of obtained maximum power P_{max} to the product of I_{SC} and V_{OC}. Ideally this values is close to unity, but it is attenuated by the total series resistance of the cell, which includes the sheet resistances of the substrate and counter electrode [19] and utilizing a TCO film of higher conductivity could improve this parameter. However, high quality TCOs comprise a considerable cost of DSSC and therefore, more affordable TCOs such as AZO prepared through non-expensive approached like sol-gel method or spray pyrolysis are economically preferred. This topic will be discussed more profoundly in Chapter 4 through the attempt for sol-gel synthesis of AZO thin film with high values of optical transmission and electrical conductivity.

2.2 Sol-gel Synthesis of Nanoparticles and Thin Films

. The sol-gel process involves the evolution of inorganic networks through the formation of a colloidal suspension (sol) towards the gelation of the sol in order to produce a network in a continuous liquid phase (gel). The precursors for the synthesis of these colloids are made of a metal or semimetallic element surrounded by various reactive ligands. Metal alkoxides are most popular because they react

quite immediately with water. The most widely used metal alkoxides are the silicon-derived precursors, named alkoxysilanes; as an example, tetramethoxysilane (TMOS) and tetraethoxysilane (TEOS). In a general way, other alkoxides, as aluminium, titanium and boron are also common and widely employed in the sol-gel process.

The sol-gel process can be described as the results of three reactions: hydrolysis of the alkoxide, condensation between two M-OH groups (water condensation), and M-OH and M-OR condensation (alcohol condensation). This general reaction scheme can be seen in Figure 2.3.

Hydrolysis occurs by the nucleophilic attack of the oxygen contained in water on the metallic or semimetallic atom. Subsequent condensation reactions take place producing oxygen bonds between two metallic atoms, under the form of monomers. The polymerization steps could be described as, a) polymerization of monomers to polymers, b) condensation to primary particles, c) growth or agglomeration of primary particles and d) linking of particles into mono-, di- or three-dimensional network. Networks extend throughout the liquid medium, giving rise to a gel. In the last stage water and alcohol are released from the network leading to a gradual shrinkage and even cracking of the monolithic gel.

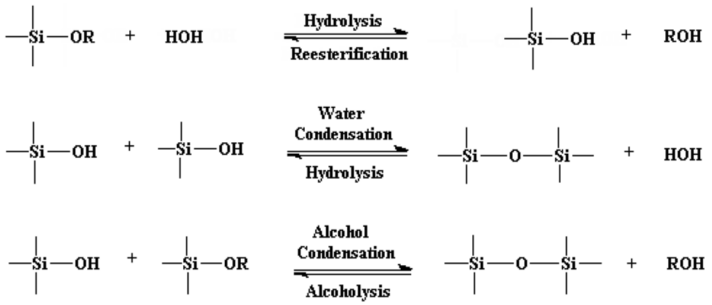

***Figure 2.3**. Chemical reactions involved in the sol-gel process.*

Indeed, the features of a particular sol-gel derived inorganic network are related to various parameters that affect the rate of hydrolysis and condensation reactions: pH, temperature and time of reaction, reagent concentrations, catalyst nature and concentration, H_2O/alkoxide molar ratio, aging temperature and final drying. Thus, by controlling these factors, it is possible to change the structure and properties of the resulting inorganic networks.

2.3 Characterization Techniques

2.3.1 X-Ray Diffraction

X-ray diffraction spectroscopy is a rapid analytical technique primarily used for phase identification of crystalline and nanocrystalline materials, whether in bulk form or thin films, and can provide information on the lattice parameters, crystallite size, preferred orientation of polycrystals as well as defects and lattice strain.
This technique works based on the interaction of incident monochromatic X-rays with the sample. When the wavelength of the incident radiation is of the same order of magnitude of the dimensions of the illuminated objects, these become secondary sources of radiation giving rise to interference effect. In the case of X-ray radiation, typical wavelengths fall into the range 10^{-8} – 10^{-12} m. correspondent to the atomic disposition inside the characteristic unit cells of the investigated crystalline solids. In this case, the interaction between incident beams and the surface of the solid waves constructive interference, giving rise to diffracted beams, when conditions satisfy Bragg's Law ($n\lambda = 2d.\sin\theta$), that is valid for monochromatic radiations. This law relates the wavelength of the electromagnetic radiation to the diffraction angle and the lattice spacing in the sample. The diffracted X-rays are then detected, processed and counted. Using a powder diffractometer, by rotating the sample through a θ angle range, all possible diffraction directions of the lattice are attained when the detector is simultaneously rotated by the double of the incident angle. Conversion of the diffraction peaks to d-spacing allows identification of the mineral since each mineral has a unique set of d-spacing. Moreover, the same instrument can also be used for the analysis of thin films, by changing the instrumental geometry; in fact, asymmetric scan configuration can be adopted: in this case, scan is performed only on the detector angle, once fixed an incident angle value, usually less than 1°. With this configuration, most of the incident beam travels inside the film and the expenses of the substrate, enhancing its contribution. Moreover, the resulting diffracted beam is always aligned with the detector, as in asymmetric scan condition the following relationship is verified: $2\theta = \theta + \theta'$, where θ is the incident beam and θ' is the diffracted one.

2.3.2 Nitrogen Physisorption Porosimetry

When a gas molecule gets close to a solid surface, two different interactions can take place: physisorption, when weak interactions, like van der Waals bonds, arise between gas and solid, and chemisorption when strong interactions, as chemical bonds, are formed. In the first case, a low energy exothermic effect can be observed, about 80 $kJ \cdot mol^{-1}$, and its detection is more sensitive when the analysis temperature

decreases. So, in this analytical technique it is possible to determine the molar quantity of gas taken up at a constant temperature value (isothermal conditions) by a clean solid surface as a function of the equilibrium pressure of the gas. Actually, in order to get morphological information on the solid surface, the measured values have to be expressed in terms of relative pressure P/P_0, where P is the measured pressure of the gas and P_0 is the saturation pressure of the same gas in the environment. The resulting isothermal curves, thus, are typical of the analysed gas and not dependent from the used gas.
Different isothermal curves can be obtained from different solid surfaces; their classification, as defined by IUPAC, allows the assessment of specific surface area values, by using BET equation that is valid under the conditions of gas monolayer coverage of the surfaces. Moreover, determination of pores and pore size distribution curves can be outlined from the whole isothermal branches.

2.3.3 UV-Vis-NIR Spectroscopy

When an electromagnetic wave illuminates an object, together with the physical interactions, such as diffraction previously described, some chemical interactions could occur, when a change in the energy status of the matter takes place. In particular, absorption or emission of energy can involve the matter, under the form of atoms or molecules, giving rise to different spectroscopic analytical methods. Particularly, exchanged energy could alter, in its turn, the energetic state of the matter that can be considered as the sum of different contributions: for molecules, we can measure the change in nuclear, electronic, vibrational and rotational energies. Thus, employing different radiation sources, for instance ultraviolet or infrared lamps, we are able to evaluate the energy responsible of the bonds present inside the molecules, obtaining details regarding their structures. At the same time, we can evaluate the “transparency” of the matter if no interactions with the incident light occurs

2.3.4 I - V Measurement

The current – voltage measurement is the most frequently used method for performance characterization of solar cells under standardized sunlight conditions. This technique is easily performed on an illuminated cell in a circuit equipped by a varistor, voltmeter and a sensitive amperemeter. Using a linear sweep with a stepwise change of the circuit resistance from zero load (short-circuit) to the infinite load (open-circuit), the measured pairs of I – V values are recorded to draw the voltage versus current curve. A typical of I – V curve is illustrated in Figure 2.4.

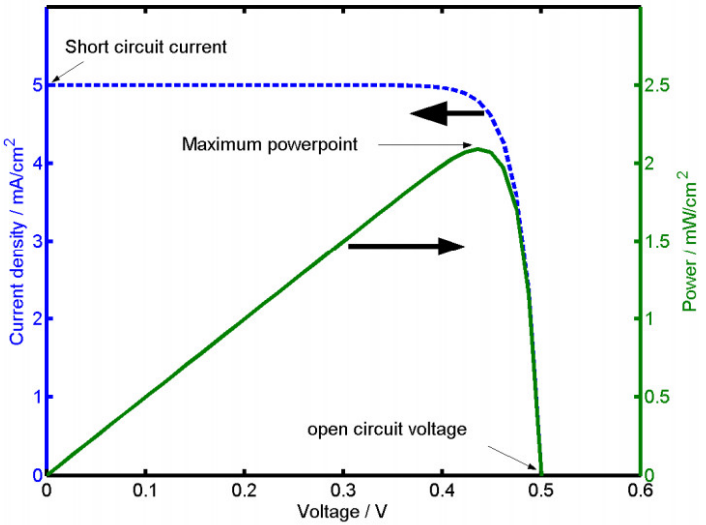

Figure2.4. *An example for I – V measurement result. The short-circuit current I_{SC} and the open-circuit voltage V_{OC}, along with P_{max} are pointed out.*

As it is observed in Figure 2.4 , the solar cell generates the maximum current at the short-circuit condition when the voltage equals to zero. On the other hand, the maximum voltage of the circuit is at open-circuit condition when there is no electrical current inside it. These two parameters, namely the short-circuit current I_{SC} and open-circuit voltage V_{OC}, are characteristic features of the cell due to their role in defining the conversion efficiency.

The conversion efficiency of any solar cell could be simply defined by the ratio of the maximum obtained power P_{max} to the input power P_{in}. The latter, P_{in}, is related to the incident light flux, for which, 100 mW·cm^{-2} in air mass (AM) 1.5 condition is used as the standard illumination in solar simulator devices. The spectrum AM1.5 consists of the UV, visible, and IR part of the solar spectrum passed throughout the air distance of 1.5 times the atmosphere thickness according to the international standard IEC 60904-3 [39]. The former parameter P_{max} is obtained through the measurement results where the product of the I – V pair is maximum. The I – V pair giving the P_{max}, namely I_m and V_m, always exists between the open-circuit and short-circuit conditions. However, it is preferred to define the efficiency according to I_{SC} and V_{OC} values. This is carried out by defining another parameter called Fill Factor, FF, considered as the ratio of I_m and V_m product to the product of I_{SC} and V_{OC}, or: $FF = \frac{I_m \cdot V_m}{I_{SC} \cdot V_{OC}}$. Therefore the conversion efficiency is as follows:

$$\eta = \frac{P_{max}}{P_{in}} = \frac{V_{OC} \cdot I_{SC} \cdot FF}{P_{in}} \quad (2-2)$$

It is important to note that I – V curve of DSSCs is more sensitive to the rate of changing the load compared with conventional solar cells and therefore, an I – V measurement takes a longer time for DSSCs. This is because DSSC is a photo-chemical solar cell, which needs a longer response time to achieve the same photoelectric conversion [40].

2.4 References

1. Grätzel, M. Photoelectrochemical cells. *Nature* **2001**, *414*, 338–344.
2. Maçaira, J.; Andrade, L.; Mendes, A. Review on nanostructured photoelectrodes for next generation dye-sensitized solar cells. *Renew. Sustain. Energy Rev.* **2013**, *27*, 334–349.
3. Bauer, C.; Boschloo, G.; Mukhtar, E.; Hagfeldt, A. Ultrafast studies of electron injection in Ru dye sensitized SnO2 nanocrystalline thin film. *Int. J. Photoenergy* **2002**, *4*, 17–20.
4. Park, N.-G.; van de Lagemaat, J.; Frank, A.J. Comparison of Dye-Sensitized Rutile- and Anatase-Based TiO 2 Solar Cells. *J. Phys. Chem. B* **2000**, *104*, 8989–8994.
5. Yella, A.; Lee, H.-W.; Tsao, H.N.; Yi, C.; Chandiran, A.K.; Nazeeruddin, M.K.; Diau, E.W.-G.; Yeh, C.-Y.; Zakeeruddin, S.M.; Gratzel, M. Porphyrin-Sensitized Solar Cells with Cobalt (II/III)-Based Redox Electrolyte Exceed 12 Percent Efficiency. *Science (80-.).* **2011**, *334*, 629–634.
6. Yen, Y.-S.; Chou, H.-H.; Chen, Y.-C.; Hsu, C.-Y.; Lin, J.T. Recent developments in molecule-based organic materials for dye-sensitized solar cells. *J. Mater. Chem.* **2012**, *22*, 8734.
7. Fukui, A.; Komiya, R.; Yamanaka, R.; Islam, A.; Han, L. Effect of a redox electrolyte in mixed solvents on the photovoltaic performance of a dye-sensitized solar cell. *Sol. Energy Mater. Sol. Cells* **2006**, *90*, 649–658.
8. Wu, J.; Lan, Z.; Hao, S.; Li, P.; Lin, J.; Huang, M.; Fang, L.; Huang, Y. Progress on the electrolytes for dye-sensitized solar cells. *Pure Appl. Chem.* **2008**, *80*, 2241–2258.
9. Boschloo, G.; Hagfeldt, A. Characteristics of the Iodide/Triiodide Redox Mediator in Dye-Sensitized Solar Cells. *Acc. Chem. Res.* **2009**, *42*, 1819–1826.
10. Bach, U.; Lupo, D.; Comte, P.; Moser, J.E.; Weissörtel, F.; Salbeck, J.; Spreitzer, H.; Grätzel, M. Solid-state dye-sensitized mesoporous TiO_2 solar cells with high photon-to-electron conversion efficiencies. *Nature* **1998**, *395*, 583–585.
11. Wu, M.; Ma, T. Platinum-Free Catalysts as Counter Electrodes in Dye-Sensitized Solar Cells. *ChemSusChem* **2012**, *5*, 1343–1357.

12. Wang, H.; Sun, K.; Tao, F.; Stacchiola, D.J.; Hu, Y.H. 3D Honeycomb-Like Structured Graphene and Its High Efficiency as a Counter-Electrode Catalyst for Dye-Sensitized Solar Cells. *Angew. Chemie Int. Ed.* **2013**, *52*, 9210–9214.
13. Papageorgiou, N. An Iodine/Triiodide Reduction Electrocatalyst for Aqueous and Organic Media. *J. Electrochem. Soc.* **1997**, *144*, 876.
14. Tsekouras, G.; Mozer, A.J.; Wallace, G.G. Enhanced Performance of Dye Sensitized Solar Cells Utilizing Platinum Electrodeposit Counter Electrodes. *J. Electrochem. Soc.* **2008**, *155*, K124.
15. Nateq, M.H.; Ceccato, R. Enhanced Sol–Gel Route to Obtain a Highly Transparent and Conductive Aluminum-Doped Zinc Oxide Thin Film. *Materials (Basel).* **2019**, *12*, 1744.
16. Sarker, S.; Ahammad, A.J.S.; Seo, H.W.; Kim, D.M. Electrochemical Impedance Spectra of Dye-Sensitized Solar Cells: Fundamentals and Spreadsheet Calculation. *Int. J. Photoenergy* **2014**, *2014*, 1–17.
17. Sharifi, N.; Tajabadi, F.; Taghavinia, N. Recent Developments in Dye-Sensitized Solar Cells. *ChemPhysChem* **2014**, *15*, 3902–3927.
18. Snaith, H.J. Estimating the Maximum Attainable Efficiency in Dye-Sensitized Solar Cells. *Adv. Funct. Mater.* **2010**, *20*, 13–19.
19. Peter, L.M. Dye-sensitized nanocrystalline solar cells. *Phys. Chem. Chem. Phys.* **2007**, *9*, 2630.
20. Docampo, P.; Guldin, S.; Leijtens, T.; Noel, N.K.; Steiner, U.; Snaith, H.J. Lessons Learned: From Dye-Sensitized Solar Cells to All-Solid-State Hybrid Devices. *Adv. Mater.* **2014**, *26*, 4013–4030.
21. Martinson, A.B.F.; Hamann, T.W.; Pellin, M.J.; Hupp, J.T. New Architectures for Dye-Sensitized Solar Cells. *Chem. - A Eur. J.* **2008**, *14*, 4458–4467.
22. Qin, Y.; Peng, Q. Ruthenium Sensitizers and Their Applications in Dye-Sensitized Solar Cells. *Int. J. Photoenergy* **2012**, *2012*, 1–21.
23. Deb, S.K. Thin-film solar cells: An overview. *Renew. Energy* **1996**, *8*, 375–379.
24. Nazeeruddin, M.K.; Kay, A.; Rodicio, I.; Humphry-Baker, R.; Mueller, E.; Liska, P.; Vlachopoulos, N.; Graetzel, M. Conversion of light to electricity by cis-X2bis(2,2'-bipyridyl-4,4'-dicarboxylate)ruthenium(II) charge-transfer sensitizers (X = Cl-, Br-, I-, CN-, and SCN-) on nanocrystalline titanium dioxide electrodes. *J. Am. Chem. Soc.* **1993**, *115*, 6382–6390.
25. Bisquert, J. Hopping Transport of Electrons in Dye-Sensitized Solar Cells. *J. Phys. Chem. C* **2007**, *111*, 17163–17168.
26. Anta, J.A.; Mora-Seró, I.; Dittrich, T.; Bisquert, J. Dynamics of Charge Separation and Trap-Limited Electron Transport in TiO 2 Nanostructures. *J. Phys. Chem. C* **2007**, *111*, 13997–14000.
27. Dittrich, T.; Lebedev, E.A.; Weidmann, J. Electron drift mobility in porous TiO_2 (anatase). *Phys. Status Solidi Appl. Res.* **1998**, *165*.
28. Solovan, M.N.; Maryanchuk, P.D.; Brus, V. V.; Parfenyuk, O.A. Electrical and optical properties of TiO_2 and TiO_2:Fe thin films. *Inorg. Mater.* **2012**, *48*, 1026–1032.
29. Tiwana, P.; Docampo, P.; Johnston, M.B.; Snaith, H.J.; Herz, L.M. Electron Mobility and Injection Dynamics in Mesoporous ZnO, SnO 2 , and TiO_2 Films Used in Dye-Sensitized Solar Cells. *ACS Nano* **2011**, *5*, 5158–5166.
30. Leijtens, T.; Lim, J.; Teuscher, J.; Park, T.; Snaith, H.J. Charge Density Dependent Mobility of Organic Hole-Transporters and Mesoporous TiO 2

Determined by Transient Mobility Spectroscopy: Implications to Dye-Sensitized and Organic Solar Cells. *Adv. Mater.* **2013**, *25*, 3227–3233.
31. Forro, L.; Chauvet, O.; Emin, D.; Zuppiroli, L.; Berger, H.; Lévy, F. High mobility n -type charge carriers in large single crystals of anatase (TiO 2). *J. Appl. Phys.* **1994**, *75*, 633–635.
32. J. Frank, A.; Kopidakis, N.; Lagemaat, J. Van De Electrons in nanostructured TiO_2 solar cells: transport, recombination and photovoltaic properties. *Coord. Chem. Rev.* **2004**, *248*, 1165–1179.
33. Jean, J.; Mahony, T.S.; Bozyigit, D.; Sponseller, M.; Holovský, J.; Bawendi, M.G.; Bulović, V. Radiative Efficiency Limit with Band Tailing Exceeds 30% for Quantum Dot Solar Cells. *ACS Energy Lett.* **2017**, *2*, 2616–2624.
34. O'Regan, B.C.; Durrant, J.R. Kinetic and Energetic Paradigms for Dye-Sensitized Solar Cells: Moving from the Ideal to the Real. *Acc. Chem. Res.* **2009**, *42*, 1799–1808.
35. Docampo, P.; Ivaturi, A.; Gunning, R.; Diefenbach, S.; Kirkpatrick, J.; Palumbiny, C.M.; Sivaram, V.; Geaney, H.; Schmidt-Mende, L.; Welland, M.E.; et al. The influence of 1D, meso- and crystal structures on charge transport and recombination in solid-state dye-sensitized solar cells. *J. Mater. Chem. A* **2013**, *1*, 12088.
36. Docampo, P.; Guldin, S.; Steiner, U.; Snaith, H.J. Charge Transport Limitations in Self-Assembled TiO 2 Photoanodes for Dye-Sensitized Solar Cells. *J. Phys. Chem. Lett.* **2013**, *4*, 698–703.
37. Guldin, S.; Hüttner, S.; Tiwana, P.; Orilall, M.C.; Ülgüt, B.; Stefik, M.; Docampo, P.; Kolle, M.; Divitini, G.; Ducati, C.; et al. Improved conductivity in dye-sensitised solar cells through block-copolymer confined TiO 2 crystallisation. *Energy Environ. Sci.* **2011**, *4*, 225–233.
38. Kopidakis, N.; Benkstein, K.D.; van de Lagemaat, J.; Frank, A.J. Transport-Limited Recombination of Photocarriers in Dye-Sensitized Nanocrystalline TiO 2 Solar Cells. *J. Phys. Chem. B* **2003**, *107*, 11307–11315.
39. Hsu, S.T.; Long, Y.S.; Wu, T.C. Standardization of Current-Voltage Test Method for DSSC Products. *Appl. Mech. Mater.* **2017**, *870*, 263–268.
40. Zheng, D.; Ye, M.; Wen, X.; Zhang, N.; Lin, C. Electrochemical methods for the characterization and interfacial study of dye-sensitized solar cell. *Sci. Bull.* **2015**, *60*, 850–863.

Chapter 3

Practical Procedure to Set Up and Enhance the DSSC

3.1 Introduction

While the equipment and practical procedure required to fabricate and characterize DSSCs with efficiency values close to the global record are not trivial, they are not, however, necessary for developing and testing experimental ideas aimed to enhance or modify the DSSC performance. In contrast, the production and testing of laboratory-grade DSSCs is relatively easy and inexpensive. This laboratory-friendly feature, combined with the diverse range of initial materials utilized in making their components and the different preparation methods to synthesize the initial materials, makes DSSCs a useful case for a variety of investigations, especially on the aspects generally involved in photovoltaics and optoelectronics.
This chapter presents step-by-step fabrication procedure of laboratory-grade DSSCs and provides approaches to optimize their performance through examining the aspects pertaining to the photo-electrode component.

3.2 Reference Samples Preparation and Characterization

The following list of materials were used to prepare the reference samples:

- Titania paste (Man Solar B.V., Netherlands) prepared by P25 TiO_2 nanopowder without binder.
- N719 dye (Solaronix, Switzerland) as a synthesized dye,
  Concentrated aqueous solution of Hibiscus (Man Solar B.V., Netherlands) as a natural dye.
- Iodine-based electrolyte (Man Solar B.V., Netherlands).

- FTO substrate (Man Solar B.V., Netherlands) on soda-lime with dimensions of 2.5 × 4 cm^2 and 3 mm thickness, offering sheet resistance of around 30 Ω/sq and visible transmittance of nearly 80%.

To set up the cell following steps were followed:

Step 1. Two pieces of FTO substrate were cleaned with detergent, acetone and ethanol respectively in an ultrasonic bath for 10 minutes, followed by rinsing with distilled water and ethanol and drying with N_2 flow.

Step 2. On one the substrates, a layer of TiO_2 paste was deposited using the tape casting (doctor blade) method: an adhesive tape of nearly 30 µm thickness with a circular hole of 0.8 cm diameter (0.5 cm^2 area) was used to cover the substrate as the mask and then the paste was deposited by sliding a glass rod.

Step 3. After 1 h for drying the paste layer on a level surface, the mask was detached and sintering at 450 °C was performed to decompose and remove the organic constituents of the paste and improving the layer porosity. To avoid the thermal cracking, a sintering cycle with the slow heating rate of 5 $°C.min^{-1}$ was programmed as: 15 min at 200 °C, 15 min at 325 °C and 30 min at 450 °C.

Step 4. The synthesized dye solution was prepared by dissolving N719 dye powder in anhydrous ethanol in order to obtain 0.4mM concentration. The Hibiscus solution was used as-received. Then the sintered layers were immersed in 100 mL of the dye solutions for 24 h in darkness to perform an efficient soaking process. Afterwards, in order to remove the extra deposited dye molecules, the dyed layers were rinsed with anhydrous ethanol and distilled water, for N719 and Hibiscus respectively.

Step 5. The second FTO substrate, which previously was drilled with a 1 mm diamond-coated drill bit, was used to prepare the counter-electrode through sputtering deposition of Pt/Pd layer for 20 seconds.

Step 6. A bi-adhesive tape of nearly 40 µm thickness with a circular hole identical to that of the mask was applied on the photo-electrode, leaving the mesoporous layer unaffected to create a circular gap between the two electrodes.

Step 7. The counter-electrode was then placed on the photo-electrode in a way that the small hole is in front of the mesoporous layer. Then the electrodes were put under pressure for several minutes to seal the cell completely.

Step 8. A small volume of nearly 10 µL of the electrolyte was dropped on the counter-electrode hole and then the cell was placed inside a vacuum chamber to

conduct the electrolyte infiltration into the circular gap. Finally, the small hole on the counter-electrode was sealed with piece of tape.

Some of the processing steps are summarized in Figure 3.1.

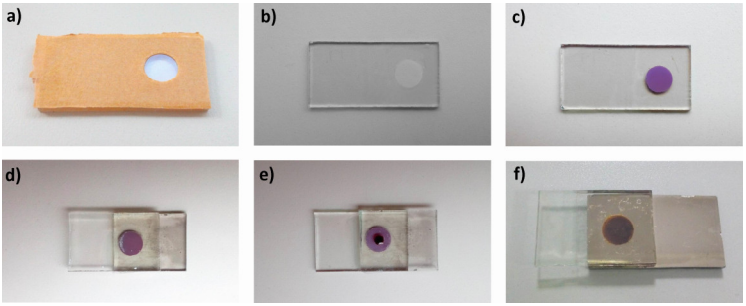

Figure 3.1. *An illustrated summary for the sample's set up; (a) masking the photo-electrode substrate; (b) the photo-electrode after depositing the paste and sintering; (c) the dye-loaded mesoporous layer; (d) the photo-electrode and counter-electrode assembled with a bi-adhesive tape; (e) before vacuum infiltration of electrolyte; (f) the prepared sample.*

The result of I-V measurements of the cells is illustrated in Figure 3.2. The obtained values of V_{OC} and J_{SC} are around 409 mV and 425 µA·cm^{-1} for the Ru-based DSSC, and 404 mV and 349 µA·cm^{-1} for the Hibiscus-based one, with a fill factor of nearly 0.58 and 0.56, resulting in efficiency value of 0.1% and 0.08% for each one respectively. The values are more than 100 time less than the global record indicating that for both samples V_{OC} and J_{SC} are below the desired range.

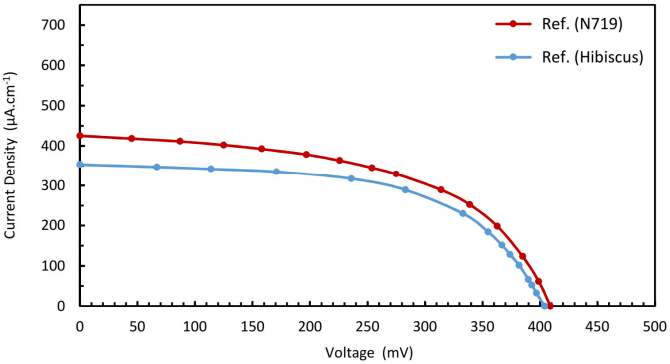

Figure 3.2. *I-V measurement curves of the reference samples.*

Expecting the highest V_{OC} value of a TiO_2/Iodine based DSSC in the range of 600 – 700 mV [1], the dropped value of V_{OC}, is more compromisable than the shortcoming in J_{SC} values; in fact, the major flaw is resulted from the low value of photocurrent. As discussed in Chapter 2, several factors are responsible for photocurrent failure in DSSCs, including the inability of dye molecules to capture a wide range of light wavelengths or weak electron injection to the TiO_2. But more importantly, this condition could be due to the morphological and structural problems in the TiO_2 mesoporous layer that result in low volume of dye loading and poor electrolyte infiltration, or inferior electron diffusion rate.

The first factor can be analyzed through absorption spectroscopy, also in order to compare how the two different dyes work under similar condition. Figure 3.3 shows absorbance spectra of diluted N719 and Hibiscus dyes in the wavelength range of 200 – 900 nm. Surprisingly, the absorption behavior of both molecules are similar to each other and even a slightly higher absorption is observed for Hibiscus molecules in the range of 550 – 900 nm. This result indicates that the major difference in performance of utilized dyes could be mainly regarding the anchoring condition to TiO_2 surface and the charge injection quality. In fact, N719 molecule enjoys four carboxylic groups (COOH) at the end of the pyridyl rings that form a strong bonding with the TiO_2 surface by donating a proton to the TiO_2 lattice [2]. This feature improves the dye injection and more importantly, a longer stability of the absorbed molecule is resulted, which is an issue in some natural dyes.

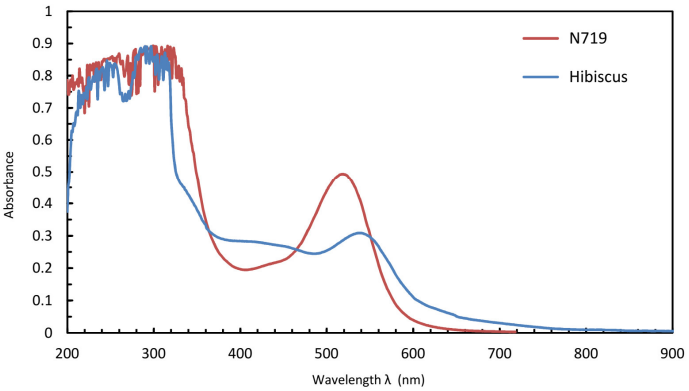

Figure 3.3. *Absorbance spectra of diluted N719 and Hibiscus dyes.*

However, since N719 is the common dye for most of the global records of DSSC efficiency, the main drawback concerning our cell must be caused by the two other reasons. Thus, in the following sections, we focus on two individual approaches to

improve the efficiency of our laboratory-grade DSSC by modifying the features of the TiO_2 mesoporous layer through the synthesis of enhanced pastes.

3.3 Enhanced Samples by Modification of TiO_2 Paste

Titania pastes for DSSC are usually prepared by mixing TiO_2 nanoparticles with organic additives such as binders and dispersants in suitable solvents. In this study, two different recipes were prepared based on the utilized solvent-binder couple, (1) polyethylene glycol (PEG) binder in an aqueous-based solvent and (2) ethyl cellulose (EC) binder in a terpineol-based solvent. Acetic acid and the nonionic surfactant Triton X-100 were used as the dispersant for P25 TiO_2 nanopowder in both recipes. We tried to keep the TiO_2 content of the both pastes around 20 – 25 wt%. The description about the preparation steps of the pastes is followed.

3.3.1 Experimental Procedure

- Recipe A

TiO_2 (1 g), preheated at 100 °C for 15 min to remove the absorbed water on the particles surface, was ground in an agate mortar with 3 mL ethanol for several minutes until complete evaporation of ethanol. Then again 3 mL ethanol was added and the content was carefully transported to a glass vial where the particles dispersion continued by magnetic stirring. Meanwhile, 0.2 mL of acetic acid (0.05M) and a small amount of Triton X-100 (about 0.1 mL) were added. After mixing for 10 min, ultrasonic dispersion was performed for 30 minutes. In another glass vial, 1 g of PEG (35 kDa) was dissolved in a solution of 3 mL distilled water and 1 mL ethanol. Then the content of the second vial was added to the first one. The obtained mixture was stirred bar overnight to increase the viscosity.

- Recipe B

The first step was carried out similar to the Recipe 1 to obtain the mixture of the first vial. In the second vial, 0.5 g of EC (viscosity 10 mPa.s) was dissolved in 5 mL ethanol. Then, 5 mL α-terpineol was added and stirring continued for 1 h. Finally, the content of second vial was added to the first one and the obtained mixture was stirred bar overnight.
The deposition, dye absorption and heat-treatment of the mesoporous layers were performed with similar approach explained for the reference sample (Ref. N719). Accordingly, two DSSCs were assembled, namely Sample A and B, with similar other components to that of the reference sample.

3.3.2 *Results and Discussion*

The I-V measurement curves of the Samples A and B in comparison with that of the reference sample are illustrated in Figure 3.4. Table 3.1 provides the details regarding I-V measurement results. In Figure 3.5, the isothermal N_2 physisorption curves of the samples scratched after deposition and the one regarding the employed initial constituent of P25 nanoparticles are depicted and the derived details are reported in Table 3.2. Moreover, the cross-section SEM images of different samples are shown in Figure 3.6.

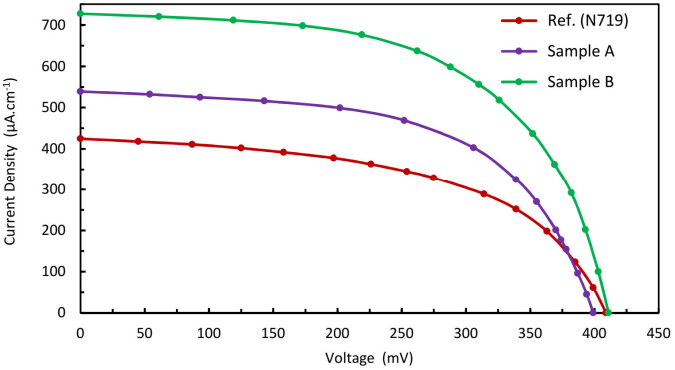

Figure 3.4. *I-V measurement curves of the Samples A and B in comparison with that of the reference.*

Table 3.1. *The I-V curve parameters for Samples A and B and the reference sample regarding Figure 3.4.*

Samples	V_{OC} (mV)	J_{SC} (mA.cm^{-2})	F.F	η%
Ref. (N719)	410	0.44	0.54	0.10
Sample A	404	0.54	0.59	0.13
Sample B	411	0.73	0.61	0.19

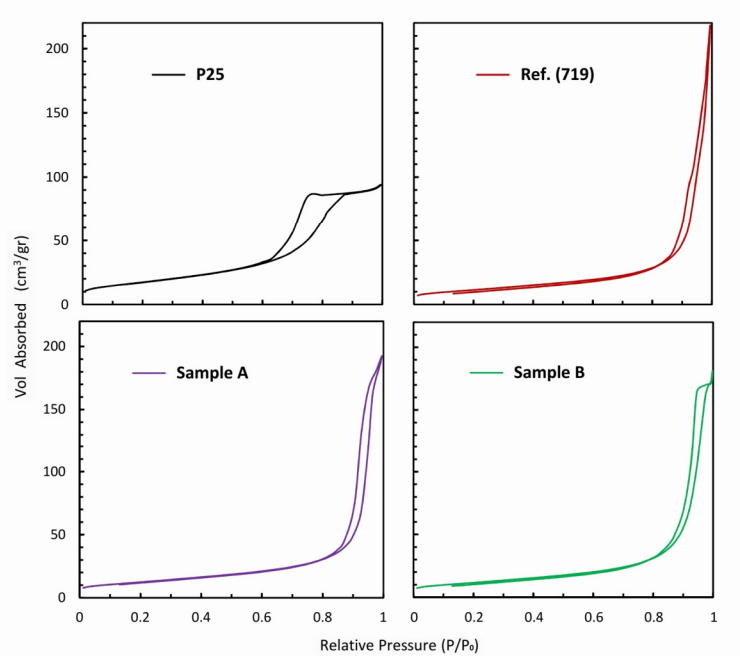

Figure 3.5. *The isothermal N_2 physisorption curves of the employed TiO_2 nanoparticles (P25) and the reference sample, in addition to curves belonging to Samples A and B.*

Table 3.2. *The derived parameters of the isothermal N_2 physisorption analysis for the Samples A and B and the reference sample in addition to the one regarding the employed initial constituent of P25 nanoparticles.*

Samples	**BET Surface Area ($m^2 \cdot g^{-1}$)**	**Total Pore Volume ($cm^3 \cdot g^{-1}$)**	**Average Pore Size (A°)**
P25	62.8 ± 0.17	0.147	83.5
Ref. (N719)	36.5 ± 0.10	0.267	255.3
Sample A	43.8 ± 0.10	0.286	266.4
Sample B	42.6 ± 0.10	0.297	267.6

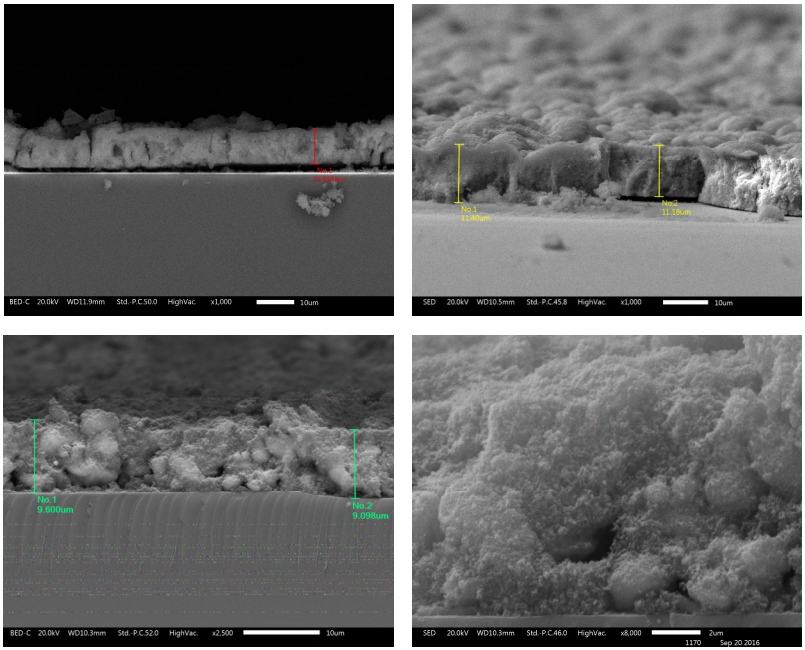

Figure 3.6. *The cross-section SEM images of TiO_2 mesoporous layers (a) reference sample, (b) Sample A, (c) Sample B. (d) An image of higher magnification for Sample B.*

Figure 3.4 shows that in comparison with the reference sample, both samples display a noticeable increase for the values of J_{SC} while the V_{OC} values are not affected. This result is in accordance with the theoretical discussion in Chapter 2 about the origin of V_{OC} and I_{SC} values; employing an identical electrolyte and same chemical compound of the semiconductor results in nearly equivalent values for V_{OC}, while the I_{SC} values could be considerably affected just by the morphology and crystalline structure of the semiconductor layer. As reported in Table 3.1, the improvement of I_{SC} is more notable in Sample B, resulting an efficiency value of almost two times higher than the one of the reference sample.

The isothermal N_2 physisorption curves of the samples in Figure 3.5 and the derived parameters reported in Table 3.2 provide a basis for the difference observed for I – V curves. A plateau region at high values of relative pressure P/P_0, indicating the presence of mesoporous solids is observed for Sample B, and to lesser extent for Sample A, while it is hardly visible in the reference sample. In Sample A the adsorption branch can be classified as Type II isotherm, according to IUPAC classification [3], whereas the reference sample displays Type IV(a) isotherm. As

reported in Table 3.2, compared with the employed nanoparticles, preparing the paste is accompanied with a reduction in surface area values but improvements in the values of pore volume in all samples. A more proper combination of both features could be the reason for better I_{SC} value in Sample B.

An indirect reasoning can also be provided by the cross-section SEM images depicted in Figure 3.6. Poor adhesion to the substrate and inferior pore structure is observed for the deposited layer of the reference sample which improves for Sample A and culminated in Sample B, indicating the superior properties of EC/terpineol for paste preparation. On the other hand, noticeable agglomeration of nanoparticles is observed for both samples that could justify the still low values of photocurrent compared with high-quality DSSCs; however, as shown in Figure 3.6(d), a porous sponge-like morphology is observed in high magnification mode.

As another result obtained in this Chapter, we can point out to the effects of the initial nanoparticles features employed for preparing the pastes, especially concerning the surface area values that were dictated by the value of the P25 nanoparticles. Thus, an initial nanoparticles of higher quality can improve the overall efficiency.

3.4 References

1. Docampo, P.; Guldin, S.; Leijtens, T.; Noel, N.K.; Steiner, U.; Snaith, H.J. Lessons Learned: From Dye-Sensitized Solar Cells to All-Solid-State Hybrid Devices. *Adv. Mater.* **2014**, *26*, 4013–4030.
2. Qin, Y.; Peng, Q. Ruthenium Sensitizers and Their Applications in Dye-Sensitized Solar Cells. *Int. J. Photoenergy* **2012**, *2012*, 1–21.
3. Thommes, M.; Kaneko, K.; Neimark, A. V.; Olivier, J.P.; Rodriguez-Reinoso, F.; Rouquerol, J.; Sing, K.S.W. Physisorption of gases, with special reference to the evaluation of surface area and pore size distribution (IUPAC Technical Report). *Pure Appl.*

Chapter 4

Synthesis of TiO_2 Nanocrystalline Particles

Parts of this chapter has been published in:

M.Nateq and R.Ceccato, **"Sol-Gel Synthesis of TiO_2 Nanocrystalline Particles with Enhanced Surface Area through the Reverse Micelle Approach",** Accepted in *Advances in Materials Science and Engineering*, **manuscript number 1567824**
DOI:

4.1 Introduction

As already discussed in Chapter 2, enhancing the DSSC efficiency through improving the cell photocurrent can be followed by modifying the morphological and structural features of the semiconductor layer, since this component is responsible for two main tasks; (1) acting as a support for dye molecules; and, (2) transporting the photoexcited electrons from the dye to the TCO film. To fulfil the first task efficiently, possessing a high value of surface area is essential to load larger volume of the dye and therefore, increasing the amount of generated charge. This point is particularly important since the optimal performance of the conventional dye molecules is only achieved if just a monolayer of dye molecules is adsorbed on the semiconductor surface [1]. Therefore, for a particular dye, increasing the semiconductor surface area is the only possible solution to increase the maximum number of dye molecules involving in the charge generation process. Moreover, the necessity of dye molecules regeneration by the oxidizing species of the electrolyte entails a well-established surface contact between the dye monolayer and the electrolyte component. This requirement is achieved if only a mesoporous semiconductor with large volume of interconnected pores is utilized in which, a complete infiltration of electrolyte ensures the regeneration of all dye molecules and therefore, maximizing the charge generation.
Fulfilling the second task, however, is of more physical and practical complexity. The charge transport performance in nanocrystalline materials, as already explained in Chapter 2, is largely deteriorated in comparison with single crystals due to the

presence of sub band gap trap states that decrease the electron mobility and therefore, charge diffusion coefficient [2-6]. Since one of the main contributing factors in creating sub band-gap trap states is the high density of grain-boundaries, synthesizing mesoporous particles with larger crystallite size is considerably preferred. In an ideal condition, we are looking for single-crystalline mesoporous particles in which, the crystallite size and particle size are almost identical. To reach this goal requires using low-temperature approaches since inducing the crystallinity and obtaining large values of crystallite size through post-calcination and high-temperature approaches results in pore collapse and severe degradation of surface area value.

For the case of TiO_2, it has already been known that the DSSCs utilizing narrow-size distributed mesoporous anatase nanoparticles with high values of surface area and pore volume are much more effective in improving the charge generation and charge transfer properties [7,8]. In this chapter, the synthesis of TiO_2 nanoparticles with suitable features for their use in DSSC devices is followed.

As a low-temperature approach, the sol-gel synthesis has been successfully applied for preparing nanocrystalline metallic oxide materials including TiO_2. In general, this method involves the hydrolysis and condensation of a metal alkoxide such as titanium(IV) isopropoxide and yielding intermediate oxo-hydroxide spices which eventually form the metal oxide [9,10]. However, precise controlling of hydrolysis step through adjusting the sol pH and temperature is critically essential to obtain homogeneous nanoscale oxide networks [4]. Moreover, the as-synthesized precipitates are generally amorphous and a post-calcination over 300 °C is required to obtain the anatase phase, whereby the inevitable particle size increase due the agglomeration causes collapsing the pore structure and surface area reduction [11]. Consequently, although sol-gel synthesis routes are capable of large-scale production of TiO_2 nanoparticles with high surface area, limitations still exist, including particles aggregation and wide size distribution [3].

A better control on the shape uniformity, size distribution and crystallinity of nanoparticles can be obtained through the surfactant-mediated sol–gel route by employing the reverse micelles [11-14]. This method provides a controlled synthesis approach whereby the hydrolysis of the precursor is confined to the nanodroplets of water which are previously trapped and stabilized in a dry organic nonpolar solvent through a shell of surfactant molecules separating the polar and the non-polar domains. The thermodynamic stability of such a system containing two immiscible liquids is by the virtue of the amphiphilic nature of surfactant molecules whereby, the hydrophilic heads of the molecules cover the surface of water nanodroplets while the hydrophobic tails align outwards in the nonpolar solvent. The subsequent reduction in the interfacial free energy results in the spontaneous formation of water nanodroplets dispersed in the nonpolar solvent. These monodispersed spherical surfactant-covered water pools, called reverse micelles, provide excellent reaction

sites for the formation of nanoparticles as the surfactant shell acts as a surface agent, limiting the future growth and prevents the particles from aggregation and coalescence [15-17]. Besides, this method impedes the precipitation of metal hydroxide due to probable uncontrolled hydrolysis and condensation of the alkoxide, which leads to the formation of heterogeneous nucleation sites and therefore, generation of large clusters with broad size distributions. [18].

The synthesis of TiO_2 nanoparticles via the reverse micelles method involves three stages: (1) formation of a water in oil microemulsion environment as the reverse micelles in the water/solvent/surfactant system; (2) adding the alkoxide precursor solution, such as titanium(IV) tetra-isopropoxide to trigger the hydrolysis reaction in the reverse micellar environment and formation of nanoscale TiO_2 network; and (3) washing or removal of the surfactant from the system to obtain the nanocrystalline powders. Several factors determine the final features of the obtained nanoparticles, among which the choice of the surfactant is the fundamental one. Different types of surfactant including AOT [19,20] and SDS [21] as anionic surfactants and also Brij and Tween series [22] as well as Triton X-100 [23-25] as the nonionic ones have been employed for the surfactant-mediated sol–gel synthesis of TiO_2. The results show that in addition to affect the shape and morphology of nanoparticles, the surfactant structure plays a decisive role in all synthesis stages. The quality of the gel and the subsequent nanoparticles strongly depends on the kinetics of the hydrolysis step [11,23]. Upon the addition of TTIP solution to the reverse micelle environment, the surfactant layer is the barrier against the alkoxide hydrolysis; however, the microemulsion is a dynamic system and the surfactants involved in formation of the layers repeatedly leave the micelles and are replaced by others that freely move in the solvent [14]; providing the exchange of materials throughout the barrier with the so called intermicellar exchange rate. Thereafter, the nucleation initially begins on the micelles edges and continues inwards with the arrival of more TTIP fed via the intermicellar exchange [15]. So the barrier that determines the intermicellar exchange rate and thus, the kinetics of the hydrolysis step depends on the rigidity of the micelle interface [15]. In a microemulsion system with a high interfacial rigidity, formation of more stable water pools leads to obtaining nanoparticles with smaller crystallite size and narrow size distributions due to the gradual hydrolysis of titanium alkoxide [11,23]. A surfactant with a longer hydrocarbon chain can prohibit accessing the water inside the micelles more effectively whereby the interfacial rigidity increases. Besides, a lower area-per-molecule adopted by the surfactant leads to a higher packing density of the interfacial film, and thus a higher rigidity [12,15]. In addition to the hydrolysis part, the last step involving the removal of surfactant molecules from the gel significantly affect the final product quality as well; since the remaining organic molecules degrade the nanoparticles surface properties. Here nonionic surfactants provide better applicability owing to easier removal procedure compared to the ionic and

cationic ones [26]. Triton X-100, a polyoxyethylene derivative, is a nonionic surfactant of nearly 50 square angstroms surface area with a hydrophilic chain containing an average of 9.5 ethylene oxide units; which is longer than the lipophilic part made of an aromatic hydrocarbon chain [27]. Having such properties, Triton X-100 is a promising candidate for template synthesis of nanoparticles via reverse micelle approach.

The other variant affecting the quality of synthesized nanoparticles is the molar ratio of initial compounds. Several studies [15-17] have shown an increase in particle size with increasing the precursor concentration. Moreover, since the volume of trapped water pools determines the reverse micelles radius, it is possible to control the size of nanoparticles through adjusting the molar ratio of the water to surfactant, S, as W= $[H_2O]/[S]$. Generally, decreasing the ratio leads to smaller water nanodroplets and consequently smaller particles [12,15] which can be attributed to the effect of water structure inside the water pool on the interfacial layer rigidity. In a system with a low W ratio, the small number of water per surfactant molecules induces a strong interaction between water molecules and the hydrophilic heads of the surfactant, as almost all of the water molecules inside the water pools can be considered as "bound". This condition leads to a high interfacial rigidity and therefore, slowing down the intermicellar exchange and low growth rate. On the contrary, with a higher W ratio, the volume of water nanodroplets increases; whereby the condition for a portion of water molecules changes from "bound" to "free" state, resulting less stable water pools and accelerated intermicellar exchange and fast growth rate [15,16].

In addition to the high value of the surface area, shape uniformity and narrow size distribution, the higher crystallinity of the as-prepared powder is considered as another factor defining the nanoparticles quality as already disscused in the introduction part. Owing to lower density of trap states and thus, larger diffusion rates of photo-excited electrons [28], the photocatalytic activity of TiO_2 nanoparticles is strongly enhanced by increasing the crystallinity which could be achieved through a high-temperature thermal treatment. However, due to the agglomeration of nanoparticles during the post-calcination treatment and the subsequent collapse of the pore structure and surface area reduction, preparing highly-crystalline as-prepared TiO_2 nanoparticle without further requirement for high-temperature crystallization is particularly favoured [11]. As a logical extrapolation, refluxing the solvent at temperatures considerably lower than those required for the traditional calcination process may be able to crystallize the amorphous nanoparticles synthesized and encapsulated in micellar cavities without significant damage to the micellar structures.

In this chapter, we investigate the effects of water-to-surfactant molar ratio and the refluxing time on the surface area, porosity and crystallite size of TiO_2 nanoparticles obtained from reverse micelle method in water/cyclohexane/Triton X-100 system.

4.2 Materials and Method

4.2.1 Synthesis Procedure

Titanium(IV) isopropoxide (TTIP) (ABCR, Germany), cyclohexane (Cy) and Triton X-100® (TX) (Sigma-Aldrich, USA) were used as precursor, solvent and surfactant respectively, without further purification, and distilled water was applied to initiate the hydrolysis. All the amounts of the reagents were kept fixed to the following values, in molar ratios: $[H_2O]/[TX]/[TTIP]$ = 10/1/1, whereas cyclohexane volumes were evaluated from the ratio: $[TTIP]/[Cy] = 5 \cdot 10^{-4}$ mol·ml^{-1}, as reported in literature [29]. Figure 4.1 shows the schematic representation of the synthesis procedure. Firstly, the reverse micellar environment was prepared by the dissolution of TX in Cy at room temperature and stirring for 10 minutes and then the drop-wise addition of stoichiometric amount of distilled water followed by a further 30 minutes stirring. In the next step, the solution of TTIP in Cy was added to the reverse micelle solution and immediately the powder formation occurred. All the obtained suspensions were left under stirring for 30 min before stopping the reaction (sample with no reflux) or starting the reflux step at 80 °C for different times. Further step provided the removal of the micellar environment by adding to the suspensions a fixed volume of water/ethanol = 1/1 solution and leaving them in a separation funnel until the complete separation between oil and aqueous phases occurred. Then powders were filtered and washed 4 times with the same amount of water; a drying was performed on the powders at 80 °C overnight. Obtained products were labelled R_x samples, with x = 0, 1, 2, 15, 24 representing the time, as hours, of the refluxing step of the suspension. Following similar synthesis procedure, two other samples were prepared with refluxing time of 24 h through changing the $W = [H_2O]/[TX]$ molar ratio from W = 10 to 5 and 2. This second group of products were labelled W_5 and W_2 samples. Finally, a fraction of all samples were taken for heat-treated at 500 °C for 2 h in a static air oven. Figure 4.1 summarizes the steps for preparation of TiO_2 nanoparticles.

4.2.2 Characterization

The as-prepared and treated powders were characterized by several techniques. Density measurements were performed by a Micromeritics 1035 helium pycnometer (Micromeritics, USA) and N_2-sorption isothermal analyses were obtained by a Micromeritics ASAP 2010 porosimeter (Micromeritics, USA). Before the analysis, each sample was degassed at a final pressure < 1.3 Pa. The assessment of their surface area values was performed by using BET equation, applied in the range: $0.05 < P/P_0 < 0.33$. Then the BJH model was applied in order to classify the pore size distribution curves. From the above data, primary particle dimensions were

evaluated, under the assumption of a spherical symmetry, using the following equation:

$$d = \frac{6}{SSA \cdot \rho} \quad (4.1)$$

where d is the primary particle dimension, SSA means the specific surface area value and ρ represents the skeletal density.

SEM micrographs were obtained by JSM-5500 instrument (JEOL, Japan), operating at voltage of 10 kV. FT-IR measurements were performed on powders dispersed into KBr pellets using an Avatar 330 spectrophotometer (ThermoNicolet, USA). TEM images, SAED patterns and regarding indexing graphs were obtained using a STEM microscope, Talos™ F200S S/TEM instrument (ThermoFisher, USA), operating under accelerating voltage of 200 kV. The XRD spectra were collected with a Rigaku IIID-Max powder diffractometer (Rigaku, Japan), employing Cu Kαα1 radiation (λ = 0.154056 nm) and a graphite curved monochromator, set on the diffracted beam. Experimental spectra were evaluated, in terms of phase content and line profile analysis, by using MAUD software, a derived Rietveld method for quantitative analysis, associated with Warren-Averbach theory for the crystallite size evaluation [30].

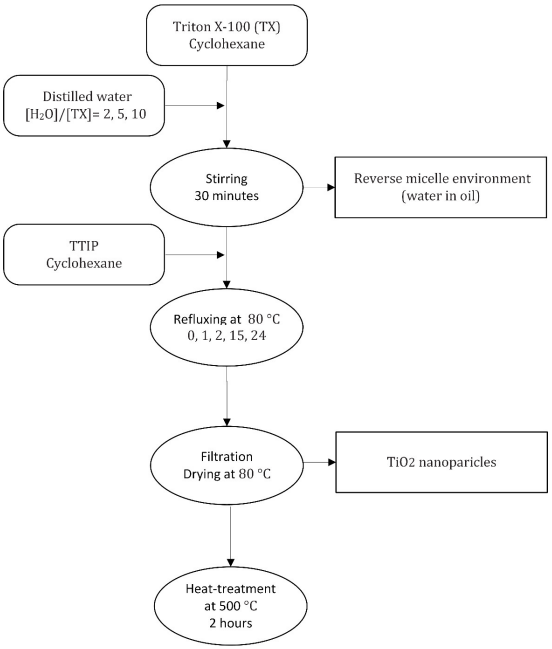

Figure 4.1. *The flowchart summarizing the steps for preparation of TiO_2 nanoparticles.*

4.3 Results

The results of the X-ray diffraction analysis, helium pycnometry measurements and also N_2 physisorption analysis are reported in Table 4.1 and Table 4.2, regarding the as-prepared and treated powders respectively. Figure 4.2 provides a visual comparison for as-prepared R_0 and R_{24} samples, followed by two pairs of high and low magnification SEM images. In Figure 4.3, for as-prepared powders synthesized through different refluxing time and W ratio, the FT-IR spectra are depicted, comparing all samples after being washed for four times. Moreover, for the as-prepared R_{24} sample, the FT-IR spectra after different numbers of washing are compared with the spectrum of the treated R_{24} sample. In Figure 4.4, the TEM images of R_{24} (W_{10}) and W_2 samples in as-prepared and treated conditions are shown in addition to regarding SAED patterns and indexing graphs, followed by X-ray diffraction patterns of all samples in Figure 4.5. The isothermal N_2 physisorption curves of the samples in the as-prepared and the treated condition are illustrated In Figure 4.6. The samples porosity features are reported in terms of the total pore volume and average pore diameter in Figure 4.7, as well as the pore size distribution and the modal pore diameter in Figure 4.8, respectively.

Table 4.1. *Structural and morphological parameters of the as-prepared TiO_2 samples.*

Sample	**Phase**	**Crystallite Size (nm)**	**Density ($g \cdot cm^{-3}$)**	**BET Surface Area ($m^2 \cdot g^{-1}$)**	**Particle Size[2] (nm)**
R_0	Amorp.	n.e.[1]	1.840±0.005	15.8±0. 9	205.4±0.2
R_1	Amorp.	n.e.	1.803±0.005	74.4±0.3	37.9±0.4
R_2	Anatase	4.1±0.6	1.471±0.001	34.5±0.2	118.2±0.7
R_{15}	Anatase	6.1±0.3	2.173±0.006	77.6±0.6	35.6±0.3
R_{24} (W_{10})	Anatase	6.3±0.5	3.133±0.006	178.8±1	10.7±0.6
W_5	Anatase	5.4±0.4	3.180±0.040	239.4 ±3	7.9±0.2
W_2	Anatase	4.6±0.1	2.753±0.005	224.6 ±3	9.7±0.4

1. Not available

2. Calculated under the assumption of spherical symmetry according to Equation 4.1.

Table 4.2. *Structural and morphological parameters of TiO_2 samples treated at 500 °C for 1 h.*

Sample	**Phase**	**Crystallite Size (nm)**	**Density ($g \cdot cm^{-3}$)**	**BET Surface Area ($m^2 \cdot g^{-1}$)**	**Particle Size[2] (nm)**
R_0	Anatase	15.3±0.2	3.51±0.02	101.6±0.6	15.8±0.1
R_1	Anatase	17±2	3.51±0.02	74.4±0.3	22.9±0.1
R_2	Anatase	15±2	3.66±0.02	104.6±0.5	15.6±0.1
R_{15}	Anatase[1]	15±1	3.63±0.02	116.0±0.5	14.2±0.1
R_{24} (W_{10})	Anatase[1]	13.6±0.2	3.67±0.01	123.1±0.4	13.3±0.1
W_5	Anatase[1]	13.7±0.2	3.75±0.02	126.6±0.7	12.9±0.1
W_2	Anatase	13.4±0.1	3.62±0.06	121.2±0.3	13.1±0.1

1. Some brookite phase is present (< 5% weight).

2. Calculated under the assumption of spherical symmetry according to Equation 4.1.

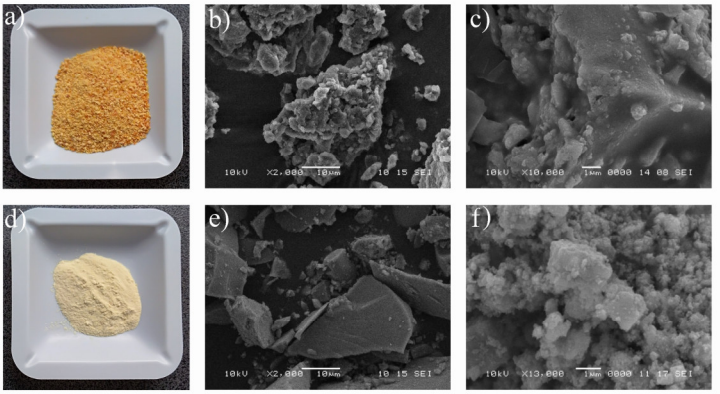

Figure 4.2. *The as-prepared R_0 sample (a), and SEM images under the low (b), and high magnification (c), in comparison with the as-prepared R_{24} sample (d), and its SEM images under low (e), and high magnification (f).*

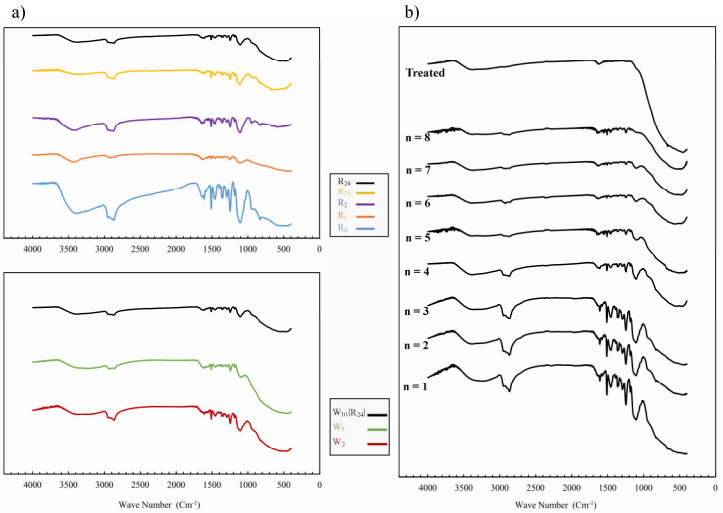

Figure 4.3. *The FT-IR spectra of as-prepared powders synthesized through different refluxing time (upper part) and W ratio (lower part) after being washed for four times (a); and the FT-IR spectra of the as-prepared R_{24} sample after different numbers of washing (n = 1 to 8) compared with the spectrum of the treated R_{24} one (b).*

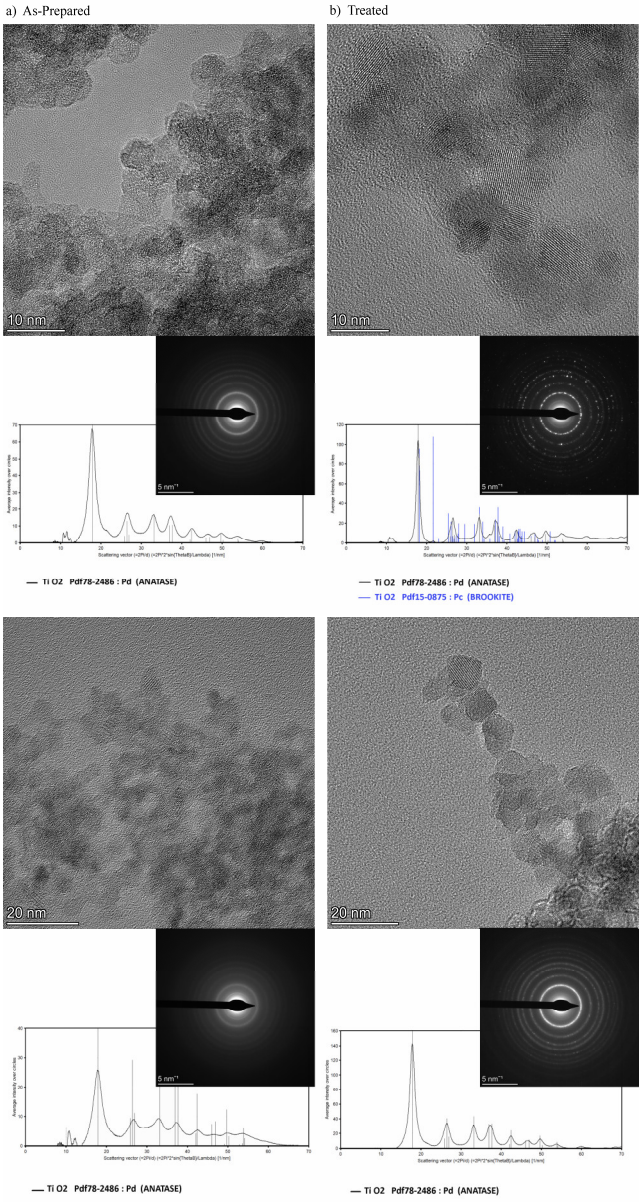

Figure 4.4 *TEM images of TiO_2 nanoparticles in the as-prepared state (a), and treated condition (b), in addition to regarding SAED patterns and indexing graphs for the samples R_{24} (W_{10}) (upper parts) and W_2 (lower parts).*

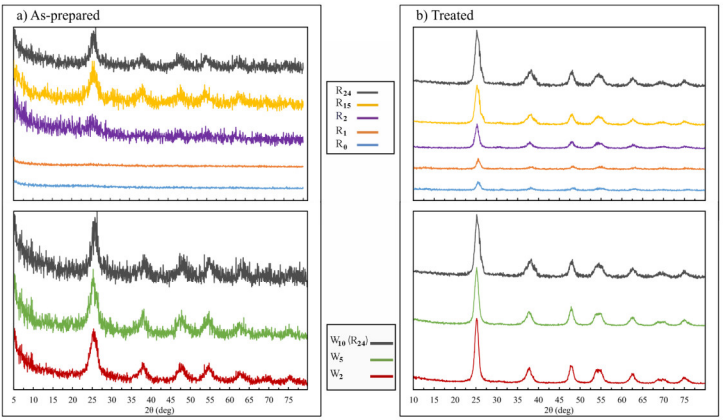

Figure 4.5. *X-ray diffraction patterns of TiO_2 nanoparticles in the as-prepared state (a), and the treated condition (b), obtained through different refluxing time (upper parts) and different water-to-surfactant ratio (lower parts).*

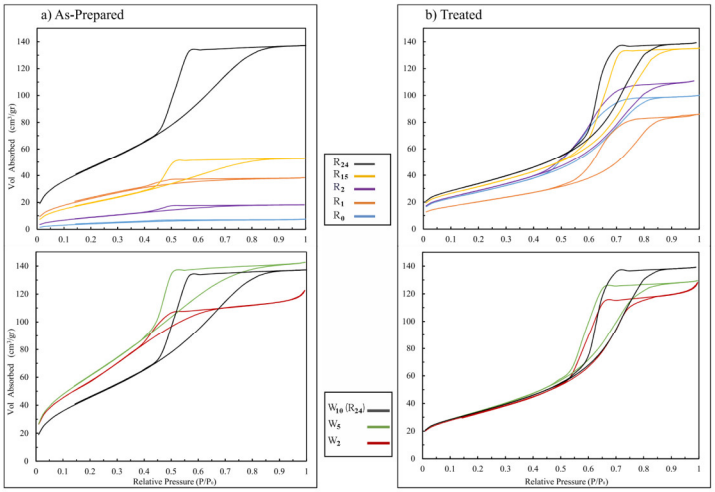

Figure 4.6. *The isothermal N_2 physisorption curves of TiO_2 nanoparticles in the as-prepared state (a), and the treated condition (b), obtained through different refluxing time (upper parts) and different water-to-surfactant molar ratio (lower parts).*

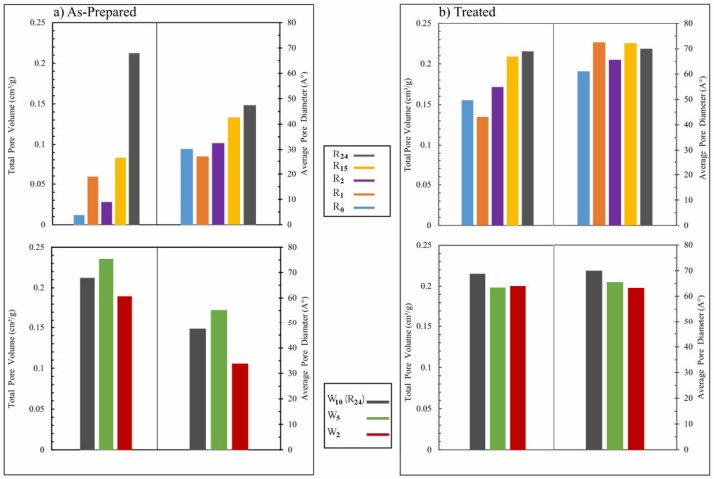

***Figure 4.7**. A comparison for the BJH Adsorption total pore volume and BJH Adsorption average pore diameter of TiO_2 nanoparticles in the as-prepared state (a), and the treated condition (b), obtained through different refluxing time (upper parts) and different water-to-surfactant molar ratio (lower parts).*

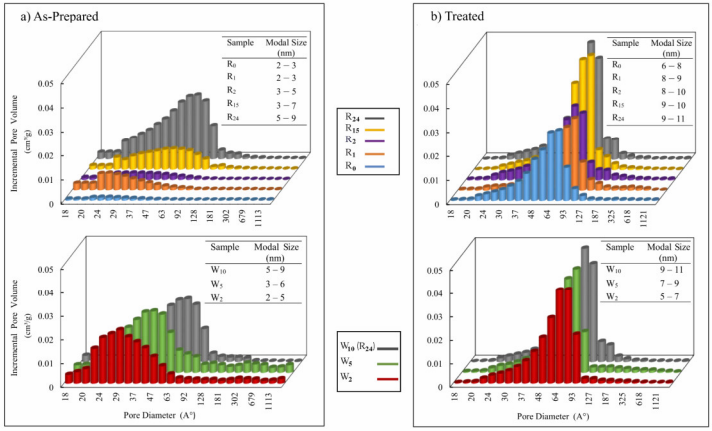

***Figure 4.8.** A comparison for the BJH adsorption pore-size distribution of TiO_2 nanoparticles in the as-prepared state (a), and the treated condition (b), obtained through different refluxing time (upper parts) and different water-to-surfactant ratio (lower parts). The inset tables report the BJH adsorption modal pore diameter values, obtained from the full width at half-maximum height of the distribution curves.*

4.4 Discussion

4.4.1 As-prepared Samples

The first goal of this chapter was to enhance the uniformity and crystallinity of the as-prepared TiO_2 nanoparticles as a function of the reflux time. The powders uniformity was studied in terms of skeletal density, particles dimension and remaining surfactant amount; and the results of XRD analysis and TEM observation were used to investigate the powders crystallinity.

According to the values reported in Table 4.1 for as-prepared samples, as a general trend, the increase of the reflux time leads to higher values of the skeletal density together with the decrease of the particle dimensions. An indirect proof of this feature can be evidenced from SEM micrographs, reported in Figure 4.2 for the samples R_0 and R_{24} comparatively. In low magnification, both samples look like large aggregates of primary particles while some differences could be observed in the high magnification mode: the surface of the R_0 particles appears very smooth and flat, whereas the R_{24} particles looks like more ordered with a prismatic symmetry. Seemingly, aggregates in R_0 are formed since the surfactant is still present, entrapped among the nanoparticles. The presence of –OH groups can act as specific sites for the aggregation of the primary particles afterwards. In Figure 4.3(a), the FT-IR spectra confirm that the surfactant is still present in as-prepared samples after four times of washing; since the absorption peaks attributable to organic residuals are detected, including CH_2 and OH stretching peaks in the range of 2800 to 3000 cm^{-1} and 3000 to 3500 cm^{-1} respectively. However, as the reflux time extends, the intensity of peaks turns out to be considerably small, indicating negligible surfactant contents in the samples R_{15} and R_{24}. Moreover, as shown in Figure 3b for the sample R_{24}, an almost surfactant-free product comparable with the treated sample is possible to obtain by increasing the numbers of washing. For the samples W_5 and W_2 that contained higher amounts of initial surfactant, more remained organic residuals is detected compared with the sample R_{24}, making the required numbers of washing up to nearly double to obtain an almost surfactant-free sample (not shown here). Thus, as the first result, it can be concluded that a sufficiently long reflux time brings about the capability of removing almost all contaminants and results in powders of smaller particle size and higher density; while short refluxing times lead to formation of large particles of lower density values containing organic residuals. The samples R_1 and R_2 display unique behaviors with respect to the R_0 one in most of characterizations results, suggesting that, for lower reflux times, the interactions between the different phases, in organic and aqueous media, are still strong and complex.

Another conclusion derived from the reported data in Table 4.1 is regarding the crystallinity of as-prepared powders: more nanocrystalline anatase phase is obtained

in case of increasing the reflux time, as also shown in Figure 4.5(a) where the XRD spectra of the as-prepared samples are reported as functions of reflux time and W ratio. All samples with 24 h refluxing time are evidently more crystalline than other samples, indicating a higher yield of the hydrolysis-condensation reactions in the micellar environment. However, in the samples of lower W ratio, a slight degradation in crystallinity and a little reduction of crystallite size are identified. This conclusion is confirmed by the TEM observation, as illustrated in Figure 4.4(a) for the samples R_{24} (W_{10}) and W_2 in the as-prepared condition. The TEM analysis shows that both samples are composed of ultrafine uniform spherical nanoparticles with the dimension of 5 – 10 nm that display the lattice fringes. The selected area electron diffraction (SAED) patterns and the corresponding indexing graphs indicate the crystallographic features of anatase phase with the interatomic spacing of $d \approx 3.7\ A^{\circ}$ for (101) planes. In accordance with XRD results, the higher W ratio is associated with increased crystallinity.

In addition to uniformity and crystallinity, enhancing the surface area and porosity features of the as-prepared samples is another goal of this work. The data reported in Table 4.1 indicate that both reflux time and W ratio play a key role on the obtained values for the specific surface area of as-prepared TiO_2 nanoparticles. By increasing the reflux time to 24 h, larger surface area value up to nearly 180 $m^2.g^{-1}$ is obtained which even increases to 220 – 240 $m^2.g^{-1}$ in case of low W ratios, much higher than the reported values for commercial catalysts based on titanium dioxide [31]. In the isothermal nitrogen physisorption curves depicted in the upper part of Figure 6a, a plateau region at high values of relative pressure, P/P_0, is observed for all of the samples, indicating the presence of mesoporous solids. For R_0 and R_1 the adsorption branch can be classified as a composite of Type I and Type II curves, according to IUPAC classification [32], whereas R_2, R_{15} and R_{24} samples display Type IVa isotherms. Moreover, all the curves are characterized by the presence of hysteresis loops, attributable to Type H_4 for the former samples and Type H_{2a} for the latter ones. The results concluded from the physisorption analyses can be interpreted as follow: i) for no or short refluxing times, the gas uptake can be associated with the micropore filling; ii) for longer times, a more complex pore and network structures take place, as referred for many ordered metal oxides [33]; iii) for a low W ratio, the plateau region is less evident, probably due to less amount of mesopores. Complementary details can be obtained through the porosity analysis of the samples in terms of the evaluation of total and average pore volume at relative pressures of $P/P_0 > 0.95$, as indicated for mesoporous solids [33]; and also the distribution curves of pore volume with respect to the pore diameter obtained via the BJH method. The illustrated results in Figures 4.7(a) and 4.8(a) imply that all samples display broad pore distribution curves with a unimodal trend; however, short reflux time leads to very small pore volumes, whereas the reflux for 24 h brings about highest pore volume values, among which, high to intermediate values of W ratio

exhibit higher pore volumes. The observations regarding higher values of surface area and pore volume are in accordance with the previously discussed argument about the advantages of sufficient reflux time in obtaining surfactant-free nanoparticles in terms of better porosity features and surface quality.

4.4.2 Treated Samples

In Table 4.2, the reported values indicate that the reflux time and W ratio are also determining factors on the structural and morphological parameters of the treated samples; however, to a lesser extent compared to the as-prepared ones. Accordingly, the skeletal density increases and the particle size decreases with higher reflux time. Long reflux time and high to intermediate values of W ratio allow to obtain almost fully dense powders with the lowest particle size (samples R_{24} and W_5), However, even for short reflux time and low W ratio, density values of 85 – 90% of the theoretical limit is estimated.

Regarding the XRD spectra in Figure 4.5(b), the qualitative analysis evidences the presence of anatase polymorph; whereas for the samples with longer reflux time, small amounts of brookite is also implied (estimated below 5 wt%), confirming the evolution of titania nanoparticles during thermal treatment above 400 °C. However, the reported values for the crystallite size in Table 2 highlight that the ordered domains of all treated samples (except R_1) fall in the narrow range of 13 – 15 nm; and regardless of the errors due to the simplified model adopted, crystallite size values are quite identical to the calculated particle dimensions. The same result is concluded from the TEM observation, as illustrated in Figure 4b for the samples R_{24} (W_{10}) and W_2 in the treated condition. In comparison with the as-prepared condition, a larger particle dimension up to 10 – 15 nm is observed for both samples and the lattice fringes are more evident. The selected area electron diffraction (SAED) patterns and the corresponding indexing graphs show the crystallographic features of highly crystalline anatase phase, together with a minor amount brookite phase in the samples R_{24} (the peaks marked with blue lines).

The comparison between the BET surface area and particle size value of samples before and after thermal treatment provides a useful criterion for observing the effect reflux time on the obtained nanoparticle features. While the thermal treatment of R_0, R_1, R_2 and R_{15} results in higher surface area values and smaller particle sizes, opposite situation is true for all the samples prepared through 24 h reflux time. A similar trend is also observed for pore volume values since as a result of thermal treatment, the pore volume of short-refluxed samples increases while it decreases for all samples prepared through 24 h reflux time. A possible reason for such different behavior could be addressed to the low crystallinity and remaining surfactant in the former group whereby, the high-temperature approach considerably improves the structural and morphological features; while for the latter group, the

consequence of post-calcination process, is merely the thermally-activated growth of nanoparticles and surface area reduction. However, as it is reported in Table 4.2, in all treated samples (except R_1) the surface areas values still remain high, above 100 $m^2.g^{-1}$. The physisorption curves in Figure 4.6(b) show that all treated samples are classified as mesoporous; however, some differences can be derived from the classification of the isothermal curves. In fact, W_2 sample displays an isothermal curve similar to those for short reflux times, whereas W_5 curve is somehow similar to that of R_{15} sample. Similar to the as-prepared powders, short reflux time leads to Type H_4 hysteresis loops, whereas R_{15}, R_{24}, W_2 and W_5 powders show Type H_{2a} loops, indicating the presence of a more complex network structures. The main discrepancy is observed for R_1 sample which displays also the lowest surface area and total pore volume values.

4.5 Conclusions

In this chapter mesoporous TiO_2 nanoparticles were synthesized through the surfactant-mediated sol–gel in the water-in-oil micellar system of water/cyclohexane/Triton X-100 and the effects of refluxing time and water-to-surfactant molar ratio on the on the surface area, porosity and crystallite size of nanoparticles were studied before and after thermal treatment at 500 C°. It was observed that for the as-prepared samples, by increasing the reflux time to 24 h, the crystallinity and porosity improve considerably and the density and BET surface area increase to nearly 3.133 $g.cm^{-3}$ and 180 $m^2.g^{-1}$ respectively, indicating a significant enhancement for the nanoparticles quality in anatase phase. On the other hand, for the constant reflux time of 24 h, decreasing the water-to-surfactant molar ratio from 10 to 5 and 2 leads to formation of smaller nanoparticles with even higher surface area of around 220 – 240 $m^2.g^{-1}$, while a slight degradation in the crystallinity and porosity of the nanoparticles is observed. Moreover, the step for removing the surfactant from the obtained powders is considerably longer. The thermal treatment of the samples at 500 C° anticipatedly contributes to increase the values of crystallite size and density, a narrower pore size distribution as well as a reduction in surface area values; however, the surface area values of the most of the samples remain over 100 $m^2.g^{-1}$ and the particle size values do not exceed nearly 15 nm.

The obtained values indicate that reverse micelle approach is a feasible and low-cost method to synthesize TiO_2 anatase nanoparticles with high surface area and noticeable porosity features in both as-prepared and thermal treated samples. These powders can be regarded as suitable candidates for the applications such as DSSCs where their crystallinity and surface properties result in considerable effect on the device functionality and efficiency.

.

4.6 References

1. Chen, X.; Mao, S.S. Titanium Dioxide Nanomaterials: Synthesis, Properties, Modifications, and Applications. *Chem. Rev.* **2007**, *107*, 2891–2959.
2. FUJISHIMA, A.; ZHANG, X.; TRYK, D. TiO_2 photocatalysis and related surface phenomena. *Surf. Sci. Rep.* **2008**, *63*, 515–582.
3. Lee, S.; Cho, I.-S.; Lee, J.H.; Kim, D.H.; Kim, D.W.; Kim, J.Y.; Shin, H.; Lee, J.-K.; Jung, H.S.; Park, N.-G.; et al. Two-Step Sol−Gel Method-Based TiO_2 Nanoparticles with Uniform Morphology and Size for Efficient Photo-Energy Conversion Devices. *Chem. Mater.* **2010**, *22*, 1958–1965.
4. Behnajady, M.A.; Eskandarloo, H.; Modirshahla, N.; Shokri, M. Investigation of the effect of sol–gel synthesis variables on structural and photocatalytic properties of TiO_2 nanoparticles. *Desalination* **2011**, *278*, 10–17.
5. Mahoney, L.; Koodali, R. Versatility of Evaporation-Induced Self-Assembly (EISA) Method for Preparation of Mesoporous TiO_2 for Energy and Environmental Applications. *Materials (Basel).* **2014**, *7*, 2697–2746.
6. Tamiolakis, I.; Lykakis, I.N.; Katsoulidis, A.P.; Armatas, G.S. One-pot synthesis of highly crystalline mesoporous TiO_2 nanoparticle assemblies with enhanced photocatalytic activity. *Chem. Commun.* **2012**, *48*, 6687.
7. Zhu, Z.; Zhu, C.; Liu, H.; Wu, Y.; Chen, G.; Lv, T. Synthesis of monodisperse colloidal TiO_2 microspheres and performance of their dye-sensitized solar cells. *Appl. Surf. Sci.* **2014**, *308*, 301–305.
8. Khan, M.A.; Shaheer Akhtar, M.; Yang, O.-B. Synthesis, characterization and application of sol–gel derived mesoporous TiO_2 nanoparticles for dye-sensitized solar cells. *Sol. Energy* **2010**, *84*, 2195–2201.
9. Yahaya, M.Z.; Abdullah, M.Z.; Mohamad, A.A. Centrifuge and storage precipitation of TiO_2 nanoparticles by the sol–gel method. *J. Alloys Compd.* **2015**, *651*, 557–564.
10. Leyva-Porras, C.; Toxqui-Teran, A.; Vega-Becerra, O.; Miki-Yoshida, M.; Rojas-Villalobos, M.; García-Guaderrama, M.; Aguilar-Martínez, J.A. Low-temperature synthesis and characterization of anatase TiO_2 nanoparticles by an acid assisted sol–gel method. *J. Alloys Compd.* **2015**, *647*, 627–636.
11. Rossmanith, R.; Weiss, C.K.; Geserick, J.; Hu̇sing, N.; Ho̊rmann, U.; Kaiser, U.; Landfester, K. Porous Anatase Nanoparticles with High Specific Surface Area Prepared by Miniemulsion Technique. *Chem. Mater.* **2008**, *20*, 5768–5780.
12. Pileni, M.P. Nanosized Particles Made in Colloidal Assemblies. *Langmuir* **1997**, *13*, 3266–3276.
13. Stathatos, E.; Lianos, P.; Del Monte, F.; Levy, D.; Tsiourvas, D. Formation of TiO_2 Nanoparticles in Reverse Micelles and Their Deposition as Thin Films on Glass Substrates. *Langmuir* **1997**, *13*, 4295–4300.
14. Pileni, M.-P. The role of soft colloidal templates in controlling the size and shape of inorganic nanocrystals. *Nat. Mater.* **2003**, *2*, 145–150.
15. Eastoe, J.; Hollamby, M.J.; Hudson, L. Recent advances in nanoparticle synthesis with reversed micelles. *Adv. Colloid Interface Sci.* **2006**, *128–130*, 5–15.
16. Qi, L. Synthesis of inorganic nanostructures in reverse micelles. *Encycl. Surf. Colloid Sci. (2nd Ed.)* **2006**, 6183–6207, 25 pp.

17. Malik, M.A.; Wani, M.Y.; Hashim, M.A. Microemulsion method: A novel route to synthesize organic and inorganic nanomaterials. *Arab. J. Chem.* **2012**, *5*, 397–417.
18. Galkina, O.L.; Vinogradov, V. V.; Agafonov, A. V.; Vinogradov, A. V. Surfactant-Assisted Sol-Gel Synthesis of TiO_2 with Uniform Particle Size Distribution. *Int. J. Inorg. Chem.* **2011**, *2011*, 1–8.
19. Saiwan, C.; Krathong, S.; Anukulprasert, T.; O'rear, III, E.A. Nano-Titanium Dioxide Synthesis in AOT Microemulsion System with Salinity Scan. *J. Chem. Eng. JAPAN* **2004**, *37*, 279–285.
20. Moran, P.D.; Bartlett, J.R.; Woolfrey, J.L.; Bowmaker, G.A.; Cooney, R.P. Formation and gelation of titania nanoparticles from AOT reverse micelles. *J. Sol-Gel Sci. Technol.* **1997**, *8*, 65–69.
21. Cai, W.; Yang, H.; Guo, X. A Facile Synthesis of Nanocrystalline Spherical TiO2 Particles and its Photoluminescent Properties. *Procedia Eng.* **2014**, *94*, 71–75.
22. Lee, M.S.; Park, S.S.; Lee, G.-D.; Ju, C.-S.; Hong, S.-S. Synthesis of TiO_2 particles by reverse microemulsion method using nonionic surfactants with different hydrophilic and hydrophobic group and their photocatalytic activity. *Catal. Today* **2005**, *101*, 283–290.
23. Kluson, P.; Kacer, P.; Cajthaml, T.; Kalaji, M. Preparation of Titania mesoporous materials using a surfactant-mediated sol–gel method. *J. Mater. Chem.* **2001**, *11*, 644–651.
24. Keswani, R.K.; Ghodke, H.; Sarkar, D.; Khilar, K.C.; Srinivasa, R.S. Room temperature synthesis of titanium dioxide nanoparticles of different phases in water in oil microemulsion. *Colloids Surfaces A Physicochem. Eng. Asp.* **2010**, *369*, 75–81.
25. Inaba, R.; Fukahori, T.; Hamamoto, M.; Ohno, T. Synthesis of nanosized TiO2 particles in reverse micelle systems and their photocatalytic activity for degradation of toluene in gas phase. *J. Mol. Catal. A Chem.* **2006**, *260*, 247–254.
26. Hussain, T.; Batool, R. Microemulsion Route for the Synthesis of Nano-Structured Catalytic Materials. In *Properties and Uses of Microemulsions*; InTech, 2017; Vol. i, p. 13.
27. Robson, R.J.; Dennis, E.A. The size, shape, and hydration of nonionic surfactant micelles. Triton X-100. *J. Phys. Chem.* **1977**, *81*, 1075–1078.
28. Ohtani, B.; Ogawa, Y.; Nishimoto, S. Photocatalytic Activity of Amorphous−Anatase Mixture of Titanium(IV) Oxide Particles Suspended in Aqueous Solutions. *J. Phys. Chem. B* **2002**, *101*, 3746–3752.
29. Zhang, R.; Gao, L. Preparation of nanosized titania by hydrolysis of alkoxide titanium in micelles. *Mater. Res. Bull.* **2002**, *37*, 1659–1666.
30. Lutterotti, L. Total pattern fitting for the combined size–strain–stress–texture determination in thin film diffraction. *Nucl. Instruments Methods Phys. Res. Sect. B Beam Interact. with Mater. Atoms* **2010**, *268*, 334–340.
31. Di Paola, A.; Cufalo, G.; Addamo, M.; Bellardita, M.; Campostrini, R.; Ischia, M.; Ceccato, R.; Palmisano, L. Photocatalytic activity of nanocrystalline TiO_2 (brookite, rutile and brookite-based) powders prepared by thermohydrolysis of TiCl4 in aqueous chloride solutions. *Colloids Surfaces A Physicochem. Eng. Asp.* **2008**, *317*, 366–376.

32. Thommes, M.; Kaneko, K.; Neimark, A. V.; Olivier, J.P.; Rodriguez-Reinoso, F.; Rouquerol, J.; Sing, K.S.W. Physisorption of gases, with special reference to the evaluation of surface area and pore size distribution (IUPAC Technical Report). *Pure Appl. Chem.* **2015**, *87*, 1051–1069.
33. Rouquerol, F.; Rouquerol, J.; Sing, K.S.W.; Llewellyn, P.; Maurin, G. Adsorption by powders and porous solid: principles, methodology and applications. *Academic Press*, San Diego **2014**, *ch.11*, 429-438

Chapter 5

Preparation and Characterization of Transparent Conducting Films

Parts of this chapter has been published in:

M.Nateq and R.Ceccato, **"Enhanced Sol–Gel Route to Obtain a Highly Transparent and Conductive Aluminum-Doped Zinc Oxide Thin Film",** *Materials* **2019**, 12, 1744
DOI:10.3390/ma12111744

5.1 Introduction

Transparent conducting films (TCFs) are neccesary components for all photoelectrochemical cells since the photo-electrode must be able to transmit the light inside the cell and at the same time, it is responsible to collect the generated charges and inject them to circuit. Thus having high optical transmission together with low electrical resistivity is a requirement for the photo-electrode that is not fulfilled with the common transparent materials such as glass and conventional polymers. Among the limited number of materials possessing such a property, the most widely utilized are thin films of certain wide band-gap n-type semiconducting oxides like In_2O_3, SnO_2 and ZnO, known as transparent conducting oxides (TCOs) [1]. Here, non-stoichiometric excess of cations or oxygen vacancies can provide a considerable number of charge carriers, causing an intrinsically moderate but usually not sufficient electrical conductivity, which is significantly boosted when properly doped with appropriate elements [2]. However, due to the trade-off between electrical conductivity and optical transmission [3], the quality of a TCO is evaluated by a factor called figure-of-merit (FoM) to consider both properties simultaneously. For this purpose, it is necessary to measure average values of transmittance T, and sometimes reflectance R, generally within the visible wavelengths region, as well as the electrical sheet resistance, R_{sh}. Among different suggested definitions for FoM, the first successful one was defined by Haacke as $\mathrm{FoM} = \mathrm{T}^{10}/\mathrm{R}_{\mathrm{sh}}$ [4], in which the dimension is Ω^{-1}, and a larger value indicates a better performance. With a similar dimension, a more practical definition was proposed by Jain and

Kulshreshtha [3, 5], which evaluates the film performance independent of the thickness:

$$\mathrm{FoM} = -[\mathrm{R_{sh}}.\ln(\mathrm{T})]^{-1}. \quad (5.1)$$

This definition was later modified by Gordon [6], as $\mathrm{FoM} = -[\mathrm{R_{sh}}.\ln(\mathrm{T}+\mathrm{R})]^{-1}$ for applications such as low-emissivity windows equipped with infrared-reflecting glass [7], where the optical absorption is considered more decisive than the mere transmission. There is also a more sophisticated definition proposed by Gruner and modified by Coleman relying on a relationship in which, T and R_{sh} are correlated to $\sigma_{\mathrm{DC}}/\sigma_{\mathrm{OP}}$ as the ratio of dc conductivity to the optical conductivity [8-10]. The derived equation [10] with a similar dimension to Haacke's FoM is:

$$\mathrm{FoM} = 188.5.[\mathrm{R_{sh}}.(\mathrm{T}^{-0.5}-1)]^{-1}. \quad (5.2)$$

The most commonly-used TCO material is indium tin oxide (ITO) since it offers the highest FoM value [11]. However, the global shortage and increasing price of indium has triggered attempts to enhance the properties of more affordable TCOs, especially Aluminum-doped ZnO (AZO) [13,14]. On an industrial scale, the deposition of AZO and other TCO films is usually performed through expensive vacuum-based technologies such as sputtering to obtain high-quality films. Another approach is using wet deposition techniques such as sol-gel method which provide a considerably more affordable way without the necessity of applying high temperature or vacuum condition [2]. They are also quite suitable for samples with sizable or non-flat surfaces like tubes [14]. In spite of such advantages, the sol-gel derived films are often porous and of lower quality and less FoM values than those of sputtered films [15], which necessitates further investigation to improve the sol-gel procedure. To date, the solution-based methods have been considered highly promising in inkjet printing of TCOs for low-cost printed electronics and solar cells [16].

In the sol-gel synthesis of thin films, nanocrystalline or amorphous as-deposited layers transform into the crystalline state by the post-deposition crystallization, throughout which the crystal orientation and grain-boundary characteristics develop. These microstructural features affect the optical and electrical properties and hence, the FoM value. Accordingly, controlling the film crystallization is a crucial step in the sol-gel synthesis of TCOs. Based on the barrier model theory proposed by Seto on the electrical properties of polycrystalline silicon films [17], and its expansion to AZO structures [18], Ohyama [19] and Nishio [20] concluded that AZO shows higher conductivity in the case of having a highly-oriented microstructure toward the c-axis of the zincite structure, compared with less-oriented or granular microstructures. Considering that the conductivity σ is in a direct relationship with the concentration N and mobility μ of charge carriers as $\sigma \sim \mathrm{N}.\mu$, a higher concentration results in less optical transmission, while the effect of the mobility value on transmission is insignificant [21]. Accordingly, a highly-oriented microstructure shows higher

conductivity because the mobility of charge carriers is enhanced by grain-boundary scattering being less effective. Higher conductivity is thus obtained while the optical transmission is unaffected, which means a higher FoM value. Heretofore, many attempts have been devoted to improve the performance of the sol-gel derived AZO thin films through studying how microstructural features are influenced by processing parameters, including solvent and stabilizer types [22-26], precursor and doping concentrations [23,20,27], deposition conditions [20,26], the drying temperature [20,28, 29] and finally annealing cycles and atmosphere [20,30,31].
In this chapter, a recently proposed modification to improve the films' conductivity value is studied. Accordingly [22], by adding water to the coating sol, the subsequent change in the hydrolysis reaction leads to a decrease in the resistivity of the final AZO thin film. Here we attempt to clarify the reasons for such an observation. The results contribute to enhance the sol–gel deposition of AZO thin films through obtaining higher FoM values, and therefore, superior performance in any photoelectrochemical cell including DSSC.

5.2 Materials and Methods

5.2.1 Sol Preparation

Figure 5.1 shows the sol preparation steps. Zinc acetate dihydrate (ZAD), $Zn(CH_3COO)_2.2(H_2O)$, was first dissolved at room temperature in a round-bottom twin-neck flask containing 2-methoxyethanol (2-Me) as the solvent and monoethanolamine (MEA) as the stabilizer agent. The concentration of ZAD was 0.2 $mol.L^{-1}$ and the molar ratio of MEA to ZAD was [MEA/ZAD] = 2. Then it was heated under reflux for 1 hour at 70 °C to yield a clear and homogeneous solution. A part of the obtained solution was removed and transferred into another flask and kept under stirring at room temperature to serve as the ZnO sol henceforth. For the remaining part, the doping solution which was ethanolic solution of aluminum nitrate nonahydrate, $Al(NO_3)_3.9H_2O$, was added drop by drop. The molar ratio of the dopant, $[Al^{3+}/Zn^{2+}]$, was precisely selected 2%. Then it was left under reflux for a further 1 hour at 70 °C to get a clear and quite pale yellowish solution. A part of the newly obtained solution was removed once again and transferred into another flask and kept under stirring at room temperature to serve as the pure AZO sol thereafter. The third part of the solution was modified via altering the hydrolysis reaction, through adding drop by drop a precise amount of ultrapure distilled water. The molar ratio of additional water to ZAD was $[H_2O/ZAD] = 2$. Then it was left under reflux for a further 1 hour at 70 °C, whereby a slightly stronger yellowish solution was obtained. It was kept under stirring at room temperature to serve as the modified AZO sol in future. All 3 flasks were dynamically aged for 72 h to yield a proper viscosity and a suitable colloidal condition. A pH measurement was performed for the sols afterwards.

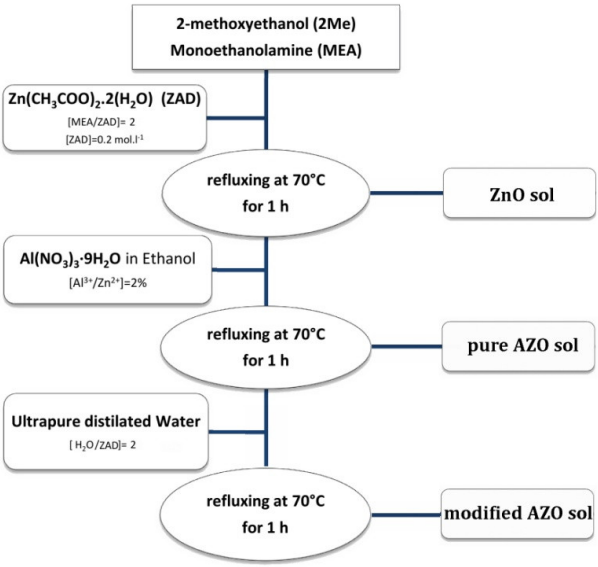

Figure 5.1. *The flowchart summarizing the sols preparation steps.*

5.2.2 Gel and Powder Processing

The remaining part of the main flask was used to prepare AZO gel and powder. The gel was obtained by keeping a portion of the solution in 80 °C for almost two weeks insofar as that a bright brownish sticky soft substance was obtained. The remaining sol was kept under reflux at 70 °C for 24 hours; whereby white AZO powder precipitated. The powder was collected after three times washing by ethanol and centrifuging, followed by annealing at 600 °C for 2 hours.

5.2.3 Substrates Preparation

The specimens were produced in 2 different groups, the Group A over soda-lime and the Group B over silica substrates, all with the dimension of 2.5×3.8 cm^2. The substrates preparation started by washing them by soap and 5 minutes of ultrasonic cleaning in acetone, ethanol and distilled water respectively. Next, in order to have highly hydrophilic surfaces with outstanding wettability, a ternary treating procedure performed, which was 10 minutes rinsing in piranha solution, then in a 5% solution of ammonium hydroxide and finally in a 5% solution of hydrochloric acid, followed by rinsing in distilled water and drying with compressed nitrogen blow.

5.2.4 Film Deposition and Annealing

A home-made dip coating apparatus was used for the film deposition. All depositions were performed under identical condition with a withdrawal speed of 2.5 cm·min^{-1}. The dipping chamber was kept at room temperature and filled with N_2 to have a dry atmosphere during the depositions and the subsequent drying. Before dipping the substrates, the coating sols were filtered through Millipore Millex-FG hydrophobic Teflon filters of 0.2 µm. Then they were warmed up to roughly 40 °C in order to insure having a homogeneous viscosity, better substrates coverage and in particular, an enhanced solvent evaporation after the withdrawal. The latter improves the layer thickness uniformity and therefore, avoids formation of pale whitish haze-looking zones on the coated areas [30]. After the withdrawal, samples were kept for 2 minutes in the dry atmosphere of the dipping chamber to start the drying and gelation reaction. It was followed by a 5 minute intermediate heat-treatment through introducing the Group A and Group B samples to an electrical furnace heated up to 275 °C and 430 °C respectively. The layer deposition cycle was repeated 15 times for each sample to obtain an adequate thickness. At the end, the final heat-treatment was performed in static air for 1 hour at 500 °C and 600 °C for Group A and Group B respectively. An additional heat-treatment was also performed only for Group B samples in Ar flow at 600 °C for 1 hour followed by another 1 hour at 400 °C in Ar/H_2 flow containing 3% hydrogen. The thermal treatment details and thermal history of samples is summarized in Table 5.1.

Table 5.1. *The thermal treatment details and thermal history of samples.*

Samples	Intermediate heat-treatment	Final heat-treatment	Additional heat-treatment		
Group A	static air at 275 °C for 5 minute	static air at 500 °C for 1 hour	none		
Group B	static air at 430 °C for 5 minute	static air at 600 °C for 1 hour	Ar flow at 600 °C for 1 hour	Ar/H_2 flow at 400°C for 1 hour	cooled down to RT* in Ar/H_2 flow

*room temperature

5.2.5 Characterization

DTA-TG measurements were performed on a Netzsch STA-409 instrument (NETZSCH Group, Selb, Germany), in the range of 20–700 ◦C with a heating rate of 10 ◦C·min-1, in static air; alumina crucibles for both reference and sample were used. Baseline correction for the DTA curve and buoyancy correction for TG were

carried out by means of an empty crucibles experiment. FT-IR analysis was performed with a Nicolet Avatar 330 instrument, in transmittance mode; powdered gel was dissolved in KBr in order to get a pellet. The same instrument was further utilized to measure the IR transmittance of the deposited thin films as well. The usual adopted scan conditions were: 4000–400 cm-1 as the wavenumber range, and the number of scans was equal to 64 with a resolution of 4 cm-1. XRD spectra were acquired on a Rigaku DMax-III D diffractometer (Rigaku Corporation, Tokyo, Japan), employing a CuKα radiation (λ = 0.154056 nm) and a graphite monochromator in the diffracted beam. Asymmetric scattering configuration was adopted for film measurements, with typical parameter values: scan range in 2θ: 10◦ to 50◦; counting time: 10 s; sample interval: 0.1◦; and the incidence angle set at 1◦. For the evaluation of crystallite dimensions, line profile analysis on the fitted peaks was performed with MAUD software [24]. To measure the sheet resistance of the obtained films in square geometry, the four-point probe method was applied at room temperature. The films' thicknesses were determined through spectroscopic ellipsometry by a HORIBA-UVISEL ellipsometer (HORIBA Ltd., Kyoto, Japan) equipped with DeltaPsi2 software. Finally, the normal transmittance and near-normal reflectance spectra were obtained by a UV-Vis-NIR spectrophotometer JASCO V570 (JASCO International Co. Ltd., Tokyo, Japan) at room temperature in the range of 300–2500 nm with the resolution of 2 nm.

5.3 Results

Figure 5.2 shows TG-DTA and derivative curves of the dried AZO gel heated in static air with the rate of 10 °C.min^{-1}. It indicates that the weight loss occurs in two different steps. The first one is observed as a sharp drop down to nearly 55% in the range of 195 to 275 °C, corresponding to the endothermic peak centered at 250 °C. During the other step, a mild weight loss starts at around 275 °C and continuous in a long temperature range up to 590 °C, comprising about other 15% weight loss. In the DTA graph, it associates with a long-range exothermic pattern resulting from successive exothermic reactions overlap, from which the sharp ones centered at around 300 and 485 °C are identified. No other weight loss is observed after 600 °C.

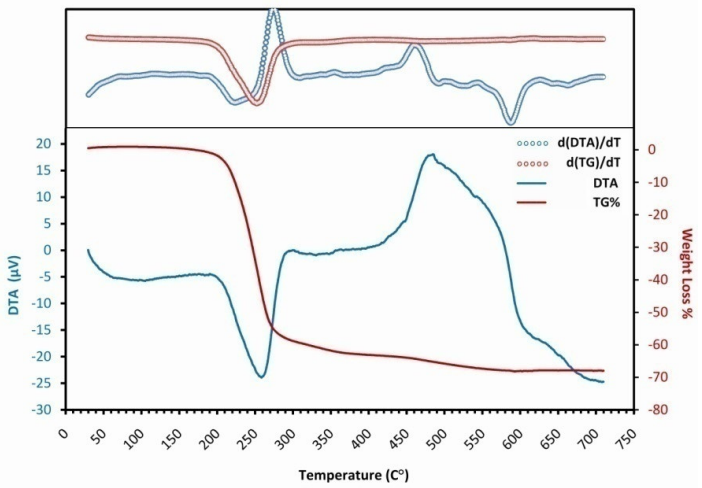

***Figure 5.2**. The TG-DTA graph of the dried gel. The derivatives are plotted in upper part.*

Figure 5.3 illustrates IR spectra of the dried AZO gel and its thermal evolution at 275 °C, 430 °C and 600 °C, in addition to ZAD, MEA and 2-ME data as the initial compounds. Higher magnifications of the graph are also included from the spectral range of 400-700 cm^{-1}, 1200-1800 cm^{-1} and 2500-3200 cm^{-1} corresponding to the IR spectrum range of Zn-O, carboxyl COO and amine CH_2 bonds respectively.

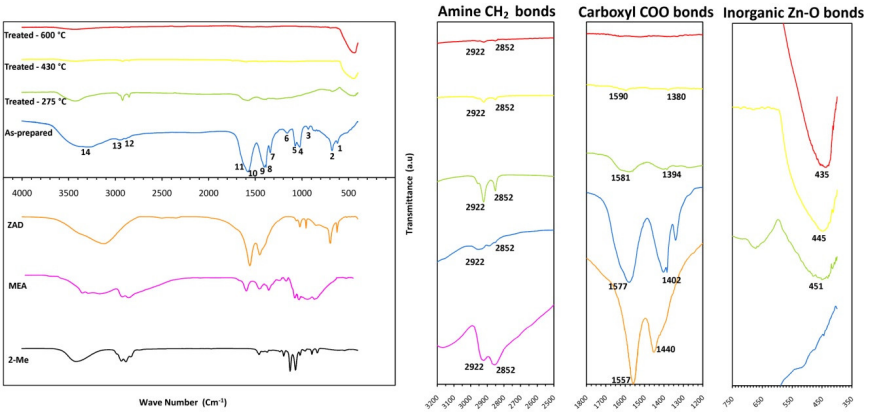

***Figure 5.3**. The IR spectra of the as-prepared AZO gel and its thermal evolution at 275°C, 430°C and 600 °C (Upper left), in addition to the data of initial compounds, ZAD, MEA and 2-ME (Lower left). Magnified parts of the spectra regarding CH2 bond, COO bond and Zn-O bond (Right). The initial compounds data were taken from Bio-Rad's IR spectral databases.*

For the dried gel, a superposition of ZAD and MEA peaks is observed, mainly including CH_3, COO and OH absorption peaks of ZAD in the range of 1000-1100 cm^{-1}, 1400-1600 cm^{-1} and 3200-3400 cm^{-1} respectively; as well as CH_2 deformations and CH_2 stretching peaks of MEA in the range of 1300-1500 cm^{-1} and 2800-3000 cm^{-1} respectively. The 2-Me peaks must be overlapped by other peaks since the long-term evaporation allows just a little amount of 2-Me remains in the sticky gel. Distinct absorption peaks of the as-prepared gel are numbered as 1 to 14 under the spectrum and their wavenumbers as well as brief explanations regarding the bonds and vibration modes of the constituent peaks are listed in Table 5.2.

Table 5.2. *Wavenumbers of distinct absorption peaks in the IR spectrum of as-prepared gel, numbered as 1 to 14 in Figure 5.3. The molecular bonds and vibration modes of the constituent peaks are provided*.

Peak(cm^{-1})		Assignments	Peak(cm^{-1})		Assignments
1	**622**	π (COO) ⟶ ZAD	9	**1402***	symmetric stretching (COO) ⟶ ZAD
2	**696**	α (COO) ⟶ ZAD	10	**1577**	asymmetric stretching (COO) ⟶ ZAD
3	**941**	out-of-plane deformation (NH_2) ⟶ MEA	11	**1593***	in-plane deformation (NH_2) ⟶ MEA
4	**1024***	rocking (CH_3) ⟶ ZAD stretching (CO) ⟶ MEA	12	**2852**	symmetric stretching (CH_2) ⟶ MEA
5	**1072***	rocking (CH_3) ⟶ ZAD stretching (CN) ⟶ MEA	13	**2922**	asymmetric stretching (CH_2) ⟶ MEA
6	**1150**	stretching (COH) ⟶ MEA			
7	**1342**	symmetric bending (CH_3) ⟶ MEA			
8	**1384**	symmetric bending (CH_2) ⟶ ZAD			

* Overlap of two or more peaks

While no evidence is detected for Zn-O bond in the gel, after heat-treatment at 275 °C, together with a considerable reduction of all organic bonds, an absorption peak of metal oxide bond appears at around 451 cm^{-1}. It is related to the stretching vibration of Zn-O bond in tetrahedral coordination [32]; whereas we cannot clearly conclude about the presence of Zn-O bond in octahedral coordination that shows absorption peak at around 670 cm^{-1} [32], due to overlapping with α and π bonds of COO peaks of ZAD. The trend continues for the treated gels at 430 and 600 °C with increasing the peak intensity of Zn-O bond in tetrahedral coordination and diminishing of remaining organic bonds, while the formation of Zn-O bond in octahedral coordination seems to be totally insignificant. In the spectra of treated gel at 600 °C just a sharp Zn-O bond peak is detected with a minor trace of CH_2 and OH bonds.

In Figure 5.4, the XRD patterns concerning the samples of both groups after the final heat-treatment are displayed in addition to the spectrum of the calcined powder. By performing the curve fitting on the peaks through the MAUD software, the thin films microstructural parameters, shown in the Table 5.3, were evaluated. The texture coefficient of (002) peak, $T_c(002)$, was also calculated for each sample, using the equation (3), in order to quantify the structural mono-orientation toward this plane;

$$T_c(002) = \frac{\left[I(002)/I_p(002)\right]}{\frac{1}{n}\cdot\sum\left[I(hkl)/I_p(hkl)\right]}, \quad (5.3)$$

where $I(hkl)/I_p(hkl)$ denotes the ratio of (hkl) peak intensity in the textured sample to the one in the randomly oriented pattern (powder); n is the number of considered reflections; and $\Sigma[I(hkl)/I_p(hkl)]$ indicates the summation of ratios for all n reflections [33]. The texture coefficient of planes in the powder pattern is $T_c(hkl)=1$; and any deviation in thin films patterns as $T_c(hkl) > 1$ or $T_c(hkl) < 1$ implies a preferred growth, as abundance or scarcity of grains oriented in the related direction respectively [34]. Moreover, the relative intensity of (002) peak, $I_r(002)$, was calculated as the ratio of the (002) peak intensity to the summation of all reflections intensities [35].

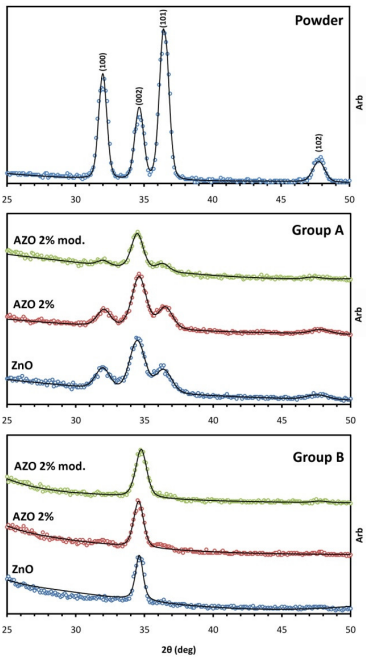

***Figure 5.4**. X-ray diffraction patterns for the powder particles and Group A and B samples after the final heat-treatment.*

***Table 5.3**. The results of line profile analysis on of the fitted peaks of thin films in Figure 5.4.*

Samples	Crystallite Size (nm)	c-axis Microstrain (%)	Texture	
			$T_c(002)$	$I_r(002)$
ZnO	27±2	-0.12	2.25	0.56
AZO2%	20±1	-0.29	2.34	0.58
AZO2% mod.	22±2	-0.23	2.94	0.73
ZnO	29±2	-0.11	3.92	0.98
AZO2%	24±1	-0.25	3.84	0.95
AZO2% mod.	27±1	-0.19	3.98	0.99

For the evaluation of electrical properties, 4-point probe test was performed on samples after the final and additional heat-treatments. The results in the form of sheet resistance, R_{sh}, and resistivity, ρ, are reported in Table 5.4. R_{sh} values, averaged on four different measurements, were estimated using the Equation (5.4) as

$$R_{sh} = \left(\frac{\pi}{\ln 2}\right)\frac{\Delta V}{I}, \tag{5.4}$$

in which ΔV is the potential difference between the voltage probes while the constant current flow of I is induced to the sample via the current probes. The ratio is multiplied by correction factor for thin films [36]. Then, ρ values were obtained by multiplying R_{sh} to the film thickness value which was determined as d = 106±2 nm. The degree of uncertainty is difficult to quantify, but the deviation was considered mainly due to systematic errors resulting from probes surface area and their non-ohmic contacts, which affects the relative behavior of different films in a similar way [37].

***Table 5.4**. The results of 4-point probe test on sheet resistance and resistivity values.*

Samples		After final heat-treatment		After additional heat-treatment	
		R_{sh} (Ω/sq)	ρ (Ω.cm)	R_{sh} (Ω/sq)	ρ (Ω.cm)
Group A	ZnO	10^6 <	10 <		
	AZO2%	348.6×10^3	3.7±0.3		
	AZO2% mod.	294.4×10^3	3.2±0.1		
Group B	ZnO	10^6 <	10 <	298.5×10^3	3.1±0.2
	AZO2%	49.7×10^3	0.52±0.2	1.3×10^3	$(14.5\pm0.3)\times10^{-3}$
	AZO2% mod.	38.4×10^3	0.41±0.1	543.7	$(5.9\pm0.1)\times10^{-3}$

The optical transmittance T and reflectance R spectra of Group B samples after the additional heat-treatment are compared in Figure 5.5. An extended spectrum in IR range is included for the transmittance as well. Since the measured values of T and

R are affected by the substrate, following equations were used to estimate the films absolute values, supposing that the substrate is homogenous and transparent with negligible absorption [38]:

$$\begin{cases} T = \dfrac{1 + R_0 - 2\Phi_R(R_0)^2}{(1 + R_0)^2 - (R_0.\Phi_T)^2}.\Phi_T \\ \\ R = \dfrac{2(1 + R_0)\Phi_R - (\Phi_T)^2}{(1 + R_0)^2 - (R_0.\Phi_T)^2}.R_0 \end{cases} ; \quad (5.5)$$

in which R_0 is defined by the refractive index of substrate, ns, as $R_0 = \frac{(1-n_s)^2}{(1+n_s)^2}$, and $\Phi_R = \frac{R_{meas}}{R_s}$ and $\Phi_T = \frac{T_{meas}}{T_s}$ represent the ratio of the measured reflectance and transmittance of the sample to the ones of the bare substrate respectively. Having the absolute values of T and R, the absorptance A is obtained as $A\% = 100 - T\% - R\%$. Average values of spectrophotometry measurement within the visible range from 400 to 700 nm are reported for all samples in Table 5.5 as $\overline{T}\%$, $\overline{R}\%$ and $\overline{A}\%$.

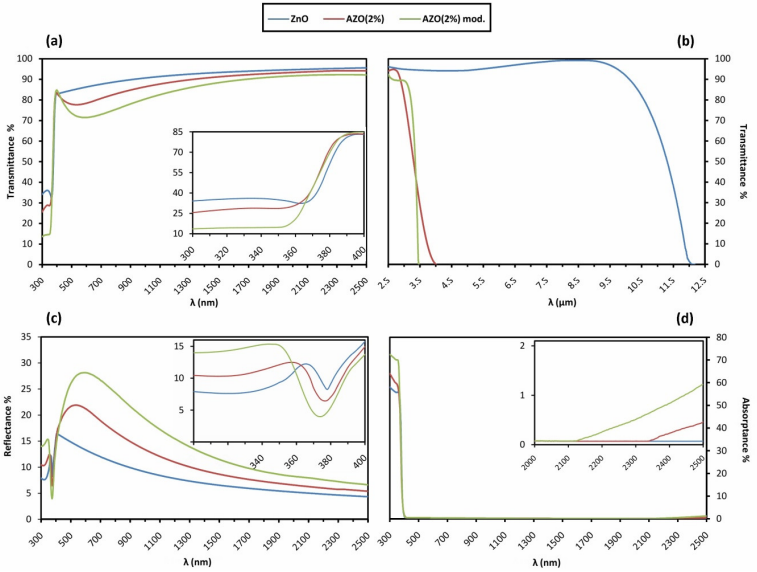

Figure 5.5. *UV-Vis-NIR spectra of Group B samples; (a) transmittance (b) extended transmittance (c) reflectance and (d) absorptance. Inset graphs for (a) and (b) show the magnification around the absorption edge while for the absorptance spectra the inset is the magnification of the far right range*.

The absorption coefficient α as a function of T and R values and the film thickness d is given by the following equation which takes into account the multiple internal reflections [39]:

$$\alpha = \frac{1}{d}\ln\left[\frac{(1-R^2)}{2T} + \sqrt{\frac{1-R}{4T^2} + R^2}\right]. \quad (5.6)$$

Having α, the optical band-gap energy E_g was estimated from the conventional Tauc-plot method. According to Tauc empirical rule [40], for the incident photons with energy levels higher than E_g which are identified by the fundamental absorption; α is a function of photon energy E = h.v with the below equation for the direct transition occurring in ZnO band structure:

$$\alpha.h\nu \sim \left(h\nu - E_g\right)^{0.5}; \quad (5.7)$$

so the extrapolation of the linear part of $(\alpha.h\nu)^2$ versus hv gives the approximate E_g value at the hv axis; as illustrated in Figure 5.6(b). However, this equation assumes an ideal parabolic band structure and it is reported that in case of broadening of the fundamental absorption edge as a result of doping or structural non-uniformities, Tauc-plot method may underestimate E_g [43,45]. Therefore, a corrected value of E_g was determined by an alternative method using the maximum of the first derivative of absorption coefficient as the function of photon energy, dα/d(hv) [44-46], as shown by dotted lines in Figure 5.6(c). All curves follow the Gaussian trend depicted with solid fitting lines. The difference between the obtained values for the band-gap energy ΔE_g is associated with the degree of absorption edge broadening and is shown to be related to the damping energy Γ by $\Delta E_g = (\pi/4)\Gamma$ [40]. The E_g values calculated by both methods in addition to Γ values are reported in Table 5.5.

For the incident photons with the energy just below the band-gap energy, α shows another form of dependency on hv as stated by Urbach empirical rule [44]:

$$\alpha \sim \exp\left(h\nu / E_u\right); \quad (5.8)$$

in which E_u is the Urbach energy, corresponding to the width of the absorption edge below the band-gap [45]. By plotting Ln(α) versus hv, the value of E_u is calculated by taking the reciprocal of the slope of the linear part in the lower photon energy region of the curve, as depicted in the inset of Figure 5.7(b). The obtained values of E_u are reported in Table 5.5.

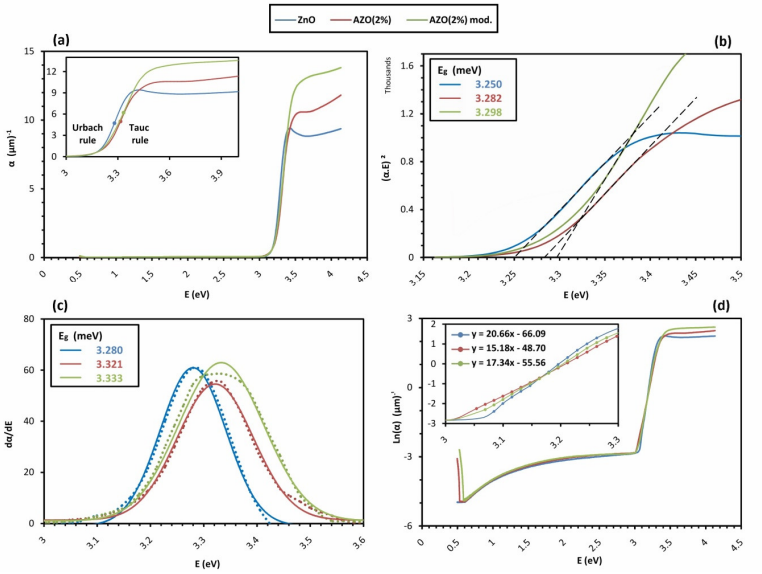

Figure 5.6. *(a) The plot of α (μm-1) versus hv. The inset is the magnification of the high energy part and shows the regions governed by Tauc and Urbach rules. The band-gap energies are marked with solid dots. (b) Determination of the band-gap energies via the Tauc-plot method; and (c) the alternative method to find the band-gap using the maximum of the dα/d(hv) curve (dotted curves). The solid curves show the Gaussian fits for dα/d(hv) curves. (d) The plot of Ln(α) (μm-1) versus hv. The inset shows the magnification of the linear parts. The slopes indicate E_u values reciprocally.*

Finally, the optical parameters were calculated including the refraction function as $\bar{n} = n + i\kappa$ and the relative permittivity function as $\bar{\varepsilon} = \varepsilon + i\acute{\varepsilon}$; where the absorption index κ, refractive index n, and real and imaginary parts of relative permittivity, ε and $\acute{\varepsilon}$ were obtained via the relations below:

$$\begin{cases} \kappa = \alpha\lambda/4\pi & R = \dfrac{(n-1)^2 + \kappa^2}{(n+1)^2 + \kappa^2} \\ \varepsilon = n^2 - \kappa^2 & \acute{\varepsilon} = 2n\kappa \end{cases} . \qquad (5.9)$$

Then, n values as a function of λ was fitted to Cauchy dispersion formula [46]. The result is illustrated in Figure 5.7. The n values at λ = 450 nm were used to estimate the porosity p of films through Lorentz–Lorentz equation [50-52]:

$$p = 1 - \frac{(n^2 - 1)/(n^2 + 2)}{(n_B^2 - 1)/(n_B^2 + 2)} \; ; \qquad (5.10)$$

considering that n and n_B are refractive index values of the film and of the pure ZnO bulk respectively. The estimated values for n and p% are listed in Table 5.5.

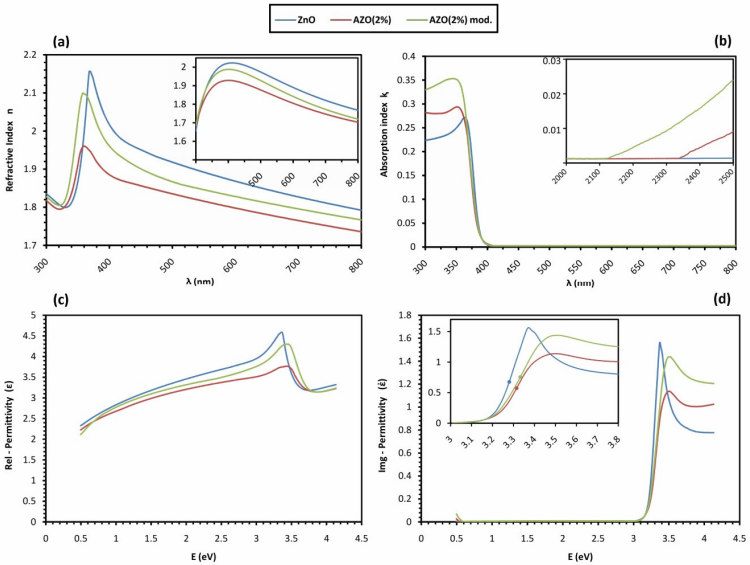

***Figure 5.7**. Calculated optical parameters of the films; (a) and (b) are the refractive index n and the absorption index ƙ as functions of wavelength respectively. The inset shows n values fitted to Cauchy dispersion formula. (c) and (d) are the real part and imaginary part of relative permittivity, ε and ε̇, as functions of photon energy respectively. The inset shows the magnified part of ε̇ around the absorption edge and the band-gap energies are marked out with solid dots.*

***Table 5.5**. A summary of observed values for the optical properties of Group B samples after the additional heat-treatment.*

Samples	Spectrophotometry			Band-Gap Eg (eV)		Urbach Energy Eu (meV)	Damping Energy Γ (meV)	Refractive Index* n	Porosity** p(%)
	$\overline{T}(\%)$	$\overline{R}(\%)$	$\overline{A}(\%)$	Tauc-plot	dα/d(hv)				
ZnO	87.7	11.8	0.4	3.25	3.28	48.4	38	2.01	6.4
AZO2%	82.3	17.1	0.5	3.28	3.32	65.8	49	1.96	16.2
AZO2% mod.	79.1	20.3	0.5	3.29	3.33	57.6	44	1.92	13.5

**at λ = 450 nm from the fitted graph.*
***considering $n_B = 2.12$ [49].*

By the data reported in Tables 5.4 and 5.5 about R_{sh} and $\overline{T}$ values and using the Equations (5.1) and (5.2), the FoM values of the Group B samples after the additional heat-treatment films were obtained as displayed in Table 5.6.

***Table 5.6**. Calculated FoM values for Group B samples after the additional heat-treatment through 3 different equations.*

Samples	**Haacke FoM** [4]	**Jain-Kulshreshtha FoM** [3,5]	**Gruner-Coleman FoM** [8,9,11]
ZnO	8.61×10^{-7}	2.46×10^{-5}	9×10^{-3}
AZO2%	1.07×10^{-4}	3.9×10^{-3}	1.41
AZO2% mod.	1.72×10^{-4}	7.7×10^{-3}	2.75

5.4 Discussion

The electrical and optical properties of the obtained films are associated with the preferred crystallization orientation and grain-boundary characteristics of their microstructures [17]. These features are correlated with the both 1) sol chemistry, as it determines the nature and amount of the species in the amorphous deposited layer; and 2) thermal treatment procedure, which induces the nucleation and crystal growth as well as the decomposition and the release of organic molecules. Generally, the oriented crystallization toward the c-axis is energetically-preferred in ZnO thin films over the substrate [23]. Based on the Ohyama proposed explanation [23], the preferred orientation toward the c-axis is even enhanced in case of less overlapping and coincidence of steps of this sequence: (a) evaporation of the liquid phase and decomposition of the organic residue, and (b) crystallization of the oxide film. Since the structural relaxation of the gel, as a prerequisite for the oxide film crystallization, originates from the evaporation of the liquid phase and decomposition of the organic residue, the better separation of steps helps avoiding any deterioration of crystallization uniformity. Such a separation is taken into account by performing the first step during intermediate heat-treatments and postponing the second one to the final heat-treatment. It requires knowing physical and chemical properties of the sol species such as boiling temperature and molecular bonding, in addition to the gel reaction to high temperature. So a detailed study on the sol chemical evolution as well as the thermal evolution of the gel is taken into consideration; followed by the consequent effects of different sol chemistry and thermal treatment procedure on the microstructural features. Finally, the different optoelectrical behavior arises from the modified microstructure is compared with those of others and evaluated by FoM value.

5.4.1 Evolution of the Sol

While the commonly used sol–gel routes to synthesize metal oxides are based on hydrolysis reactions of metal-alkoxides or their inorganic salts in organic solvents or

aqueous media respectively [51], for ZnO-based compounds, using ZAD as an organic salt in an alcoholic solvent has been reported more often, which is an intermediate between the two conventional sol–gel routes. In such conditions, an in-situ formation of alkoxide- or hydroxide-based compounds happens initially and then they transform into metal oxide nanoparticles via hydrolysis and condensation reactions [52].

The experiment in this study starts by adding 2-ME to the ZAD precursor which results in the formation of zinc monoacetate, Zn(OAc) [53], while the expected zinc alkoxide is inhibited to form; since the solubility of simple zinc alkoxides in alcoholic media is restricted to just long-chain alcohols such as oleyl alcohol [57,58]. Then, the supposedly released water molecules of ZAD start to hydrolyze Zn(OAc), forming zinc hydroxide, $Zn(OH)_2$, which will undergo condensation to form ZnO during the forthcoming thermal treatment. However, due to the low initial amount of water supplied by ZAD, the rate of assumed hydrolysis is low [56]. Addition of water in this step is not helpful and should be avoided; as otherwise, since the solubility of $Zn(OH)_2$ in alcohols is limited, white solid $Zn(OH)_2$ precipitates [57]. Moreover, the limited solubility in alcohols applies to ZAD as well; because the coulombic hydration sheath surrounding a zinc cation remains attached with it inside non-polar solvents and prevents the dissolution [57,61]. Consequently, all reactions develop just very partially, resulting in a turbid grayish solution. Eventually, any hydrolysis through the aqueous route is considerably insignificant.

In order to improve the solubility, it is necessary to introduce an additive compound such as monoethanolamine (MEA) that acts as a nucleophilic agent towards Zn ions. MEA has two Lewis base groups, a hydroxy and an amine and it is capable of making a bidentate ligand, whether as a chelate to one ion or a bridge between two Zn ions [59]; however, a chelating ligand is expected to be more stable [63,64]. In a similar way, in ZAD and Zn(OAc), acetate is a Lewis base and a chelating ligand exists between the acetate oxygen atoms and Zn ion; while water molecules form a hydration sheath around the metal core [65,66]. It is reported that by adding amine-containing compounds, the hydration sheath is disturbed and water molecules are released [58]. Moreover, instead of a selective coordination and ligand exchange with the acetate anion, an additional coordination happens [64]. Therefore, the MEA molecule alongside the acetate ion forms a complex ion cooperatively, in which the central metal ion is coordinated by two chelating ligands; a metal-oxygen core formed by the acetate ion, covered by an organic shell made by MEA. The solubility of the new complex compound, referred by [MEA][Zn(OAc)], in the non-polar solvent of 2-ME is much more than before the addition of MEA; so that a clear transparent solution is obtained. However, based on DFT calculations, such a mono-nuclear compound is not thermodynamically stable in the solution and a dimer structure, $[MEA]_2[Zn(OAc)]_2$, has nearly 50 $kcal.mol^{-1}$ free energy less than two monomers [65]. In the solid phase, the most stable compound has a tetramer structure,

$[MEA]_4[Zn(OAc)]_4$, formed by the union of two dimers [66]. Figure 5.8 illustrates the structural formula related to each one.

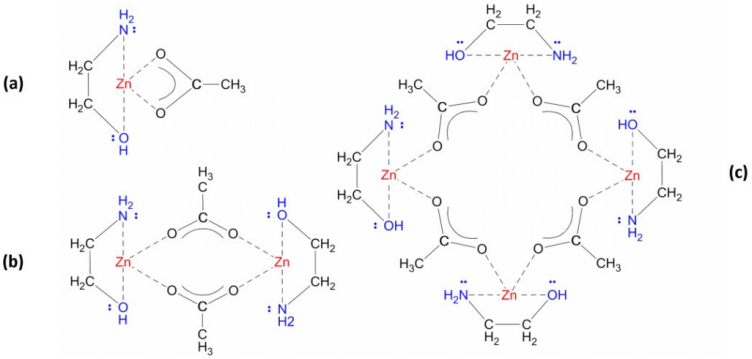

***Figure 5.8**. Proposed structural formula of different forms of the complex compound as a, (a) monomer, (b) dimer and (c) tetramer.*

As depicted in Figure 5.8, in the monomer structure, likewise ZAD, there is a chelating ligand between any acetate and Zn ions; while in dimer and tetramer structures, each acetate anion forms a bridge ligand between two metal ions. Similar result regarding the bonding condition was reported through NMR analysis as well [65].

The subsequent transformation of the sol species depends on the competition for the Zn Lewis acid center between nucleophilic species of $(-NH_2)$ and $(CH_3COO)^-$ as the capping agents, and $(OH)^-$ as the hydrolysis agent [59,70]. Considering a fixed amount for acetate anions, it is possible to modify the sol evolution by changing the molar ratio of the other species in so far as the solution remains clear and in equilibrium condition.

The presence of free $(OH)^-$ primarily originates from the basic environment. Owing to $[H_2O/Zn^{2+}] = 2$ in ZAD, the typical initial condition is $[OH^-/Zn^{2+}] = 1$. However, unlike before the addition of MEA, it is possible to manipulate the ratio by adding a limited amount of extra water, inasmuch as the solution remains clear. The experimented molar ratio of $[H_2O/ZAD] = 2$ for additional water increases the amounts of free $(OH)^-$ to $[OH^-/Zn^{2+}] = 2$. It was observed that the addition of more water makes the solution translucent and disturbs the equilibrium. For $(-NH_2)$, the ratio of $[MEA/Zn^{2+}] = 1$ is extensively used in literature; however, several researchers have reported that in case of $[MEA/Zn^{2+}] = 2$ a more enhanced texture orientation toward c-axis direction of zincite structure [59, 23, 71] and also finer crystallite size with less porosity is obtained [69]. This approach is also confirmed by the investigations exclusively devoted to study the effect of amino-additives amount on the microstructural features of ZnO thin film [24,25,72,73]. While an equimolar ratio

of [MEA/Zn^{2+}] is enough to form the [MEA][Zn(OAc)] spices, a higher ratio increases the solution pH value, which affects the formation of ionic zinc complexes. It is known that the stable ionic form of Zn in the solution varies by changing the pH; from Zn^{2+} in acidic conditions to non-ionic state when 6 < pH < 8, and to Zn^{2-} in highly basic condition of pH > 12 [73]. The latter pH value, which can facilitate formation of a stable hydroxide-based complex ion, was obtained by [MEA/Zn^{2+}] = 2 in the present study.

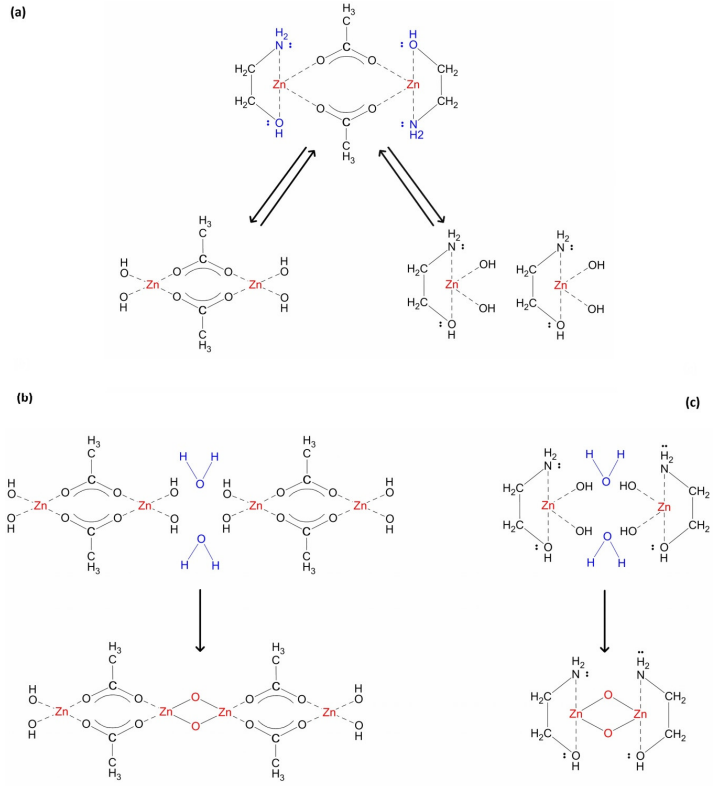

***Figure 5.9**. Suggested mechanism for possible hydrolysis (a); and condensation reactions (b) and (c).*

Considering the condition obtained from the applied ratios of [OH^{-}/Zn^{2+}] and [MEA/Zn^{2+}], following the addition of extra water, the hydrolysis reaction accelerates and continues throughout the reflux time. It originates from attacking the highly nucleophilic $(OH)^{-}$ to the core of the complex, transforming it to a hydroxide-based complex as depicted in Figure 5.9(a).

During the aging time, the hydrolysis products are in equilibrium with the initial complex but they may engage in condensation reaction if water molecules are present, illustrated by Figures 5.9(b) and 5.9(c). It involves linking of the hydrolysis products through formation of metal-oxygen bonds in an oxolation condensation.

5.4.2 Thermal Evolution of Gels

Transformation of the gel layer into the oxide film is a multiple-step process. It involves formation of metastable intermediates, pyrolysis and decomposition of organic parts, initiation and development of a network of metal oxide crystallites by nucleation and growth mechanisms as well as releasing the residuals outwards. The initial part of such a process occurs during the drying and intermediate heat-treatment which is performed between each layer deposition; while the rest happens throughout the final heat-treatment within the whole of the layers collectively. The extent to which the transformation develops during the intermediate heat-treatments is decisive in the crystallization behavior and the microstructure of the final film [72].
In the gel IR spectrum, in spite of overlapping, it is clear that absorption peaks (listed in Table 5.2) follow a simple superposition of MEA and ZAD peaks. As a suitable indication, we can follow the stretching COO peaks of ZAD (the peaks numbered as 9 and 10) and the stretching CH_2 peaks of MEA (those numbered as 12 and 13) due to their higher intensities in the initial compounds and being relatively less influenced by overlapping. It is observed that while CH_2 peaks of MEA appear without any shifting in the IR spectrum of the gel, the two stretching COO peaks of ZAD, referred by $v_{symmetric}$ and $v_{asymmetric}$, show a diverging shift in their wavenumbers. In other words, if the wavenumber separation value is defined as $\Delta v = (v_{asymmetric} - v_{symmetric})$, for stretching COO peaks we have: $\Delta v_{(ZAD)} < \Delta v_{(gel)}$, as it is clear in the magnified part of Figure 5.3 in the carboxyl COO bonds frame. It is reported that Δv value is the characteristic of acetate/metal bonding form and as a general rule: $\Delta v_{(chelating)} < \Delta v_{(bridging\ bidentate)} \leq \Delta v_{(ionic)} < \Delta v_{(unidentate)}$ [66,75,76]. Accordingly, while in the ZAD structure nearly all bonds between acetate groups and Zn ion are chelating ligands, bridging bonds are expected to exist in the gel. It is in accordance with the presence of thermodynamically more stable dimers and tetramers of [MEA][Zn(OAc)] with bridging ligands instead of monomers with chelating ligands.
In the IR spectrum of the treated gel at 275 °C, the most noticeable feature is a drastic decrease in absorption peaks of organic bonds. It shows that the 55% weight loss and the endothermic peak observed in 195-275 °C of TG-DTA graph are related to decomposition of zinc-organic compounds. Comparing with the spectrum of the as-prepared gel, the intensity reduction is more evident for the stretching COO peaks of ZAD than the stretching CH_2 peaks of MEA. (In the gel spectrum, a considerable part of CH_2 peaks is hidden due to overlapping with the broad OH peak of ZAD). So it can point to the fact that compounds containing acetate group experienced more deterioration by 275 °C. Besides, while the Δv value for stretching CH_2 peaks of

MEA remains unchanged, it continues the increasing trend for COO peaks, probably as a result of unidentate bonds formation in decomposed species. The second important feature is the appearance of Zn-O bond absorption peak which indicates the existence of crystalline ZnO with tetrahedral coordination. It means that the exothermic process started at around 250 °C and centered at nearly 300 °C could be associated to the AZO crystallization from newly-decomposed zinc compounds. Eventually, 275 °C was selected as the lower limit for intermediate heat-treatment temperature, since it separates the first sequence of decomposition-crystallization.

At 430 °C, the TG analysis shows 10% weight loss more than that of observed at 275 °C; and it is correlated with the ongoing reduction in the intensity of organic bonds peaks in the IR spectrum. Since the maximum weight loss obtained through TG analysis is around 70%, a great amount of organic compounds are decomposed by 430 °C, including those containing MEA. Furthermore, the relatively sharper Zn-O bond absorption peak indicates a fair development in AZO crystallization during 300-430 °C. However, the DTA graph does not show the features regarding neither an ongoing decomposition nor a crystallization development. Instead, an almost flat line with a subtle positive sloop is observed which may originates from overlapping of two different peaks happening simultaneously in 300-430 °C; an endothermic peak related to decomposition of organic species containing MEA and an exothermic peak associated to AZO crystallization. Following 430 °C, a net exothermic peak shows that the crystallization overcomes the decomposition afterwards. Accordingly, 430 °C was selected as the higher limit for intermediate heat-treatment temperature since it separates the second sequence of decomposition-crystallization.

The IR spectrum of 600 °C shows a very sharp peak of Zn-O bond in tetrahedral coordination in an organic-free background; nevertheless, an extremely weak yet-detectable pair of peaks related to CH_2 bond of MEA is present. This temperature is associated with 70% weight loss in the TG graph which remains constant up to the end of analysis at 700 °C. So for the final heat-treatment temperature, 600 °C is a suitable choice.

5.4.3 Structural Analysis of Films

X-ray diffraction patterns in Figure 5.4 together with the extracted data in Table 5.3 provide a basis for studying correlation of samples microstructure with the sol chemistry and applied thermal treatment through comparing them with the same batch or with the other group samples. Accordingly, different thermal treatment for Group A and B samples seems to have a determining effect on the texture coefficient T_c and relative intensity I_r of (002) peak; however, other parameters including the crystallite size and lattice strain are less affected by the thermal treatment. The only other noticeable variation is observed in comparing AZO structures with the undoped ZnO ones; where altering the sol chemistry by the introduction of Al^{3+} dopants causes smaller crystallite sizes and increased

microstrain values, independently of the applied thermal treatment. This is in accordance with observing slight broadening of (002) peaks in AZO patterns. On the other hand, altering the sol chemistry in terms of sol modification seems to have no effect, although the c-axis microstrain values are fairly affected in the modified AZO ones.

In order to discuss about the samples texture, the powder pattern is considered as the reference. This pattern shows a set of well-defined diffraction peaks concerning a highly crystalline phase in the hexagonal zincite structure with randomly-oriented crystallites. For the films of Group A, apart from a lower degree of crystallinity which originates from the small thickness of the films, a great increment is observed for $T_c(002)$ and $I_f(002)$ values, showing a preferred orientation along c-axis. However, only Group B samples display a totally mono-oriented structure along the c-axis direction; whereas the intensity of other peaks is insignificant. At the same time, through comparing the texture values within the groups, it is observed that different chemistry of the deposited sol does not lead to a significant texture variation. So it can be concluded that the structural orientation in the post-annealed films is essentially the matter of nucleation and grain growth [76], depending on the thermal treatment procedure. Accordingly, the thermal treatment with high temperature approach performed on Group B samples at 430 and 600 °C is recognized more appropriate to decrease the overlapping of decomposition and crystallization and therefore, to obtain a structure with stronger c-axis preferred orientation. This conclusion could associate with the TG-DTA measurement result. As mentioned in Section 5.4.2, the total weight loss of the gel equals to nearly 70%. At 275 and 430 °C, the weight loss is roughly 55% and 65% respectively. Thus, performing the intermediate heat-treatment at 430 °C compared with 275 °C remains fewer amounts of organic residual to be decomposed during the final heat-treatment in which, the grain crystallization and growth occur. Consequently, due to less overlapping of crystallization and decomposition, the morphological order of grains follows the energetically-preferred columnar orientation during the nucleation and growth [23] and it is not disturbed with the release of organic residuals. In the nucleation step, the driving force is the reduction of free energy through transformation of the metastable amorphous phase to the crystalline state; so the initial orientation of nuclei develops in a way to bring about the minimum free energy configuration. Considering a heterogeneous nucleation at the film/substrate or film/film interface, since the basal plane in ZnO structure has a lower surface energy [77], the nuclei with their basal plane parallel to the substrate surface possess the smallest free energy. It can be considered as the origin of preferred orientation along the c-axis [76] that is maintained during the crystal growth as well. In the hexagonal structure of ZnO, the two basal planes are composed of just O^{2-} or just Zn^{2+} ions and therefore, due to being polar and metastable, they show a greater reactivity tendency to impose less energy to the system, which results in a faster growth rate. On the

contrary, the lateral planes are non-polar and electrically neutral with a higher stability. Supposing a full coverage of the substrate, in the initially formed particles the c axis-oriented growth perpendicular to the substrate dominates, due to the faster development of the polar planes [56] and a dense columnar morphology is resulted. However, this reasoning is justified when the nucleation occurs mainly at the film/substrate or film/film interface in a heterogeneous manner. If the deposited layer thickness is larger than the average crystallite size, in addition to the heterogeneous nucleation at the interface, the homogeneous nucleation also occurs inside the film volume, resulting in a porous granular morphology [79,80]. In this study, the obtained final thickness after deposition of 15 layers is in the range of 106 ± 2 nm, indicating that the thickness of each individual layer could be estimated to be less than 10 nm. Since this value is considerably smaller than the average grain size of 20 to 30 nm reported in Table 5.3, a fully-heterogeneous nucleation is claimed in deposition of all layers for the samples of both groups. Therefore, the difference observed in Group A and B samples regarding the $T_c(002)$ and $I_r(002)$ values could be considered as the consequence of the overlapping of decomposition and crystallization.

Regarding the c-axis microstrain values, it is observed that the modified AZO structures in both groups show slightly higher values in comparison with pure AZO ones, considering that the negative sign just indicates the compressive stress mode. Originally, the film stress comprises two components; an intrinsic part due to point-defects and crystal lattice distortions; and an extrinsic part due to the thermal strain related to the different thermal expansion coefficients for the film and the substrate [80]. The latter seems to be insignificant in the c-axis direction; since by assuming the validity of the thin film approximation in having much larger lateral dimensions than that of the thickness, the thermal strain of the film is under a plane stress condition [81]. The intrinsic part mainly results from the substitution of Zn^{2+} by the smaller Al^{3+} ion and/or the presence of oxygen ion vacancies and therefore, it leads to the unit cell contraction and observing compressive strain. For the undoped ZnO samples, the absence of the dopants could lead to lower unit cell contraction and less compressive strain. For AZO samples, the subtle difference in strain values is likely to be caused just by the growth process itself, since the doping levels are identical. Accordingly, the fairly lower strain levels observed for the modified AZO structures could imply slightly enhanced crystallinity of their structures after the growth process, originating from less crystal lattice distortion and fewer numbers of defects such as grain-boundaries and porosities [24].

4.4.4 Electrical Behavior of Films

Preliminary, the electrical performance of the TCO film directly depends on the concentration N and mobility μ of the charge carriers, which are in turn altered by the microstructural variations. This is confirmed by the result displayed in Table 5.4

about the electrical resistivity of the samples. Accordingly, after the final heat-treatment, resistivity values are around one order of magnitude smaller in AZO films of Group B compared with those of Group A ones; indicating that improved electrical conductivities are obtained through performing the high temperature approach of thermal treatment by which, structures with stronger c-axis oriented and greater $T_c(002)$ and $I_r(002)$ values are resulted. Besides, in both groups, fairly lower resistivity values are detected for the modified AZO films. However, the resistivity of undoped ZnO sample is not altered by the microstructural improvements.

These correlations could be associated to the polycrystalline nature of the films and the contribution of grain-boundaries in the charge carrier transport in terms of degrading the mobility of electrons and therefore, the conductivity of the films. Generally, the charge carrier transport in doped semiconductors is limited through three independent scattering mechanisms [82,83]; (1) the scattering by the host-lattice vibration; (2) the ionized scattering due to the distortion resulting from the presence of intrinsic and extrinsic carriers; and (3) the scattering caused by surface-defects. Higher values of mobility are expected for the undoped ZnO samples since the ionized scattering is less-frequent; unlike the AZO samples in which due to the huge numbers of carriers added through Al doping, the charge transport is accompanied by ionized scattering and therefore, lower mobility values are expected. Among the AZO samples, considering the impeding effect of the host-lattice scattering being little at room temperature [18,83], and an identical ionized scattering due to the equal level of doping, the surface-defect scattering is the only reason for the difference observed in conductivity values. The surface-defect scattering is mainly caused by grain-boundaries and their effect on the electrical conductivity was explained by Seto [17] through defining the barrier model. Accordingly, the crystallographically disturbed surfaces between the grains contain a high density of defects and impose a surface-defect energy E_s to the structure as a direct function of the density and the surface energy of grain-boundaries. With respect to the electronic states, E_s is interpreted as localized electronic states within the band-gap with a density value correlated to the defects density. Since in n-type semiconductors the Fermi level is above the localized states [18,84], the localized states related to grain-boundaries are acceptors for the adjacent grains and trap charge carriers from the bulk of the grains. It leads to form (1) charged boundary surfaces; and also (2) the so-called charge “depletion-region” in the bulk of the grains near the boundaries and along them. The charged boundaries establish a potential barrier which impedes the charge transport across the grain-boundaries and also inside the bulk along the depletion-regions [82,83]. Consequently, the non-affected volume for high-mobility charge transport is expected to be larger for a microstructure with larger grains and narrower depletion-region [85].

This explanation justifies the increase in conductivity values of AZO samples in Group B compared with the Group A ones after the final heat-treatment. Since

among the structures with relatively equal crystallite size, a mono-oriented structure contains less density of grain-boundaries, the higher (002) texture coefficients could bring about less restriction for charge transport by forming narrower depletion-regions and therefore, higher values of carrier mobility in Group B AZO samples. Moreover, in modified AZO films, the comparatively higher conductivity could be associated to moderately larger crystallite sizes and less microstrain values. For undoped ZnO samples however, the absence of adequate charge carrier concentration is the predominant reason of high resistivity, making the grain-boundary effect by far insignificant.

Another point concluded from Table 5.4 is the significant effect of thermal treatment atmosphere observed as the result of additional heat-treatment. Accordingly, the resistivity values of Group B samples decreases by nearly two orders of magnitude, even for the undoped ZnO one, which implies a noticeable change in the electronic band structure beyond the microstructural variations.

Together with extrinsic carriers imported to the ZnO lattice by Al^{3+} dopants, another part of carrier concentration is intrinsically supplied by the lattice point defects including oxygen vacancies V_O and interstitial zinc ions Zn_i [86]. While V_O and Zn_i act as donor states and are considered as the origin of n-type conductivity in undoped ZnO; the zinc ion vacancies V_{Zn} and the interstitial oxygen ions O_i act as acceptor states against the intrinsic conductivity. V_O is the by far most abundant point defect due to its much lower formation energy [87,88]; however, performing the final heat-treatment in air atmosphere promotes the chemisorption of acceptor oxygen molecules on the film surface, inside the pores and between the grain-boundaries. Similar to O_i, the oxygen chemisorption involves capturing electrons from the ZnO bulk located in the conduction band and formation of O^{-2} and O^{-} ions leading to the carrier concentration loss. Moreover, it helps charge depletion regions in the bulk which degrades the mobility of carriers as mentioned above [89]. Hence, the low partial pressure of oxygen during the additional heat-treatment could enhance both the concentration and mobility of carriers by giving rise to better desorption of oxygen from the structure [90,91]. By partial introducing of H_2 to the furnace, the additional heat-treatment continues under reducing atmosphere. It is reported that [92] hydrogen-treatment increases the ZnO intrinsic conductivity through accelerating the oxygen desorption and also by etching of small grains growing among larger ones, leading to reduced grain-boundary scattering. More importantly, hydrogen behaves as a shallow donor in the electronic band structure of ZnO [93], leading to charge carrier increase as well. These explanations justify the functionality of the low oxygen pressure and also the role of hydrogen-treatment in decreasing the intrinsic resistivity of the undoped ZnO sample of Group B by performing the additional heat-treatment.

For AZO samples, the effectiveness of the additional heat-treatment is beyond the advantages mentioned for the undoped ZnO sample and expanded to alter the

condition of extrinsic carriers as well, regarding the position of Al^{3+} ions in the ZnO lattice. In the hexagonal structure of ZnO, the O^{-2} and Zn^{2+} ions occupy the tetrahedral positions while all of the octahedral holes are empty, providing suitable space for interstitial Al^{3+}. But ideally and in order to add a free electron to the lattice, one Al^{3+} must substitute for one Zn^{2+} at a tetrahedral position, since in case of interstitial occupation of octahedral sites, it behaves as an acceptor and decreases the conductivity [94]. In an inclusive investigation through performing ^{27}Al NMR spectrometry on AZO powders [95], Damm et al. reported that while before the reductive annealing, the relative occupancy of Al^{3+} in octahedral positions is more or less equal to the tetrahedral ones, after the reduction annealing a dominant substitutional tetrahedral occupancy of Al^{3+} is observed. It was also confirmed by Momot et al. that upon the reductive annealing, a rearrangement of the Al^{3+} coordination in ZnO lattice happens by migration of the Al^{3+} ions at interstitial positions to the substitutional positions [96]. This “dopant activation” contributes to conductivity boost up by increment of active charge carriers.

5.4.5 Optical Behavior of Films

Based on the Maxwell’s equations, the interaction between a medium and the incident electromagnetic wave depends on the electrical and magnetic characteristics of the medium; or more precisely, on the electrical conductivity σ and permittivity ε as well as the magnetic permeability [97]. So regarding non-magnetic compounds with permeability of unit of value, including conventional TCOs, the optical behavior depends on whether the medium shows dielectric or conductive features. The distinction resides in the fact that in the former, just bound electrons exist while in the latter, moving free electrons as the charge carriers respond to the incident wave as well. This interaction depends on the concentration and mobility values of free electrons; indicating that, different optical behaviors are expected for samples of a certain compound with different N and μ and hence, different conductivity. Such correlation between the optical and electrical behaviors is confirmed by the results displayed in Table 5.5 as the summary of the observed values in Figures 5.5 to 5.7 for the optical properties of Group B samples after the additional heat-treatment. In the following, we discuss the effect of N and μ on the observed optical behavior in two forms of optical absorption and dispersion.

5.4.5.1 Absorption Behavior

For high-energy photons of around 3 eV and above (equivalent with UV wavelengths of $\lambda \leq 400$ nm), the sharp reduction in the transmittance spectra in Figure 5.5(a) shows that the optical behaviors of the samples are dominated by the fundamental absorption occurring as excitation of electrons. In this range, as depicted in the inset of Figure 5.6(a), the absorption coefficient α shows two different relationships with the photon energy:

The first one, stated as Tauc empirical rule in Equation (5.7), is a parabolic relationship applied to the incident photons with energy levels higher than the band-gap energy ($E_g < E$); for which the eventual excitation of electrons happens as a direct "interband transition" from the valence to the conduction band. The E_g value for the band structure of a pure undoped ZnO single-crystal has been reported controversially ranging from 3.1 to 3.4 eV; but values above 3.3 eV are confirmed more frequently [41,81]. This is higher than the calculated E_g value of the undoped ZnO sample reported around 3.28 eV in Table 5.5. This "band-gap narrowing" is in accordance with previously reported data about ZnO thin films prepared by the sol-gel method on the quartz substrate [81,48] and it is associated with the existence of surface-defects. As mentioned in Section 5.4.4, due to being of small grain-size, there is a high density of surface-defects in form of grain-boundaries that create localized states within the band-gap and trap charge carriers from the bulk of the grains. It is reported that charged boundary surfaces decrease the E_g value [81,48]. So the absorption coefficient and E_g value of the undoped ZnO thin film sample is smaller than that of a single-crystal ZnO. On the other hand, there is an increase in the E_g values of AZO samples compared to the undoped ZnO one. This "band-gap widening" is reported to occur proportionally with increasing the free charge carriers through importing Al^{3+} dopants to the ZnO lattice [89]. As stated in Section 5.4.3, the substitution of smaller Al^{3+} with Zn^{2+} ions increases the compressive strain along the c-axis direction of AZO samples; which is reported to cause band-gap widening compared with the undoped ZnO sample [80,81,98]. More importantly and based on the Moss–Burstein effect, doping generates donor levels at the base of the conduction band and increases the charge carriers through filling there with free electrons. Hereafter, the excited electrons from the valence band must overcome an additional energy gap to reach empty available states [43]. So a higher widening is expected for a larger concentration of free charge carriers N. Based on the difference in E_g values of Group B samples, we can conclude that N follows this trend: $N_{(ZnO)} \ll N_{(AZO\ 2\%)} \leq N_{(AZO2\%\ mod.)}$.

At the same time, the second relationship is an exponential one, introduced as Urbach empirical rule in Equation (5.8) for the photons with energy levels of $E < E_g$. It describes the transition of electrons in the localized states positioned within the band-gap and indicates the absorption of photon with energy levels even below the band-gap energy. The Urbach energy E_U characterizes the degree of absorption edge extension in to the sub-gap region and is related to the crystalline lattice disordering caused by the thermal vibrations and also crystallographic faults [45]. Thus, in a constant temperature, structural defects in the form of deviation from the perfect periodicity of an ideal crystalline state have the main contribution in increasing the width of absorption edge and observing higher Eu values [99]. With respect to electronic states, as it was mentioned in the Section 5.4.4, structural defects introduce localized electronic states within the band-gap, leading to the so

called “tailing” of the states above the valence band and below the conduction band with an exponential distribution [84,100]. Therefore, while the band edges terminate abruptly in a defect-free single-crystalline structure and no optical absorption happens below the band-gap energy, in amorphous or microcrystalline and in heavily-doped structures, the localized band-tail states encroaching to the band-gap induce the optical absorption with an exponential dependency on the photon energy [101]. Here, E_U corresponds to the width of these localized states and informs about the overall effect of all types of lattice disorders such as strains, dislocations, porosities and most importantly grain-boundaries that form the trap states together [45,81]. To a minor extent, it is also associated with the fault originating from the remained organic molecules introduced to the system in the role of capping ligands [102]; as could be traced in the present study in Figure 5.3 in form of a pair of weak peaks related to CH_2 bond of MEA after thermal treatment at 600 °C. Since in ZnO as a n-type semiconductor the Fermi level is above the localized states [18,84], they act as the electron acceptor and can trap free electrons; so the charge transport is assumed as a series of trapping and release events regarding such electron traps. The density of these localized states is a determining factor in the electronic performance of a semiconductor in terms of reducing its charge carrier mobility μ; and it is found the density of localized states increases with increasing the E_U value [100]. So based on the difference in E_U values of Group B samples, we conclude that μ follows this trend: $\mu_{(AZO\ 2\%)} < \mu_{(AZO2\%\ mod.)} < \mu_{(ZnO)}$.

In addition to the transition of electrons, the fundamental absorption is also attributed to the formation of excitons. Excitons are bound-states between the excited electrons in the conduction band and the corresponding holes in the valence band stabilized through Coulomb force attraction. These excitonic states dominate the absorption above the absorption edge [103]. As observed in Figure 5.6(a), the undoped ZnO sample shows an excitonic peak at around 3.4 eV in the absorption coefficient spectrum α, coordinated with the peak at around 364 nm in the absorption index spectrum k of Figure 5.7(b). The excitonic peak is also correlated with a minimum in the transmittance spectrum in Figure 5.5(a), as a shoulder peak between 360 to 370 nm. However, the excitonic absorption peak is hardly observed for the AZO samples spectra, indicating that the so called “exciton Mott transition” is activated; whereby, the interaction of excitons with free electrons in the conduction band alters the electron-hole binding characteristics and results in exciton dissociation and therefore, broadening or total vanishing of the excitonic absorption peak [104-106]. The exciton Mott transition implies the existence of free electrons in the conduction band and having a degenerate semiconductor with metallic behavior [42,106]. Here, for both spectra of α and k, the broadening of excitonic peak in the modified AZO sample is detected slightly more intensive, so it may be concluded that a fairly higher density of free electrons in the conduction band of the modified AZO

sample causes more exciton dissociation and almost total vanishing of the peak, and hence, $N_{(ZnO)} \ll N_{(AZO\ 2\%)} \leq N_{(AZO2\%\ mod.)}$.

For the photons with visible and IR wavelengths of around $400 \leq \lambda \leq 700$ nm and $\lambda \geq 700$ nm (possessing the energy levels of 1.6 to 3 eV and below 1.6 eV), the interband transition of bound electrons does not occur, as the incident photons cannot provide the required energy for the electron excitation. So principally no absorption behavior is expected in these ranges; however, the presence of free electrons in the conduction band and their response to the incident photons affects the optical behavior of a degenerate semiconductor compared to the non-degenerate one.

In the range of visible wavelengths, as depicted in Figure 5.5(a), the undoped ZnO sample exhibits a high average transmittance up to nearly 90% while the value drops to roughly 80% for the doped samples. The visible reflectance spectra in Figure 5.5(c) also depicts a clear distinction where average values for the doped samples are nearly 22% and 18% compared to 12% for the undoped ZnO one. On the other hand, the visible range of the absorptance spectra in Figure 5.5(d) is almost identical for all samples with average values below 1%. Insignificant visible absorption is also confirmed by the spectra of absorption coefficient α and absorption index k in Figure 5.6(a) and 5.7(b) respectively. This observation shows that the transparency loss in the visible range is mainly due to the reflection, and not because of the transition-based absorption of photons.

In the IR range, as depicted in Figures 5.5(a) and (b), samples are highly transparent as long as a sharp reduction in the transmittance occurs for all. However, the undoped ZnO sample keeps the transparency for a much broader wavelength interval compared to the doped ones. At the same time, on the far right of the absorptance spectra as illustrated in the inset of Figure 5.5(d), a new absorption trend of the so called “free carrier absorption” is observed to initiate only for the doped samples. The free carrier absorption is correlated to the increment of absorption coefficient for the low-energy photons in Figures 5.6(a) and 5.6(d), and is responsible for transmission loss in the IR range as illustrated in Figure 5.5(b). The free carrier absorption increases directly with the free carrier concentration N [107-109], as the larger value of N changes the onset and maximum wavelength of the absorptance spectrum with a blue shift [3]. The blue shift could be observed for the modified AZO sample in the inset of Figure 5.5(d) and also in Figure 5.5(b) supposing that the maximum absorptance happens roughly at the transmission minimum wavelength. Accordingly, through comparing Figures 5.5(b) and 5.5(d) it can be concluded that: $N_{(ZnO)} \ll N_{(AZO\ 2\%)} \leq N_{(AZO2\%\ mod.)}$.

5.4.5.2 Dispersion Behavior

The final argument on the samples optical behavior could be stated through the dispersion theory, which explains the frequency-dependent response of a medium to the incident wave from the optical and electrical point of view, in terms of refraction

and relative permittivity function. Accordingly [108], the solid medium is considered as an arrangement of self-oscillating components embedded in vacuum. Their response to an incident electromagnetic wave is emitting wavelets with the same frequency as of the incident wave expanding in all directions; however wavelets interference is constructive just in one direction and destructive in other lateral directions. So a redirected secondary wave is formed and propagates in the medium. The emission of wavelets happens with a delay, so compared to the incident wave, the secondary wave has a phase-lag which reduces its amplitude. The phase-lag value of a single wavelet is related to the incident wave frequency ω, and also the medium oscillation resonance ω_r. The total phase-lag is the aggregate of all phase-lags formed by all components along propagation path, so it is proportional with the medium thickness. For a thin medium or when the incident wave is of very low-energy in which $\omega \ll \omega_r$, there is almost no delay in wavelet emission and the total phase-lag is nearly zero. In this condition, the secondary wave propagates through the medium with the same amplitude and frequency of the incident wave; which means that the medium is transparent. For a thick medium or when the incident wave is of higher energy, the phase-lag increases directly with the ω and thickness. In this condition, the secondary wave has the same frequency but less amplitude than that of the incident wave, indicating partial energy absorption and less transmission. Finally for an incident wave in which $\omega = \omega_r$, or when the medium is thicker, the amplitude of the secondary wave becomes zero and the total absorption occurs.

Optically, the redirection of the secondary wave determines the refraction of light and the refractive index value n; and the amplitude reduction, resulted from the total phase-lag, associates with the absorption index k and therefore, the absorption coefficient α as stated in Equation (5.9). Figures 5.7(a) and 5.7(b) depict the refraction function of Group B samples. The k value in the visible region is nearly zero for all samples, following regular transparent semiconductors properties. However, in the infrared region as depicted in the inset of Figure 5.7(b), an increasing trend of k is observed for the doped samples unlike the undoped ZnO one, indicating the free carrier absorption as mentioned in Section 5.4.5.1. Similarly, the blue shift of the onset wavelength in the modified AZO sample indicates a slightly higher value of free carrier concentration compared with the pure AZO one. On the other hand, since n is affected by the degree of crystallinity, it is possible to evaluate the density of defects through comparing the n values of the films with that of the bulk .Using Lorentz–Lorentz relation stated in Equation (5.10) the porosity volume fraction is estimated as a basis to compare the films structural uniformity and thus, the carrier transport mobility. So according to the data reported in Table 5.5, μ follows such a trend: $\mu_{(AZO\ 2\%)} < \mu_{(AZO2\%\ mod.)} < \mu_{(ZnO)}$.

From the electrical point of view, the response of the medium to the oscillating electric field $\vec{E}$ of an incident electromagnetic wave in the optical frequency range is

described by formation of oscillating electronic dipoles due to a slight shifting of the negative cloud of electrons from positive atomic nuclei. The summation of all dipole moments is the electronic polarization field $\vec{P}$, which has a phase delay compared to $\vec{E}$ and is related to it through the frequency-dependent parameter of electrical permittivity $\bar{\varepsilon}$ as $\vec{P} \sim \bar{\varepsilon}.\vec{E}$ [108]. Similar to refraction function, $\bar{\varepsilon}$ also is a complex function and comprises a real part ε indicating the degree to which the medium can be polarized and an imaginary component $\acute{\varepsilon}$ associated with the attenuation of electromagnetic wave passing through the medium [109]. Figures 5.7(c) and 5.7(d) compare the permittivity function of Group B samples. The samples demonstrate an almost a similar trend throughout the selected frequency (energy) region, with a maximum polarization around the band-gap energy as the equivalent for the resonance frequency of dipole oscillation. For the incident $\vec{E}$ of higher frequencies, the dipoles are no longer able to follow the oscillations and the electronic polarization stops, but the dipoles oscillation continues until being absorbed and attenuated by the structure. This time-dependent process is known as dielectric relaxation, which is evidenced by a drop in ε and a maximum in $\acute{\varepsilon}$ [110]. In spite the similar trend, it is observed that the undoped ZnO shows sharp peaks for both ε and $\acute{\varepsilon}$ spectra around the band-gap energy, while for the doped samples peak broadening and reduction of both ε and $\acute{\varepsilon}$ values occurs. In $\acute{\varepsilon}$ spectra, the undoped ZnO peak correlates with the excitonic absorption which is broadened for the doped samples under similar justification explained in Section 5.4.5.1. For ε, this observation is attributed to shorter dielectric relaxation, resulting from higher damping intensity against the dipoles oscillation [111]. The possible source for the damping of dipoles oscillation could be associated to the active electron scattering mechanisms. As stated in Section 5.4.4, in the undoped ZnO the ionized scattering is less frequent compared to the doped ones, which is claimed to cause collision-based damping [112]. Therefore, a higher level of damping and shorter relaxation time is concluded for AZO films. Considering the equal level of doping and thus, a nearly identical ionized scattering in AZO structures, difference in their peak broadening could be related to the damping originated from structural non-uniformity of grain-boundaries, as previously referred by surface-defect scattering [110]. This means that the lower peak broadening and damping intensity could be associated with less surface-defect scattering in the modified AZO compared with the pure AZO. The effect of grain size reduction on relaxation time shortening is also observed in other sol-gel derived systems [113]. The proposed comparison among damping intensity of the samples is in accordance with the calculated values for the damping energy Γ reported in Table 5.5 as $\Gamma_{(ZnO)} < \Gamma_{(AZO2\%\ mod.)} < \Gamma_{(AZO\ 2\%)}$. Eventually, assuming that $\bar{\varepsilon}$ is affected by the presence of free electrons and structural defects through their impact on the damping intensity, a qualitative estimation for the scattering time τ of electrons could be proposed by comparing dispersive behavior of $\bar{\varepsilon}$. The scattering time τ, which has inverse relationship with the damping as $\tau \sim 1/\Gamma$ is considered as the average of

the time intervals that an electron in the electric field is accelerated until it collides with other electrons or with structural defects that changes its energy. This parameter fundamentally associates with the concept of electron mobility by a direct relationship as $\mu \sim \tau$ [114]. Thus, we can conclude that μ follows such a trend: $\mu_{(AZO\ 2\%)} < \mu_{(AZO2\%\ mod.)} < \mu_{(ZnO)}$.

5.5 Conclusions

In this chapter the effects of sol chemistry and thermal treatment procedure on the optical and electrical properties of sol-gel derived ZnO thin films doped with 2 at.% of aluminium ions was studied and the polycrystalline nature and the grain-boundaries characteristics of microstructure were determined as the most crucial factors on the final results.

The sol chemistry was modified by altering the hydrolysis reaction through adding water with the molar ratio of [H_2O/ZAD] = 2. It was argued that a complex ion forms in the coating sol in which, the Zn^{2+} cores are coordinated by MEA molecules and acetate ions in a dimer structure. The addition of extra water increases the amount of free $(OH)^-$ as the hydrolysis agent and accelerates formation of hydroxide-based complexes owing to the highly basic condition provided by ratio of [MEA/ZAD] = 2.

The structural analysis of the films via XRD diffraction analysis showed that the thermal treatment in high-temperature approach brings about samples with grains of considerably stronger c-axis preferred orientation compared with those of obtained from the low-temperature one. This result indicates that the high-temperature approach provides a better separation of the decomposition and crystallization steps during the thermal evolution of the deposited gel; a claim which was confirmed through the TG-DTA measurement and FT-IR spectroscopy. Therefore, the energetically-preferred columnar morphology with higher $T_c(002)$ and $I_r(002)$ values develops less restrictedly through the high-temperature approach, due to being less disturbed with the release of organic residuals during the nucleation and growth of the grains. Moreover, as the second conclusion for this part, the fairly larger crystallite size and slightly less microstrain values in the modified AZO structures implies an enhanced structural crystallinity after the growth process, originating from less crystal lattice distortion and fewer numbers of defects such as grain-boundaries and porosities.

The 4-point probe evaluation of thin films electrical properties after the final heat-treatment showed that ρ values of the doped films were around one order of magnitude smaller through the high-temperature approach compared with the low-temperature one; a reduction from around 3 to 4 Ω.cm to less than 0.5 Ω.cm. But for the undoped ZnO film ρ value was not affected. Besides, among the doped films, ρ values of modified AZO films were detected fairly lower than the pure AZO ones. The obtained conclusions confirm the correlation between the grain-boundaries characteristics and the conductivity values. Providing that enough carrier

concentration is supplied via doping, the stronger c-axis oriented morphology obtained through the high-temperature approach results in less density of grain-boundaries which consequently reduces the surface-defects scattering. Therefore, the increase of carriers' mobility is believed to improve the conductivity. Moreover, for the modified AZO film, the fairly larger crystallite size and slightly less microstrain value could provide better mobility and conductivity values compared with the pure AZO ones.

In addition to the high-temperature approach, an additional heat-treatment step performed under the reducing atmosphere of Ar/H_2 showed to have an extremely determining effect on the conductivity through decreasing the R_{sh} values by nearly two orders of magnitude; a reduction from around 0.4 – 0.5 Ω.cm to nearly 6 – 15 mΩ.cm. It was argued that while the low partial pressure of oxygen helps in desorption of acceptor oxygen molecules chemisorbed on the surface-defects and eliminating the related acceptor states, the partial introduction of H_2 creates shallow donor states. Therefore, the intrinsic conductivity improves. In AZO samples, the extrinsic carriers are also affected by the reduction annealing, since a rearrangement of Al^{3+} coordination in ZnO lattice happens through the migration of Al^{3+} ions located in interstitial positions to the substitutional positions. So the reduction annealing leads to the "dopant activation" in terms of increasing the substitutional tetrahedral occupancy of Al^{3+} and therefore, contributes to conductivity boost up by increasing the active charge carriers.

Finally, the UV-Vis-NIR spectroscopy that was performed to study the absorption and dispersion behaviors of the films supported the higher mobility, and to a lesser extent, the concentration of charge carriers in the modified AZO film. From the results obtained for E_u values, n values and studying the dielectric relaxation, it was concluded that $\mu_{(AZO\ 2\%)} < \mu_{(AZO2\%\ mod.)} < \mu_{(ZnO)}$. At the same time, by investigation on the band-gap widening, excitonic transition and the free carrier absorption in NIR region, it was concluded that: $N_{(ZnO)} \ll N_{(AZO\ 2\%)} \leq N_{(AZO2\%\ mod.)}$. The obtained orders for N and μ are in accordance with the conductivity order of $\sigma_{(ZnO)} \ll \sigma_{(AZO\ 2\%)} < \sigma_{(AZO2\%\ mod.)}$.

Taking the optical transmission in to account, the figure-of-merit values showed the following order: $FoM_{(ZnO)} \ll FoM_{(AZO\ 2\%)} < FoM_{(AZO2\%\ mod.)}$. This indicates the enhanced performance of the modified film as a transparent conducting film. The result for the modified AZO sample is in the same class of the highest-ranking AZO films previously obtained via sol–gel method, with the resistivity values in the order of few mΩ·cm, which is equivalent with the sheet resistance of $R_{sh} < 500$ Ω/sq, and the average visible transmittance of $80\% \leq T \leq 90\%$ [93]. However, compared to the specifications reported for the AZO films obtained via more sophisticated techniques such as sputtering [115], chemical vapor deposition [116], and atomic layer deposition [117], which provide thin films with resistivity that is one order of magnitude lower and similar visible transmittance. Nevertheless, considering the

high cost of TCO substrates, the sol–gel derived AZO films are suitable to improve the cost/watt ratio in applications such as inkjet printing of low-cost printed electronics and more affordable DSSC devices.

5.6 References

1. Lewis, B.G.; Paine, D.C. Applications and Processing of Transparent Conducting Oxides. MRS Bull. **2000**, 25, 22–27.
2. Pasquarelli, R.M.; Ginley, D.S.; O'Hayre, R. Solution processing of transparent conductors: From flask to film. Chem. Soc. Rev. **2011**, 40, 5406–5441.
3. Coutts, T.J.; Wu, X.; Mulligan, W.P.; Webb, J.M. High-performance, transparent conducting oxides based on cadmium stannate. J. Electron. Mater. **1996**, 25, 935–943.
4. Haacke, G. New figure of merit for transparent conductors. J. Appl. Phys. **1976**, 47, 4086–4089.
5. Jain, V.K.; Kulshreshtha, A.P. Indium-Tin-Oxide transparent conducting coatings on silicon solar cells and their "figure of merit." Sol. Energy Mater. **1981**, 4, 151–158.
6. Gordon, R.G. Preparation and Properties of Transparent Conductors. MRS Proc. **1996**, 426.
7. Gordon, R.G. Criteria for Choosing Transparent Conductors. MRS Bull. **2000**, 25, 52–57.
8. Hu, L.; Hecht, D.S.; Grüner, G. Percolation in Transparent and Conducting Carbon Nanotube Networks. Nano Lett. **2004**, 4, 2513–2517.
9. De, S.; Coleman, J.N. Are There Fundamental Limitations on the Sheet Resistance and Transmittance of Thin Graphene Films? ACS Nano **2010**, 4, 2713–2720.
10. Sepulveda-Mora, S.B.; Cloutier, S.G. Figures of merit for high-performance transparent electrodes using dip-coated silver nanowire networks. J. Nanomater. **2012**, 2012.
11. Stadler, A. Transparent Conducting Oxides—An Up-To-Date Overview. Materials (Basel). **2012**, 5, 661–683.
12. Minami, T. Transparent conducting oxide semiconductors for transparent electrodes. Semicond. Sci. Technol. **2005**, 20, S35–S44.
13. Minami, T. Present status of transparent conducting oxide thin-film development for Indium-Tin-Oxide (ITO) substitutes. Thin Solid Films **2008**, 516, 5822–5828.
14. Puetz, J.; Chalvet, F.N.; Aegerter, M.A. Wet chemical deposition of transparent conducting coatings in glass tubes. Thin Solid Films **2003**, 442, 53–59.
15. Chen, Z.; Li, W.; Li, R.; Zhang, Y.; Xu, G.; Cheng, H. Fabrication of Highly Transparent and Conductive Indium–Tin Oxide Thin Films with a High Figure of Merit via Solution Processing. Langmuir **2013**, 29, 13836–13842.
16. Choi, S.; Kim, K.-T.; Park, S.; Kim, Y.-H.; Choi, S.; Kim, K.-T.; Park, S.K.; Kim, Y.-H. High-Mobility Inkjet-Printed Indium-Gallium-Zinc-Oxide Thin-Film Transistors Using Sr-Doped Al_2O_3 Gate Dielectric. Materials (Basel). **2019**, 12, 852.

17. Seto, J.Y.W. The electrical properties of polycrystalline silicon films. J. Appl. Phys. **1975**, 46, 5247–5254.
18. Ghosh, S.; Sarkar, A.; Chaudhuri, S.; Pal, A.K. Grain boundary scattering in aluminium-doped ZnO films. Thin Solid Films **1991**, 205, 64–68.
19. Ohyama, M.; Kozuka, H.; Yoko, T. Sol-Gel Preparation of Transparent and Conductive Aluminum-Doped Zinc Oxide Films with Highly Preferential Crystal Orientation. J. Am. Ceram. Soc. **2010**, 81, 1622–1632.
20. Nishio, K.; Miyake, S.; Sei, T.; Watanabe, Y.; Tsuchiya, T. Preparation of highly oriented thin film exhibiting transparent conduction by the sol-gel process. J. Mater. Sci. **1996**, 31, 3651–3656.
21. Calnan, S.; Tiwari, A.N. High mobility transparent conducting oxides for thin film solar cells. Thin Solid Films **2010**, 518, 1839–1849.
22. Znaidi, L.; Illia, G.J.A.A.S.; Guennic, R. Le; Sanchez, C.; Kanaev, A. Elaboration of ZnO Thin Films with Preferential Orientation by a Soft Chemistry Route. J. Sol-Gel Sci. Technol. **2003**, 26, 817–821.
23. Ohyama, M.; Kouzuka, H.; Yoko, T. Sol-gel preparation of ZnO films with extremely preferred orientation along (002) plane from zinc acetate solution. Thin Solid Films **1997**, 306, 78–85.
24. Kuo, S.-Y.; Chen, W.-C.; Lai, F.-I.; Cheng, C.-P.; Kuo, H.-C.; Wang, S.-C.; Hsieh, W.-F. Effects of doping concentration and annealing temperature on properties of highly-oriented Al-doped ZnO films. J. Cryst. Growth **2006**, 287, 78–84.
25. Chen, J.; Chen, D.; Chen, Z. Optimization of the process for preparing Al-doped ZnO thin films by sol-gel method. Sci. China, Ser. E Technol. Sci. **2009**, 52, 88–94.
26. Bu, I.Y.Y. Effects of the pre-annealing temperature on structural and optical properties of sol–gel deposited aluminium doped zinc oxide. Ceram. Int. **2014**, 40, 11941–11946.
27. Musat, V.; Teixeira, B.; Fortunato, E.; Monteiro, R.C.C. Effect of post-heat treatment on the electrical and optical properties of ZnO:Al thin films. Thin Solid Films **2006**, 502, 219–222.
28. Shu-wen, X. A Study of Annealing Time Effects on the Properties of Al:ZnO. Phys. Procedia **2012**, 25, 345–349.
29. Nehmann, J.B.; Ehrmann, N.; Reineke-Koch, R.; Bahnemann, D.W. Aluminum-doped zinc oxide sol–gel thin films: Influence of the sol's water content on the resistivity. Thin Solid Films **2014**, 556, 168–173.
30. Guzman, G.; Dahmani, B. Transparent conducting sol–gel ATO coatings for display applications by an improved dip coating technique. Thin Solid Films **2006**, 502, 281–285.
31. Lutterotti, L. Total pattern fitting for the combined size–strain–stress–texture determination in thin film diffraction. Nucl. Instruments Methods Phys. Res. Sect. B Beam Interact. with Mater. Atoms **2010**, 268, 334–340.
32. Sharma, D.; Jha, R. Transition metal (Co, Mn) co-doped ZnO nanoparticles: Effect on structural and optical properties. J. Alloys Compd. **2017**, 698, 532–538.
33. Meziane, K.; El Hichou, A.; El Hamidi, A.; Mansori, M.; Liba, A.; Almaggoussi, A. On the sol pH and the structural, optical and electrical properties of ZnO thin films. Superlattices Microstruct. **2016**, 93, 297–302.

34. Bandyopadhyay, S.; Paul, G.K.; Roy, R.; Sen, S.K.; Sen, S. Study of structural and electrical properties of grain-boundary modified ZnO films prepared by sol–gel technique. Mater. Chem. Phys. **2002**, 74, 83–91.
35. Shikha, D.; Mehta, V.; Sood, S.C.; Sharma, J. Structural and optical properties of ZnO thin films deposited by sol–gel method: effect of stabilizer concentration. J. Mater. Sci. Mater. Electron. **2015**, 26, 4902–4907.
36. Smits, F.M. Measurement of Sheet Resistivities with the Four-Point Probe. Bell Syst. Tech. J. **1958**, 37, 711–718.
37. Rietveld, G.; Koijmans, C. V.; Henderson, L.C.A.; Hall, M.J.; Harmon, S.; Warnecke, P.; Schumacher, B. DC conductivity measurements in the Van Der Pauw geometry. IEEE Trans. Instrum. Meas. **2003**, 52, 449–453.
38. Borgogno, J.-P.; Pelletier, E. Determination of the extinction coefficient of dielectric thin films from spectrophotometric measurements. Appl. Opt. **2009**, 28, 2895.
39. Gadallah, A.-S.; El-Nahass, M.M. Structural, Optical Constants and Photoluminescence of ZnO Thin Films Grown by Sol-Gel Spin Coating. Adv. Condens. Matter Phys. **2013**, 2013, 1–11.
40. Dolgonos, A.; Mason, T.O.; Poeppelmeier, K.R. Direct optical band gap measurement in polycrystalline semiconductors: A critical look at the Tauc method. J. Solid State Chem. **2016**, 240, 43–48.
41. Srikant, V.; Clarke, D.R. On the optical band gap of zinc oxide. J. Appl. Phys. **1998**, 83, 5447–5451.
42. Segura, A.; Sánchez-Royo, J.F.; García-Domene, B.; Almonacid, G. Current underestimation of the optical gap and Burstein-Moss shift in CdO thin films: A consequence of extended misuse of α2-versus-hv plots. Appl. Phys. Lett. **2011**, 99, 2–5.
43. Sernelius, B.E.; Berggren, K.-F.; Jin, Z.-C.; Hamberg, I.; Granqvist, C.G. Band-gap tailoring of ZnO by means of heavy Al doping. Phys. Rev. B **1988**, 37, 10244–10248.
44. Urbach, F. The Long-Wavelength Edge of Photographic Sensitivity and of the Electronic Absorption of Solids. Phys. Rev. **1953**, 92, 1324.
45. Studenyak, I. Urbach Rule in Solid State Physics. Int. J. Opt. Appl. **2014**, 8.
46. Poelman, D.; Smet, P.F. Methods for the determination of the optical constants of thin films from single transmission measurements: a critical review. J. Phys. D. Appl. Phys. **2003**, 36, 1850–1857.
47. Guenther, K.H. Physical and chemical aspects in the application of thin films on optical elements. Appl. Opt. **2009**, 23, 3612.
48. Bandyopadhyay, S.; Paul, G.K.; Sen, S.K. Study of optical properties of some sol–gel derived films of ZnO. Sol. Energy Mater. Sol. Cells **2002**, 71, 103–113.
49. Bond, W.L. Measurement of the refractive indices of several crystals. J. Appl. Phys. **1965**, 36, 1674–1677.
50. De, S.; Higgins, T.M.; Lyons, P.E.; Doherty, E.M.; Nirmalraj, P.N.; Blau, W.J.; Boland, J.J.; Coleman, J.N. Silver Nanowire Networks as Flexible, Transparent, Conducting Films: Extremely High DC to Optical Conductivity Ratios. ACS Nano **2009**, 3, 1767–1774.
51. Livage, J.; Henry, M.; Jolivet, J.P.; Sanchez, C. Chemical Synthesis of Fine Powders. MRS Bull. **1990**, 15, 18–25.

52. Livage, J.; Sanchez, C.; Toledano, P. Sol-Gel Synthesis of Metal Oxide Clusters and Colloids. MRS Proc. **1992**, 272.
53. Jiménez-González, A.E.; Soto Urueta, J.A.; Suárez-Parra, R. Optical and electrical characteristics of aluminum-doped ZnO thin films prepared by solgel technique. J. Cryst. Growth **1998**, 192, 430–438.
54. Ohya, Y.; Saiki, H.; Takahashi, Y. Preparation of transparent, electrically conducting ZnO film from zinc acetate and alkoxide. J. Mater. Sci. **1994**, 29, 4099–4103.
55. Zhong, X.; Feng, Y.; Zhang, Y.; Lieberwirth, I.; Knoll, W. Nonhydrolytic Alcoholysis Route to Morphology-Controlled ZnO Nanocrystals. Small **2007**, 3, 1194–1199.
56. Znaidi, L.; Soler Illia, G.J.A.A.; Benyahia, S.; Sanchez, C.; Kanaev, A. V Oriented ZnO thin films synthesis by sol–gel process for laser application. Thin Solid Films **2003**, 428, 257–262.
57. Chakrabarti, S.; Ganguli, D.; Chaudhuri, S. Substrate dependence of preferred orientation in sol–gel-derived zinc oxide films. Mater. Lett. **2004**, 58, 3952–3957.
58. Kamalasanan, M.N.; Chandra, S. Sol-gel synthesis of ZnO thin films. Thin Solid Films **1996**, 288, 112–115.
59. Ohyama, M.; Kozuka, H.; Yoko, T.; Sakka, S. Preparation of ZnO Films with Preferential Orientation by Sol-Gel Method. J. Ceram. Soc. Japan **1996**, 104, 296–300.
60. Hancock, R.D. The chelate effect in complexes with ethanolamine. Inorganica Chim. Acta **1981**, 49, 145–148.
61. Sridaeng, D.; Jitaree, W.; Thiampanya, P.; Chantarasiri, N. Preparation of rigid polyurethane foams using low-emission catalysts derived from metal acetates and ethanolamine. e-Polymers **2016**, 0.
62. Ishioka, T.; Murata, A.; Kitagawa, Y.; Nakamura, K.T. Zinc(II) Acetate Dihydrate. Acta Crystallogr. Sect. C Cryst. Struct. Commun. **1997**, 53, 1029–1031.
63. Ishioka, T.; Shibata, Y.; Takahashi, M.; Kanesaka, I.; Kitagawa, Y.; T. Nakamura, K. Vibrational spectra and structures of zinc carboxylates I. Zinc acetate dihydrate. Spectrochim. Acta Part A Mol. Biomol. Spectrosc. **1998**, 54, 1827–1835.
64. Yang, J.; Puchberger, M.; Qian, R.; Maurer, C.; Schubert, U. Zinc(II) complexes with dangling functional organic groups. Eur. J. Inorg. Chem. **2012**, 4294–4300.
65. Gómez-Núñez, A.; Alonso-Gil, S.; López, C.; Roura, P.; Vilà, A. Role of Ethanolamine on the Stability of a Sol–Gel ZnO Ink. J. Phys. Chem. C **2017**, 121, 23839–23846.
66. Gómez-Núñez, A.; López, C.; Alonso-Gil, S.; Roura, P.; Vilà, A. Study of a sol–gel precursor and its evolution towards ZnO. Mater. Chem. Phys. **2015**, 162, 645–651.
67. Znaidi, L. Sol-gel-deposited ZnO thin films: A review. Mater. Sci. Eng. B Solid-State Mater. Adv. Technol. **2010**, 174, 18–30.
68. Znaidi, L.; Touam, T.; Vrel, D.; Souded, N.; Yahia, S.; Brinza, O.; Fischer, A.; Boudrioua, A. AZO Thin Films by Sol-Gel Process for Integrated Optics. Coatings **2013**, 3, 126–139.

69. Boudjouan, F.; Chelouche, A.; Touam, T.; Djouadi, D.; Khodja, S.; Tazerout, M.; Ouerdane, Y.; Hadjoub, Z. Effects of stabilizer ratio on photoluminescence properties of sol-gel ZnO nano-structured thin films. J. Lumin. **2015**, 158, 32–37.
70. Khodja, S.; Touam, T.; Chelouche, A.; Boudjouan, F.; Djouadi, D.; Hadjoub, Z.; Fischer, A.; Boudrioua, A. Effects of stabilizer ratio on structural, morphological, optical and waveguide properties of ZnO nano-structured thin films by a sol–gel process. Superlattices Microstruct. **2014**, 75, 485–495.
71. Yahia, I.S.; Farag, A.A.M.; Cavas, M.; Yakuphanoglu, F. Effects of stabilizer ratio on the optical constants and optical dispersion parameters of ZnO nano-fiber thin films. Superlattices Microstruct. **2013**, 53, 63–75.
72. Hosseini Vajargah, P.; Abdizadeh, H.; Ebrahimifard, R.; Golobostanfard, M.R. Sol–gel derived ZnO thin films: Effect of amino-additives. Appl. Surf. Sci. **2013**, 285, 732–743.
73. Tari, O.; Aronne, A.; Addonizio, M.L.; Daliento, S.; Fanelli, E.; Pernice, P. Sol–gel synthesis of ZnO transparent and conductive films: A critical approach. Sol. Energy Mater. Sol. Cells **2012**, 105, 179–186.
74. Zeleňák, V.; Vargová, Z.; Györyová, K. Correlation of infrared spectra of zinc(II) carboxylates with their structures. Spectrochim. Acta Part A Mol. Biomol. Spectrosc. **2007**, 66, 262–272.
75. Palacios, E.G.; Juárez-López, G.; Monhemius, A.J. Infrared spectroscopy of metal carboxylates. Hydrometallurgy **2004**, 72, 139–148.
76. Fujihara, S.; Sasaki, C.; Kimura, T. Crystallization behavior and origin of c-axis orientation in sol-gel-derived ZnO:Li thin films on glass substrates. Appl. Surf. Sci. **2001**, 180, 341–350.
77. Fujimura, N.; Nishihara, T.; Goto, S.; Xu, J.; Ito, T. Control of preferred orientation for ZnOx films: control of self-texture. J. Cryst. Growth **1993**, 130, 269–279.
78. Schuler, T.; Aegerter, M.A. Optical, electrical and structural properties of sol gel ZnO:A1 coatings. Thin Solid Films **1999**, 351, 125–131.
79. Goebbert, C.; Gasparro, G.; Schuler, T.; Krajewski, T.; Aegerter, M.A. Influence of the Layer Morphology on the Electrical Properties of Sol Gel Transparent Conducting Oxide Coatings. J. Sol-Gel Sci. Technol. **2000**, 19, 435–439.
80. Malek, M.F.; Mamat, M.H.; Sahdan, M.Z.; Zahidi, M.M.; Khusaimi, Z.; Mahmood, M.R. Influence of various sol concentrations on stress/strain and properties of ZnO thin films synthesised by sol–gel technique. Thin Solid Films **2013**, 527, 102–109.
81. Srikant, V.; Clarke, D.R. Optical absorption edge of ZnO thin films: The effect of substrate. J. Appl. Phys. **1997**, 81, 6357–6364.
82. Nomoto, J.; Inaba, K.; Kobayashi, S.; Watanabe, T.; Makino, H.; Yamamoto, T. Characteristics of Carrier Transport and Crystallographic Orientation Distribution of Transparent Conductive Al-Doped ZnO Polycrystalline Films Deposited by Radio-Frequency, Direct-Current, and Radio-Frequency-Superimposed Direct-Current Magnetron Sputter. Materials (Basel). **2017**, 10, 916.
83. Nguyen, V.H.; Gottlieb, U.; Valla, A.; Muñoz, D.; Bellet, D.; Muñoz-Rojas, D. Electron tunneling through grain boundaries in transparent conductive oxides

and implications for electrical conductivity: the case of ZnO:Al thin films. Mater. Horizons **2018**, 5, 715–726.
84. Lormand, G. ELECTRICAL PROPERTIES OF GRAIN BOUNDARIES. Le J. Phys. Colloq. **1982**, 43, C6-283-C6-292.
85. Srikant, V.; Sergo, V.; Clarke, D.R. Epitaxial Aluminum-Doped Zinc Oxide Thin Films on Sapphire: II, Defect Equilibria and Electrical Properties. J. Am. Ceram. Soc. **1995**, 78, 1935–1939.
86. Look, D.C.; Coşkun, C.; Claflin, B.; Farlow, G.C. Electrical and optical properties of defects and impurities in ZnO. Phys. B Condens. Matter **2003**, 340–342, 32–38.
87. Lany, S.; Zunger, A. Dopability, intrinsic conductivity, and nonstoichiometry of transparent conducting oxides. Phys. Rev. Lett. **2007**, 98, 2–5.
88. Liu, L.; Mei, Z.; Tang, A.; Azarov, A.; Kuznetsov, A.; Xue, Q.-K.; Du, X. Oxygen vacancies: The origin of n -type conductivity in ZnO. Phys. Rev. B **2016**, 93.
89. Tang, W.; Cameron, D.C. Aluminum-doped zinc oxide transparent conductors deposited by the sol-gel process. Thin Solid Films **1994**, 238, 83–87.
90. Geistlinger, H. effects on the thin-film conductivity. **1992**.
91. Glemza, R.; Kokes, R.J. Chemisorption of Oxygen on Zinc Oxide. J. Phys. Chem. **1965**, 69, 3254–3262.
92. Baik, S.J.; Jang, J.H.; Lee, C.H.; Cho, W.Y.; Lim, K.S. Highly textured and conductive undoped ZnO film using hydrogen post-treatment. Appl. Phys. Lett. **1997**, 70, 3516–3518.
93. Van de Walle, C.G. Hydrogen as a Cause of Doping in Zinc Oxide. Phys. Rev. Lett. **2000**, 85, 1012–1015.
94. Kemmitt, T.; Ingham, B.; Linklater, R. Optimization of Sol–Gel-Formed ZnO:Al Processing Parameters by Observation of Dopant Ion Location Using Solid-State ^{27}Al NMR Spectrometry. J. Phys. Chem. C **2011**, 115, 15031–15039.
95. Damm, H.; Adriaensens, P.; De Dobbelaere, C.; Capon, B.; Elen, K.; Drijkoningen, J.; Conings, B.; Manca, J. V; D'Haen, J.; Detavernier, C.; et al. Factors Influencing the Conductivity of Aqueous Sol(ution)–Gel-Processed Al-Doped ZnO Films. Chem. Mater. **2014**, 26, 5839–5851.
96. Momot, A.; Amini, M.N.; Reekmans, G.; Lamoen, D.; Partoens, B.; Slocombe, D.R.; Elen, K.; Adriaensens, P.; Hardy, A.; Van Bael, M.K. A novel explanation for the increased conductivity in annealed Al-doped ZnO: An insight into migration of aluminum and displacement of zinc. Phys. Chem. Chem. Phys. **2017**, 19, 27866–27877.
97. Jahani, S.; Jacob, Z. All-dielectric metamaterials. Nat. Nanotechnol. **2016**, 11, 23–36.
98. Ghosh, R.; Basak, D.; Fujihara, S. Effect of substrate-induced strain on the structural, electrical, and optical properties of polycrystalline ZnO thin films. J. Appl. Phys. **2004**, 96, 2689–2692.
99. Pejova, B. The Urbach–Martienssen absorption tails in the optical spectra of semiconducting variable-sized zinc selenide and cadmium selenide quantum dots in thin film form. Mater. Chem. Phys. **2010**, 119, 367–376.
100. Wager, J.F. Real- and reciprocal-space attributes of band tail states. AIP Adv. **2017**, 7.

101. O'Leary, S.K. An empirical density of states and joint density of states analysis of hydrogenated amorphous silicon: a review. J. Mater. Sci. Mater. Electron. **2004**, 15, 401–410.
102. Nelson, C.A.; Zhu, X.Y. Reversible surface electronic traps in PbS quantum dot solids induced by an order-disorder phase transition in capping molecules. J. Am. Chem. Soc. **2012**, 134, 7592–7595.
103. Muth, J.F.; Kolbas, R.M.; Sharma, A.K.; Oktyabrsky, S.; Narayan, J. Excitonic structure and absorption coefficient measurements of ZnO single crystal epitaxial films deposited by pulsed laser deposition. J. Appl. Phys. **1999**, 85, 7884–7887.
104. Li, X.D.; Chen, T.P.; Liu, P.; Liu, Y.; Leong, K.C. Effects of free electrons and quantum confinement in ultrathin ZnO films: a comparison between undoped and Al-doped ZnO. Opt. Express **2013**, 21, 14131.
105. Makino, T.; Tamura, K.; Chia, C.H.; Segawa, Y.; Kawasaki, M.; Ohtomo, A.; Koinuma, H. Optical properties of ZnO: Al epilayers: Observation of room-temperature many-body absorption-edge singularity. Phys. Rev. B - Condens. Matter Mater. Phys. **2002**, 65, 1–4.
106. Schleife, A.; Rödl, C.; Fuchs, F.; Hannewald, K.; Bechstedt, F. Optical absorption in degenerately doped semiconductors: Mott transition or Mahan excitons? Phys. Rev. Lett. **2011**, 107, 1–5.
107. Fujiwara, H.; Kondo, M. Effects of carrier concentration on the dielectric function of ZnO:Ga and In_2O_3:Sn studied by spectroscopic ellipsometry: Analysis of free-carrier and band-edge absorption. Phys. Rev. B **2005**, 71, 075109.
108. Li, X.D.; Chen, T.P.; Liu, Y.; Leong, K.C. Evolution of dielectric function of Al-doped ZnO thin films with thermal annealing: effect of band gap expansion and free-electron absorption. Opt. Express **2014**, 22, 23086.
109. Zheng, H.; Zhang, R.-J.; Li, D.-H.; Chen, X.; Wang, S.-Y.; Zheng, Y.-X.; Li, M.-J.; Hu, Z.-G.; Dai, N.; Chen, L.-Y. Optical Properties of Al-Doped ZnO Films in the Infrared Region and Their Absorption Applications. Nanoscale Res. Lett. **2018**, 13, 149.
110. Baker-Jarvis, J.; Kim, S. The Interaction of Radio-Frequency Fields With Dielectric Materials at Macroscopic to Mesoscopic Scales. J. Res. Natl. Inst. Stand. Technol. **2012**, 117, 1–60.
111. Andrade-Neto, A. V.; Andrade-Neto, A. V. Dielectric function for free electron gas: comparison between Drude and Lindhard models. Rev. Bras. Ensino Física **2017**, 39.
112. Elissalde, C.; Ravez, J. Ferroelectric ceramics: Defects and dielectric relaxations. J. Mater. Chem. **2001**, 11, 1957–1967.
113. Mandal, S.; Mullick, H.; Majumdar, S.; Dhar, A.; Ray, S.K. Effect of Al concentration in grain and grain boundary region of Al-doped ZnO films: a dielectric approach. J. Phys. D. Appl. Phys. **2008**, 41, 25307.
114. Hamberg, I.; Granqvist, C.G.; Berggren, K.-F.; Sernelius, B.E.; Engström, L. Band-gap widening in heavily Sn-doped In_2O_3. Phys. Rev. B **1984**, 30, 3240–3249.
115. Prakash, T.; Ramasamy, S.; Murty, B.S. Influence of bias voltage on dielectric relaxation of nanocrystalline anatase TiO_2 using modulus formalism. J. Appl. Phys. **2011**, 109.

116. Romanyuk, V.; Dmitruk, N.; Karpyna, V.; Lashkarev, G.; Popovych, V.; Dranchuk, M.; Pietruszka, R.; Godlewski, M.; Dovbeshko, G.; Timofeeva, I.; et al. Optical and electrical properties of highly doped ZnO:Al films deposited by atomic layer deposition on Si substrates in visible and near infrared region. Acta Phys. Pol. A **2016**, 129, A36–A40.

Chapter 6

Conclusions and Future Perspective

The overall objective of this thesis was to enhance sol-gel based approaches in synthesis of higher quality nanoparticles and thin films used in fabrication of DDSCs photo-electrodes, with the aim of improving the conversion efficiency of the cell in an affordable way.

In Chapter 2, it was theoretically explained that the DSSC efficiency depends on the morphological and structural features of the mesoporous layer of its photo-electrode, including the surface area, pore volume and crystallinity, due to their impact on the dye-loading capacity and charge transport mechanism and therefore, the final value of the photocurrent. Moreover, as two other parameters particularly related to the photo-electrode, the conductivity of the transparent conducting film and the condition of its interface with the mesoporous layer were noted to be influential factors on the overall efficiency of the DSSC due to their impact on the series resistance of the cell and the rate of electron-hole recombination.

In Chapter 3, choosing the TiO_2 nanopowder P25 to prepare the mesoporous layer, the already-discussed argument about the layer morphological features and the condition of its interface with the transparent conducting film were examined in terms of fabricating two samples by using different TiO_2 pastes. It was observed that the TiO_2 paste prepared by ethyl cellulose (EC) binder in α-terpineol results in a mesoporous layer with higher values of surface area and larger pore volumes compared to one prepared by the paste with polyethylene glycol (PEG) binder in water. The higher efficiency value for the cell with EC/terpineol-based paste emphasized on applicability of the approach on the improving the performance of DSSC.

Keeping in mind the results of Chapter 3 as a basis, Chapter 4 was aimed to synthesize mesoporous TiO_2 nanocrystalline particles with better morphological and structural features than that of P25 used in Chapter 2. Due to the amorphous nature of as-prepared powder obtained through the conventional sol-gel synthesis routes, a

surfactant-mediated approach was utilized in the water-in-oil micellar system of water/cyclohexane/Triton X-100 and it was attempted to synthesize the as-prepared nanocrystalline particles with higher surface area, better porosity features and improved crystallinity by changing the refluxing time and the water-to-surfactant molar ratio. It was observed that by increasing the reflux time to 24 h, the crystallinity and porosity improve considerably and the density and BET surface area values increase to nearly 3.133 $g \cdot cm^{-3}$ and 180 $m^2 \cdot g^{-1}$ respectively, indicating a significant enhancement for the nanoparticles quality in anatase phase. On the other hand, for the constant reflux time of 24 h, decreasing the water-to-surfactant molar ratio from 10 to 5 and 2 leads to formation of smaller nanoparticles with even higher surface area of around 220 – 240 $m^2 \cdot g^{-1}$, while a slight degradation in the crystallinity and porosity of the nanoparticles was observed. Moreover, the step for removing the surfactant from the obtained powders was considerably longer. The obtained values indicate that reverse micelle approach was a feasible and low-cost method to synthesize TiO_2 anatase nanoparticles with high surface area and noticeable porosity features providing them to be used for a variety of applications including DSSCs.

Chapter 5 was devoted to enhancing the features of the transparent conducting film as another component of photo-electrode DSSC. Sol-gel derived aluminium-doped zinc oxide (AZO) thin films doped with 2 at.% of aluminium ions were modified by altering the hydrolysis reaction through the addition of water with the molar ratio of $[H_2O/Zn] = 2$ and also perusing different thermal treatment procedures. The results of XRD analysis showed that in the sample prepared by the intermediate and final heat-treatment at 430 and 600 °C, grains of considerably stronger c-axis preferred orientation were formed compared with those of obtained by intermediate and final heat-treatment at 275 and 500 °C, because of better separation of the decomposition and crystallization steps during the thermal evolution of the deposited gel. This condition resulted in reduction of ρ values from around 3 to 4 Ω.cm to less than 0.5 Ω.cm due to the lower degrading effect of grain-boundaries on electron mobility in microstructures with c-axis preferred orientation. Besides, an additional heat-treatment step under the reducing atmosphere of Ar/H_2 could decrease R_{sh} values by nearly two orders of magnitude; a reduction from around 0.4 – 0.5 Ω.cm to nearly 6 – 15 mΩ.cm which resulted from desorption of acceptor oxygen molecules chemisorbed on the surface-defects and eliminating the related acceptor states as well as creating shallow donor states. The sample modified by adding additional amount of water showed a slightly better conductivity after each heat-treatment procedures which accompanied with moderately larger crystallite size and less microstrain values in their microstructures. Additionally, the results of UV-Vis-NIR spectroscopy showed that the improvement in conductivity values of the modified sample, to a larger extent, was due to increasing the mobility values indicated by less porosity, lower Urbach and damping energies and higher refractive index; to a

lesser extent, it resulted from increasing the charge carrier concentration indicated by more band-gap widening, less excitonic transition and wider free carrier absorption in NIR region. Finally, taking into account the optical transmission results, a higher figure-of-merit value was obtained for the modified sample. This indicated the enhanced performance of the modified film as a transparent conducting film. The result for the modified AZO sample was in the same class of the highest-ranking AZO films previously obtained via sol–gel method, with the resistivity values in the order of few mΩ·cm, equivalent with the sheet resistance of R_{sh} < 500 Ω/sq, and visible transmittance of 80% ≤ T ≤ 90%; but they were still lower than the values of AZO films obtained via more sophisticated techniques. However, considering the high cost of TCO substrates, the sol–gel derived AZO films were considered suitable to improve the cost/watt ratio in applications such as inkjet printing of low-cost printed electronics and more affordable DSSC devices.

As the future approach on this topic, we particularly point out to the possibility of altering the mesoporous/TCO interface from geometrical point of view.
Conventionally, the mesoporous layer and TCO film form a planar interface. As already dissused, in order to collect as many photons as possible for a given area or volume, a thicker mesoporous layer means the more photon number collection. On the other hand, the generated charges must to be transported to the external circuit; the longer is the path length, the higher the probability of losing the charge through recombination at defect sites on the nanocrystals. Thus, the amount of the transported charges decreases by increasing the mesoporous layer thickness. Consequently, there is an optimal thickness for the mesoporous layer which is around 10 – 15 μm for TiO_2 – based layers.
As an extrapolation, a 3-dimensional mesoporous/TCO interface, in which the TCO layer is extended into the mesoporous layer, can overcome some of the limitations of the 2D network. This 3D interface makes it possible to minimize the charge collection losses by reducing the distance that the charges have to travel to be collected by the TCO; and at the same time, it maintains a large photon collection volume due to providing high surface area which improves the cell efficiency. The extension of the TCO layer, as the current collector, into the matrix of a DSSC was as first proposed and presented by Zaban et al. They fabricated a core-shell structure in which, after deposition of a porous layer of ITO over a glass substrate via CVD, a thin layer of TiO_2 was deposited over it through the atomic layer deposition technique. Since then, there have been several similar attempts, all including the fabrication of a porous core-shell structure, wherein the TCO layer, synthesized through electrospinning, pulsed laser ablation or porous alumina template, is coated by TiO_2 layer. However, the core-shell structure does not provide enough space for the deposition of the mesoporous layer.

It is possible to promote this idea through formation of some extended branches of TCO using organic template-assisted method. This approach involves the ordered monolayer deposition of organic microspheres as the template over the TCO film and filling the voids with the TCO sol, followed by thermal decomposition of the template. The branches of TCO will be extended inside the mesoporous layer to perfrom the charge collection more efficiently.

Scientific Productions

M.Nateq and R.Ceccato, **"Enhanced Sol–Gel Route to Obtain a Highly Transparent and Conductive Aluminum-Doped Zinc Oxide Thin Film",** *Materials* **2019**, **12, 1744**
DOI:10.3390/ma12111744

M.Nateq and R.Ceccato, **"Sol-Gel Synthesis of TiO_2 Nanocrystalline Particles with Enhanced Surface Area through the Reverse Micelle Approach",** Accepted in *Advances in Materials Science and Engineering*, **manuscript number 1567824**
DOI:

R.Ceccato and M.Nateq "**Sintesi, microstruttura e proprietà elettriche di film a base di ZnO ottenuti via metodo sol-gel**", *Proceedings of "XI Congresso AICIng"*, Bologna, September 9–12, 2018, page 40
ISBN: 978 8879 59 8545

Participation and Activities

- **Conferences**

M.Nateq and R. Ceccato **"Dye sensitized solar cell with enhanced charge collector layer",** *Organic & Perovskite Solar Cells Conference,* Heraklion, October 19–20, 2016

M.Nateq and R. Ceccato **"Using inverse opal structure to enhance the charge collection in the dye-sensitized solar cel",** *15th Young Researchers' Conference on Materials Science and Engineering"* Belgrade, December 7–9, 2016

M.Nateq and R. Ceccato "**Template-assisted synthesis of ordered porous AZO layer as an enhanced "Transparent Conducting Film",** *Photonics as a key enabling technology,* Trento, November 17, 2017

- **Schools**

MatHero Summer School on **Organic Photovoltaics**, August 23–27, 2015, Freudenstadt, Lauterbad, Germany.

XXth International Krutyn Summer School on **Advanced Perovskite, Hybrid and Thin-film Photovoltaics**, June 12–18, 2016, Krutyń, Masurian Lake District, Poland.

- **Co-supervising**

Master's thesis in Mechatronics Engineering Faculty of Industrial Engineering:

"Realizzazione e Caratterrizzione di Celle Fotovotaiche Organiche"

Author: Jacopo Andermarcher
Supervisor: Riccardo Ceccato
Academic Year: 2014-2015

Acknowledgements

First and foremost, I would like to thank my supervisor, Professor Riccardo Ceccato, for his invaluable support during my studies and research at the Chemistry Lab of the Industrial Engineering department. By providing the opportunity of co-supervision of a Master's and several Bachelor's theses, he wisely prepared me a suitable basis for step-by-step learning the practical and theoretical aspects of my work. This thesis owes its accomplishment to his warmly patience, precise discipline and the ability to solve the problems as well.

I would like to especially thank my family for their unconditional love and support. I am glad to be able to repay their patience and sacrifice by successfully completing my PhD.

I spent the whole of this period at San Bartolameo student residence of the Opera Universitaria di Trento, a well-established complex of high standards of dormitory facilities and management and I am so much thankful for that. There I found true friends with whom I spent memorable, enjoyable and instructive moments of this five-year journey, Linda, Pranab, Tatev, Astghik, Payam and my guardian angel, Prapassorn Siriwichai. I would also like to express my gratitude to all of them.

M. Nateq

August 2019